# TEM examination of innovative materials for energy conversion

## Dissertation

zur Erlangung des akademischen Grades

Doktor der Ingenieurwissenschaften

(Dr.-Ing.)

der Technischen Fakultät

der Christian-Albrechts-Universität zu Kiel

Gero Neubüser

Kiel

2018

Betreuer: Prof. Dr. Lorenz Kienle
Zweitgutachter: Prof. Dr. Klaus Rätzke
Datum der mündlichen Prüfung: 07.12.2018

# Abstract

**TEM examination of innovative materials for energy conversion**

To meet the increasing demand for mobile energy storage, the development of more powerful rechargeable batteries is inevitable. Within this dissertation, different promising material systems for battery anodes as well as one for cathodes are being examined by methods of transmission electron microscopy (TEM).

A high-capacity anode was developed based on a novel silicon microwire structure. Like its starting material, silicon wafers, used in the semiconductor industry, these structures are highly crystalline and show a defined arrangement. Their large inner surface guarantees a steady and large absorption of Li ions and eventually a large capacity. In the course of repeated charging and discharging, strong capacity fading of the anode was noticed after only a few cycles, which was attributed to structural degradation. As a part of this work, causes and effects of electrode degradation will be examined. Recent advances are presented which pave the way to the development of more powerful electrodes. Not only crystalline, but also amorphous and porous silicon modifications were considered being synthesized by chemical extraction methods.

Another promising class of anode materials is represented by spinel-type transition metal oxides. According to the wide variety of applicable transition metals, this field of research bears a large potential for development. Types being already applied commercially in electric vehicles usually contain cobalt, which gives rise to considerable concern due to controversial mining conditions and should be avoided. Binary and ternary compounds are being researched and compared with respect to microstructural changes during charging/discharging.

Furthermore, a sulfur-based cathode material will be presented as a respective counterpart to the aforementioned anode concepts. A great benefit of sulfur is its theoretically high capacity, but integration into a suitable host material has so far not been successfully achieved. To map occurring processes, especially on the atomic scale, transmission electron microscopy provides suitable measures.

A competing or possibly complementary technology to electric battery is provided by the fuel cell, especially hydrogen-based types, which provide electric power through the reaction between oxygen and hydrogen into water. Significant for their economic use is an efficient generation of hydrogen through regenerative processes. Here, hydrogen production from water is considered as a very promising and environmental-friendly process in case of suitable catalysts. Recently synthesized copper-poor compounds will be presented and analyzed with respect to their ability to perform as photo catalyst to generate hydrogen.

# Zusammenfassung


**TEM Untersuchungen an neuartigen Materialien für Energieanwendungen**

Um dem wachsenden Bedarf an mobiler Energiespeicherung nachzukommen, ist die Entwicklung leistungsfähigerer Akkumulatoren unumgänglich. Verschiedene Konzepte für Anoden sowie eines für Kathoden werden mittels Methoden der Transmissionselektronenmikroskopie (TEM) untersucht.

Auf der Grundlage von neuartigen Silizium-Mikrodrahtstrukturen wurde eine Hochkapazitätsanode hergestellt. Analog zu ihrem Ausgangsmaterial, Siliziumwafern, bekannt aus der Halbleiterindustrie, sind diese Strukturen anfangs hochkristallin und besitzen eine definierte Anordnung. Durch die große innere Oberfläche kann eine gleichmäßige und hohe Aufnahme von Lithiumionen gewährleistet werden, d. h. eine hohe Kapazität. Im Zuge des Lade-/Entladezyklus wurden starke Kapazitätseinbußen schon nach wenigen Ladezyklen festgestellt, welche auf eine Degradation der Anode zurückgeführt wurden. Im Rahmen dieser Arbeit werden Ursachen und Ausmaß der Degradation herausgearbeitet und Ansätze zur Verbesserung vorgestellt und evaluiert, die zur Entwicklung einer leistungsfähigeren Anode beitragen. Neben kristallinem Silizium wird auch auf das Potenzial von amorphen und porösen Modifikationen eingegangen, welche mittels Extraktionsverfahren synthetisiert werden.

Eine ebenfalls vielversprechende Klasse von Anodenmaterialien sind Übergangsmetallspinelle. Aufgrund der Vielzahl infrage kommender Übergangsmetalle liegt hier ein großes Entwicklungspotenzial vor. Bereits kommerziell in Elektrofahrzeugen eingesetzte Typen enthalten unter anderem Kobalt, dessen Anteil aufgrund umstrittener Abbaubedingungen reduziert werden soll. Binäre und ternäre Metalloxide werden untersucht mit Fokus auf mikrostrukturellen Veränderungen während des Ladens und Entladens.

Als Gegenstück zu bereits erwähnten Anodensystemen wird des Weiteren ein schwefelbasiertes Kathodenmaterial vorgestellt. Schwefel besitzt eine hohe theoretische Kapazität, jedoch ist die Fixierung in einer geeigneten Matrix bisher nicht erfolgreich gewesen. Auch hier ist eine Anwendung der Transmissionselektronenmikroskopie vielversprechend, um ablaufende Prozesse auf atomarer Ebene zu verfolgen.

Eine konkurrierende oder möglicherweise auch ergänzende Technologie zur Batterietechnik sind Brennstoffzellen auf Wasserstoffbasis, mit deren Hilfe Wasserstoff und Sauerstoff bei positiver Energiebilanz zu Wasser reagieren. Entscheidend für deren wirtschaftlichen Betrieb ist eine effiziente Gewinnung von Wasserstoff durch regenerative Verfahren. Die Abscheidung von Wasserstoff aus Wasser durch photokatalytische Materialien ist ein vielversprechender und umweltfreundlicher Prozess, vorausgesetzt die verwendeten Materialien sind es auch. Im bereits bekannten Cu-In-S System werden neue kupferarme Verbindungen synthetisiert und ihre Fähigkeit Wasserstoff durch Photokatalyse zu gewinnen untersucht.

# Contents

# 1 Introduction

Versatile and efficient energy storage is an urgent technological challenge in order to replace fossil fuels and establish the use of renewable forms of energy. In nature, evolution enabled plants and animals to convert and store energy in various forms, e.g. ATP (adenosine triphosphate), glucose, fat or proteins. As a comparable technical solution, the electrical battery was invented and has to be developed further to ensure comfortable everyday application.

The first galvanic element working as battery – the Voltaic pile– was developed and published by Alessandro Volta in 1799. 60 years later, Gaston Planté invented the lead-acid battery the principle of which is still used today. In 1886, the dry cell battery was invented by Carl Gassner and the first model, a 1.5 V six-inch type, was marketed by the National Carbon Company[1] in the USA. In the 1970s, first concepts of the use of lithium for batteries based on $TiS_2$ and $MnO_2$[2] were investigated. The intention was to build lighter batteries and replace the harmful lead and cadmium. In the beginning, lithium was used for cathodes in its solid metallic form. But as metallic lithium suffers from dendrite formation, internal short circuits occurred whenever dendrites electrically connected anode and cathode side[3]. Therefore, metallic lithium was replaced by the Li-ion technology in the 1980s with the discovery of $LiCoO_2$[4]. Sony[5] introduced the first commercially available Li-ion battery in 1990[5] being used to power video camcorders. For anodes, carbonaceous materials especially graphites[6–8] were established. But although many improvements have been developed, there is still potential and need for further progress. Weight reduction, recyclability, environmental sustainability and well available resources are major issues. According to different research institutes, there are central strategy plans which determine the future development[9–11].

With ongoing digitalization, the development of microsystems for mobile devices and gadgets for various aspects of everyday life demands more powerful, cheaper and rechargeable batteries. For instance, since the introduction of the first mobile phone in 1983[12] the number of mobile devices has increased exponentially. According to the Ericsson report[13], the worldwide number of smartphones amounted 4.4 billion in November 2017. Since mobile phones are being used every day, their battery performance is a crucial criterion. Current mobile phones are equipped with a powerful processor, a big touchscreen and many sensors but a comparable poor battery which has to be charged every one or two days. Charging costs time and impairs mobility and for most mobile phones today a broken battery is an economic total loss as a battery exchange is complicated and expensive or not even provided. Next to mobile phones, notebooks and tablet PCs also require high-power batteries.

Traction batteries for automobiles and other vehicles represent a second growing market. Consumer relevant points regarding cars are fast chargeability and capacity to compete with conventional petrol-fueled cars. Refueling with gasoline lasts around three minutes and the range averages around roughly 600 km. Present electric cars also reach 500 km[14], but charging lasts one hour or more[15,16]. Only considering its use, electrical engines are emission-free, silent and many mechanical parts like gearing mechanism, exhaust system etc. are not needed anymore, which saves weight to compensate the extra mass of the heavy batteries which weight up to 600 kg[17]. But fabrication of batteries as well as incidental disposal from sorted out modules are not emission-free, and of course the energy for charging has to get transformed elsewhere. Moreover it has to be considered that the installed batteries pose a danger in case of accidents or failures resulting in spontaneous ignition[18,19]. Like fossil fuels, also certain battery materials will become rare as their demand increases.
The aim of this work is to characterize and evaluate the properties of selected potential materials for next generation energy materials with focus on rechargeable batteries. The experiments were essentially conducted by methods of scanning and transmission electron microscopy. The practical part of this work comprises five topics:

- Chapter 3: The characterization and subsequent improvement of recently developed silicon microwire anodes for high-capacity batteries is presented. Pristine and cycled devices are examined to monitor their shape and state. Key properties that are investigated are defect formation, degradation and its dependence on process parameters (e.g. charging rate and temperature) and the influence of applied modifications. Besides, related experiments on non-battery Li-Si phases are presented, which were conducted to provide additional information about the system Li-Si, especially about crystallinity and feasibility of handling in a TEM.

- Chapter 4: Next to crystalline silicon, other modifications of silicon are considered which are also suited for battery applications. Two modifications of an amorphous type, developed at the Department for Chemistry at TU Munich, and aero-silicon, synthesized on the basis of zinc oxide tetrapods at the Institute for Material Science at Kiel University, are investigated and discussed in terms of morphology, structure and composition.

- Chapter 5: Detrimental to certain common Li-ion batteries is the use of cobalt[20]. Regarding substitution of the rare cobalt, that is often mined under debatable conditions, spinel-type transition metal oxide systems with reduced cobalt content were developed at the Institute of Inorganic Chemistry at Kiel University. Three compounds namely $CoFe_2O_4$, $CoMnFeO_4$ and $NiFe_2O_4$ that are

used as paste electrodes are analyzed. The main aspects of these analyses are composition, distribution and stability of the transition metal oxide compounds.

- Chapter 6: Fundamental characterizations of carbon-sulfur compounds, recently developed at the Institute for Material Science at Kiel University, are presented in terms of stability of resulting cathodes and their compatibility in full cells. Current progress in sulfur integration as well as appropriate synthesis steps are discussed and concluded with a short outline of subsequent following steps.
- Chapter 7: Complementary to batteries, the hydrogen-based fuel cell is a promising technology for next generation energy supply. Energy gets converted by combustion of oxygen and hydrogen with only water as a byproduct. To obtain an environmental neutral process, hydrogen has to be extracted without combustion of fossil or nuclear fuels. This last section highlights recent results on Cu-In-S phases being potential candidates for energy-related processes, e.g. photocatalysis[21], and can be considered as further step to meet the aforementioned environmental demands. Basically, this ternary system represents mixtures of InS and CuS. Due to different synthesis parameters for the applied solvothermal synthesis, three different main phases have been identified: $CuInS_2$, $CuIn_3S_5$ and $CuIn_5S_8$. Their various morphologies, crystal structures as well as defects are discussed with respect to potential functional characteristics.

# 2 Experimental techniques

## 2.1 Scanning electron microscopy

Equipped with an electron source, this type of microscope allows to capture highly magnified images of small samples in order to determine size and shape. A focused electron beam is generated to form a probe which scans the sample line by line. The achievable magnification depends on the chosen acceleration voltage and the electron source. For each scanning point the sample-beam interaction will be detected simultaneously. Different signals most prominent secondary (SE), backscattered (BSE) and Auger electrons (AE) and X-rays were detected. Images usually were taken in SE-contrast mode that only provides information about the samples' surface. The image contrast principally arises from the signal intensity and depends on the surface orientation towards the beam and the detector. For a sample surface perpendicular to the primary beam, the resulting spotsize is smaller being beneficial for the final resolution (see Figure 2.1 a). By using the installed EDX detector, elemental mappings, linescans and point analyses were performed. For the interpretation of EDX data it is important to consider the interaction volume of electron beam and sample material. The information depth depends on the atomic number of the material and the applied acceleration voltage. Thus, elemental ratios detected for heterogeneous systems, e.g. the solid electrolyte interface (SEI) on silicon wires vary depending on the voltage and the layer thickness. SEM images presented within this thesis were conducted with a *Zeiss Gemini Ultra* field emission (FE)SEM, which has a field emission gun (FEG) cathode operated at 10-12 kV and a silicon drift detector (SDD) from *Oxford Instruments* for EDX analysis.

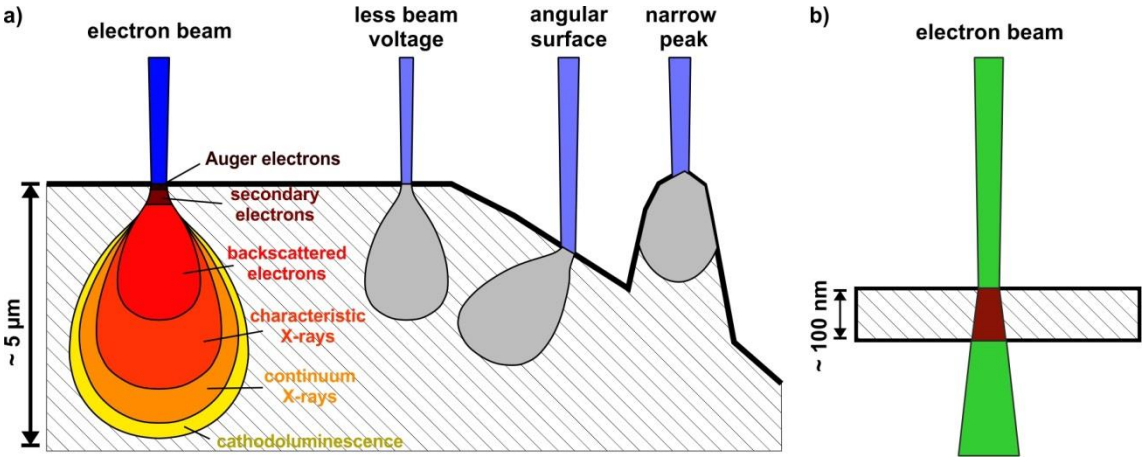


**Figure 2.1:** a) The interaction between electron beam and sample surface is described by an interaction bulb which contains specific regions. It is essential for interpretation of SEM images. b) For TEM it can be applied in a truncated manner (red part).

## 2.2 Transmission electron microscopy

Invented in 1933 by Ernst Ruska, the TEM represents the most versatile instrument for micro-and nanostructure characterization as it allows the determination of structural and chemical information of prepared samples (compare Figure 2.1a, b). Applied methods comprise selected area electron diffraction (SAED), precession electron diffraction (PED), high-resolution (HR)TEM and high-angle annular dark-field scanning (HAADF-S)TEM EDX mapping. Additionally, electron energy loss spectroscopy (EELS) and energy-filtered (EF)TEM were performed to examine the chemical environment. Since these are standard TEM techniques, they are considered as common knowledge and can be reread in standard textbooks[22–25]. Representing a special technique, PED is briefly explained in the following paragraph. TEM measurements were performed on three different microscopes: *Jeol Jem-2100* ($LaB_6$, 200 kV, $C_s$ = 1.0, *Oxford* SDD EDX detector), *FEI Tecnai F30 G² STwin* (FEG, 300 kV, $C_s$ = 1.2, *EDAX* EDX detector) both located at the TEM Center at Kiel University and *Phillips CM 30* ($LaB_6$, 300 kV, $C_s$ = 1.15, SDD EDX-detector) operated at the Max-Planck-Institute for solid state research (in the following simply abbreviated as MPI) in Stuttgart by Viola Duppel.

Precession electron diffraction[26]

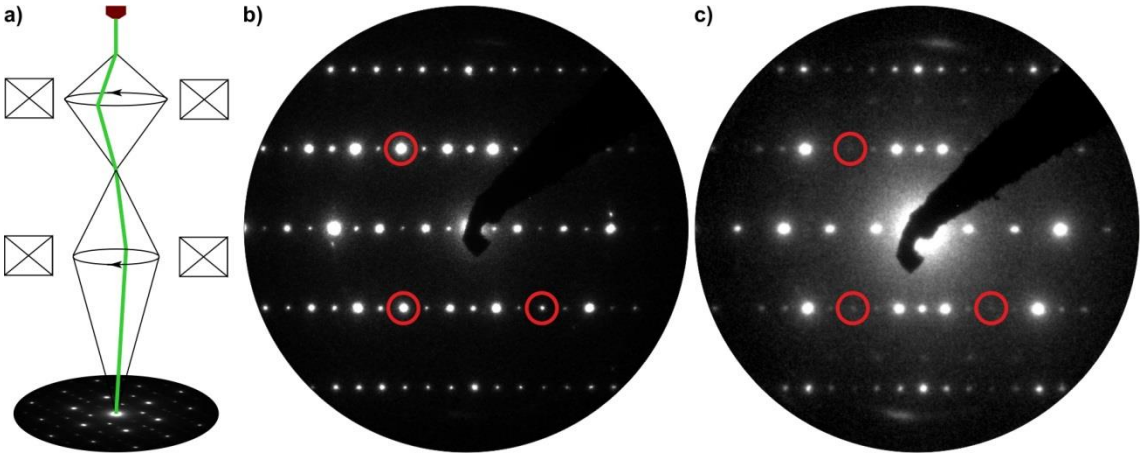


**Figure 2.2:** a) Precession movement of the electron beam. Comparison of diffraction patterns obtained by (b) SAED and (c) PED with exemplarily marked forbidden reflections.

In a TEM, diffraction contrast is obtained from elastic scattering of electrons by atoms of the specimen. In case of a crystalline material, its periodic lattice causes constructive interference observable as defined reflections in the resulting diffraction pattern. But their intensities do not necessarily represent the real structure since the effect of dynamic (multiple) scattering becomes more pronounced with increasing sample thickness. A technique to reduce dynamic scattering is PED. The electron beam gets deflected (angle ≤ 3°) periodically into a precession movement on a cone surface

(Figure 2.2 a). During precession, many off-axis diffraction patterns were recorded in order to process an averaged pattern and thus inhibiting the excitement of multiple beams. By following this procedure, dynamic scattering gets reduced due to its random character. The intensity of the primary beam is more pronounced and forbidden reflections are suppressed. In Figure 2.2, two different diffraction patterns obtained by SAED (b) and PED (c) are compared.

### 2.3 *In situ* heating

Chemical processes inside a battery are strongly influenced by temperature. Prominent examples are self-discharge and thermal runaway[27,28], which finally destroys the battery, and can subsequently cause harm to the surrounding environment. The TEM (from *FEI*) used in Kiel is equipped with a heating system, including a *Gatan 652 Tantalum* heating holder, a temperature regulating cooling water basin and a *Gatan Smart 900* temperature control unit. By this, *in situ* heating of the sample is supported up to a temperature of 1000 °C. Depending on the desired temperature, a suitable TEM grid has to be used in order to prevent melting. As rule of thumb, the maximum applied temperature should not exceed $^2/_3$ of the applied material's melting point which is considered as approximate lower energy barrier for noticeable diffusion processes[29]. Furthermore, the formation of eutectic alloys through contact of the sample with its holder as well as with the pole pieces of the objective lens has to be considered and avoided. Generally, heating deteriorates the image quality due to lattice oscillation of the sample material especially at high magnification and induces material expansion which causes minor changes of size and position of the sample and thereby impedes focusing on defined areas. If the grid is coated with a supportive carbon film/network, the carbon will partially get dissipated, which will subsequently deform its structure and by that will cause a drift of dispensed material.

### 2.4 Sample preparation

Depending on the chosen instrument, there are specific requirements regarding the sample. XRD machines used within this work were powder diffraction machines. Every sample, that was to be measured, was ground thoroughly to obtain a fine powder in order to prevent texturing effects[30]. Subsequently, this comes along with the loss of position information and a restriction to quantitative information.

For SEM, two prerequisites regarding the sample must be considered: vacuum stability and electrical conductivity. In the course of this work, mainly inorganic materials were investigated which, after careful drying, did not suffer from evaporation. Conductivity was critical, e.g. for $SiO_2$: During measurement, the sample material with low

conductivity got charged by the electron beam, which generated blurring and glaring artifacts on the obtained images. To overcome charging artifacts, coating with gold or silver or conducting tape was applied.

TEM, the most advanced applied machine, also requires a very thorough sample preparation. Electron transparency is of utmost importance, meaning sample thickness of about maximum 100 nm (depending on the atomic number of the material), which turned out to be very challenging especially for silicon microwires. The easiest and straight forward approach was to grind samples to a fine powder. As for XRD, it resulted in a partial or total loss of position information, depending on the ratio of final grain to feature size and further destruction of functional structures and morphologies. Due to the wires' design, fragments originating from the upper and lower part could be distinguished as they showed characteristic thickness features. To overcome the drawback of loss of position information, more precise techniques as described in the following were applied.

### 2.4.1 Focused ion beam milling

For preparation of very thin electron-transparent samples, FIB milling[31] is a well-suited method (Figure 2.3). This procedure comprises the mounted sample, a micro manipulator and an ion beam and is conducted in a SEM machine setup. The area of choice, that is to be extracted, is covered by platinum in order to protect and stabilize the final lamella. By cutting two trenches perpendicular to the sample's surface with a Ga-ion beam, a remaining lamella is obtained in between. It almost gets cut off the bulk, attached to a fine needle-shaped manipulator and lifted out afterwards. Finally, the lamella gets thinned by the ion beam to about 50 nm and attached to a TEM holder-compatible grid. All FIB procedures presented in this work were performed by Christin Szillus at the Institute for Material Science at Kiel University.

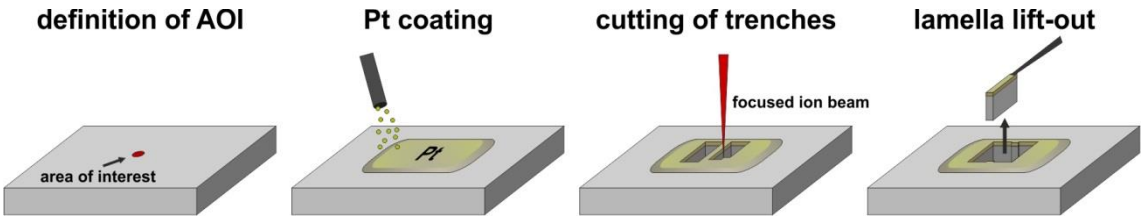


**Figure 2.3:** Schematic sequence of a basic focused ion beam-assisted preparation of a lamella.

2.4.2 Ultramicrotomy

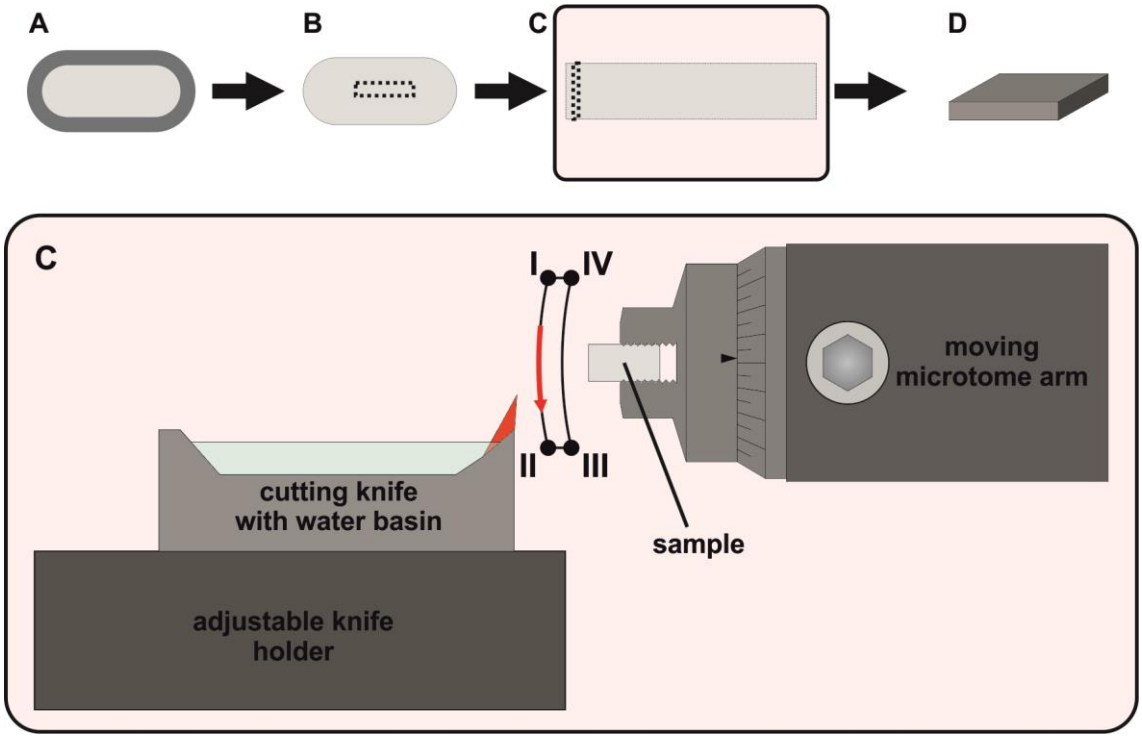


**Figure 2.4:** Ultramicrotome-assisted preparation of an embedded sample. The embedded sample is moved in a repeating cycle (positions **I**-**IV**). From position **I** towards **II** a thin slice is cut off by the knife (red) and caught in the water basin.

As a rather conventional but very useful technique, ultramicrotomy[32,33] provides very thin samples in a comparably short time (Figure 2.4). For fixation the sample is embedded in a compatible polymer (**A**) in a small water dissoluble capsule about 15 mm long and 5 mm in diameter. The polymer must not change the sample chemically or physically and it further has to provide similar mechanical properties for an effective embedding, especially for the final cutting. Polythiourethane (PTU)[34,35], purchased from Fluid-& Prozesstechnik GmbH (Waltershausen, Germany), which is a two-component polyurethane thermoset system, was utilized as it does not contain any solvent. Furthermore, its final hardness can be adjusted by the components' ratio and the hardening procedure. The embedded specimen is roughly cut with a wire saw (**B**) to fit the dimensions of the ultramicrotome holder. The resulting block with dimensions of about 1 x 1 x 5 $mm^3$ is mounted into the ultramicrotome holder (**C**), and both are adjusted to the cutting range of the blade. Depending on the specimen's hardness, a diamond or glass blade is used. Main parameters to modify are slice thickness (down to 40 nm) and cutting speed (slower for hard samples). During cutting, multiple thin slices are sheared off the sample (**D**) and float on the surface of a small water basin next to the blade for an easier separation and extraction.

### 2.4.3 Inert gas sample transfer

Especially air- and moisture-sensitive samples, e.g. Li or Na compounds, demand for a careful handling in $N_2$ or Ar atmosphere. The TEM column provides ultrahigh vacuum, but the transfer from a glovebox to the TEM usually includes contact to air. Therefore, a sealed bag is used to protect the sample. Inside the glovebox, the sample is mounted into the TEM holder and both put into a mechanically sealed bag. The bag is taken out of the glovebox and to the TEM. The sealed opening is put next to the TEM holder stage and a $N_2$ counterflow out of the TEM stage is started to avoid contact with air during transfer. Finally, the bag is opened partially next to the $N_2$ counterflow to quickly mount the holder into the TEM stage. Applying this procedure, the formation of lithium oxide was reduced proven by EDX analyses for $Li_{16.42}Si_4$ (see Chapter 3.3). Minimal amorphization does not inhibit detailed TEM examination since the occurring noisy contrast can be improved by, for instance, applying Fourier filtering techniques in HRTEM.

### 2.4.4 Solvothermal synthesis

To synthesize rare compounds, which do not form at ambient conditions, solvothermal syntheses[36,37] can be applied. The parameters temperature and pressure are changed to force the formation of metastable phases. The necessary starting chemicals are put into a PTFE (polytetrafluoroethylene) vessel and an agent is added, that increases the pressure with rising temperature. The PTFE vessel is closed with a fitting cap and put into a steel container, which is closed with a steel cap to reinforce the less pressure-resistant PTFE vessel. The final set-up is put into an oven to be heated and kept at elevated temperatures for several days or weeks. Supported by the agent, the pressure in the PTFE vessel increases as the temperature does. Starting from the Clausius-Clapeyron relation:

$$\frac{dP}{dT} = \frac{L}{T\Delta v}$$

With $\frac{dP}{dT}$ being the slope of the resulting curve at any point, *L* the specific latent heat, *T* the temperature and $\Delta v$ the specific volume change of the phase transition, the Antoine equation was developed as semi-empirical correlation:

$$log_{10}p = A - \frac{B}{C + T}$$

With this correlation, that includes the introduced component-specific constants *A*, *B* and C, the resulting pressure *p* at higher temperatures can be determined more precisely since the Clausius-Clapeyron relation is restricted to a linear relation between

pressure and temperature. The amount of the agent can be calculated roughly by applying the Antoine equation in order to prevent damage of the vessel by excessive pressure but still providing sufficiently high pressures to support the formation of respective Cu-In-S phases. Besides, careful handling and preparation of the vessels is essential to prevent explosions or release of hot steam during removal and opening. After the vessel has cooled down to room temperature, it can be opened to extract the obtained products. They are filtered by passing a fine frit and later rinsed with water, acetone and ethanol multiple times to remove remaining EN and other non-solid byproducts. Finally, the filtered particles are led to dry to obtain pure solid Cu-In-S particles.

# 3 Silicon-microwire anodes

## 3.1 Introduction

Based on pure silicon wafers, which are originally being used in the semiconductor industry to fabricate microchips, a promising type of battery electrode was developed by Dr. Enrique Quiroga-González et al. at the former group of General Materials Science at Kiel University[38–40]. Applied as an anode half-cell, superior capacities of 4200 $mAhg^{-1}$ have been realized, which are about a factor of eight higher than commercially available carbon based batteries in 2014[41]. The general fabrication process was worked out well to allow a constant manufacturing of electrodes, but their performance ceased after only a few charge/discharge cycles. Commercially available battery cells are advertised to be charged and used for up to 3000 times[42,43]. The example of mobile phones demonstrates that charging every day and considering their average lifetime of about 30 months[44] equals approximately 900 cycles. Electric cars present an even greater challenge as their employment is more versatile and the capability and attendance to recharge differs substantially: The usage profile of cars ranges from daily, short and long distances by commuters and trucks to rare use by car rentals or utility vehicles. A mobile phone can be used even while getting charged and if necessary there are supplying batteries (power banks) for charging on the move. But for a car, so far neither is possible.

The first working batteries containing silicon microwire anodes did only withstand a few charge/discharge cycles until the capacity dropped (see Figure 3.1, data provided by Dr. Hansen). Crucially, reasons for their early failure need to be identified in order to enhance their quality and develop competitive anodes and finally batteries.

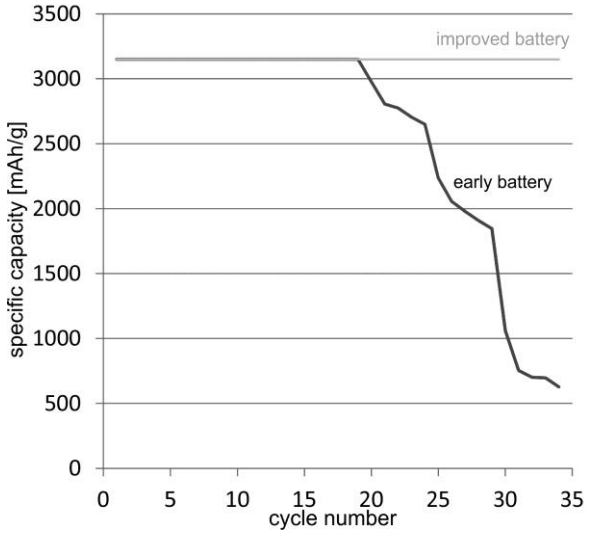


**Figure 3.1:** The first anodes showed a rapid capacity fading compared to (later) improved variants.

## 3.2 Secondary batteries

Chemical energy is stored in batteries to be converted into electrical energy being available on demand. Essentially, batteries can be subdivided into two classes: primary and secondary cells. Primary cells are intended for single use since a chemically irreversible decomposition occurs during discharge. They are suitable for infrequent and little power consuming use, e.g. in watches, electronic scales or pocket calculators, as they suffer from less self-discharge, have a lower prime cost and are less temperature-sensitive. Secondary cells are designed to be used multiple times. The occurring chemical reactions during discharge are reversible, meaning that the batteries can be recharged to be used again. Especially for frequently used devices, e.g. MP3-players, mobile phones and cars, this type of battery is favored since the higher prime costs are compensated and resources conserved upon multiple use.

### 3.2.1 General setup

Si-microwire electrodes chosen as anodes represent a half cell from a secondary type battery. To give an overview, the main components of a battery are briefly explained in the following section. Those, already present in the first galvanic cell, are: anode, cathode and electrolyte. Moreover, there are many supporting parts, e.g. separators, current collectors and housings[3].

#### Anodes

During discharge, the anode material operates as electron donator. Charge carriers (ions and electrons) moving to the cathode side are responsible for the current flow. The electrode potential is the basis and driving mechanism of a working battery. The electropotential series (listed in standard chemistry textbooks) gives an overview of the possible chemical elements. Per definition, the anode has a lower potential than the cathode. Common anode materials are depicted in Table 1.

#### Cathodes

The cathode represents the electron-accepting electrode. Bearing a lower potential, the applied material is chemically reduced, accompanied by an oxidation of the anode material as soon as the electrical circuit is closed. Common cathode materials are listed in Table 1.

#### Electrolytes

Mechanical stability, conductivity and the overall battery chemistry are strongly dependent on the utilized electrolyte. It basically consists of an ion salt which provides charge carriers (usually Li) and appropriate solvents to support the salt's mobility

through diffusion. Important characteristics of the electrolyte are ion conductivity and viscosity, which are controlled by its composition. Early galvanic elements featured a salt bridge between anode and cathode side to provide charge balance without direct contact between both electrodes, respectively their electrolytes. Otherwise, ion concentrations from both sides would balance and thereby neutralize the chemical potential. Modern batteries contain gel-like electrolytes and a separating membrane, which is permeable to respective ions. As discussed in Chapter 3.6, electrolytes are usually multi-component systems that have a large effect on the SEI characteristics and thereby on the long-term performance of the battery.

**Table 1:** Common anode/cathode material combinations and incidental voltage.

| Anode material | Cathode material | Voltage/V |
|---|---|---|
| C6 | $LiCoO_2$ | 3.6 |
| | $LiMn_2O_4$ | 3.6 |
| | $LiFePO_4$ | 3.3 |
| a-C | $LiMn_2O_4$ | 3.6 |
| Li4Ti5O12 | $LiFePO_4$ | 2.4 |
| Cd | NiO(OH) | 1.2 |
| Fe | | 1.3 |
| Zn | | 1.2 |
| MH* | | 1.6 |
| Pb | $PbO_2$ | 2 |

*metal hydride, $AB_x$: basically a mixture of transition (A) and rare-earth (B) elements.

### 3.2.2 Li-ion batteries

The general principle of Li-ion batteries (see Figure 3.2) is the usage of Li ions as charge carriers and their reversible insertion/extraction into/from a host matrix at the anode/cathode side. The three basic parts are anode, cathode and the electrolyte. To fit the chemical requirements of the active material (e.g. silicon), a suitable electrolyte composition has to be chosen to provide a good transport of the charge carriers and reduce degradation effects (see Chapter 3.6.3). Lithium is the lightest solid element (at room temperature) and due to its small size, it can be employed to achieve high energy densities depending on the storage capability of the host material at both the anode and cathode side. The separator between anode and cathode side is tailored to exclusively allow Li ions to pass. Initially, the battery is charged by applying a potential difference between both electrodes. A redox reaction between anode and cathode material occurs generating a flow of Li ions and electrons, which move towards the anode side. Hence, the Li ions leave the cathode matrix and pass the separator to be intercalated into the anode material, accompanied by an electron flow through the

external circuit. The battery is fully charged once the anode material's capacity for Li ions is obtained. Studies on Li-ion batteries revealed that charging to complete saturation of the electrode system strongly promotes aging[45,46]. To reduce aging, the practical capacity is usually limited to about 85 % of the maximum theoretical capacity[47]. If anode and cathode are electrically connected, a potential difference will build up allowing an external electron flow accompanied by and electrically compensated with Li-ion diffusion. The open-circuit potential (for examples see Table 1) is determined by the difference of the utilized materials' electrode potential and can be calculated from the electropotential series. It should be considered that the theoretically available voltage gets reduced by internal resistances, high load condition and decreasing state of charge.

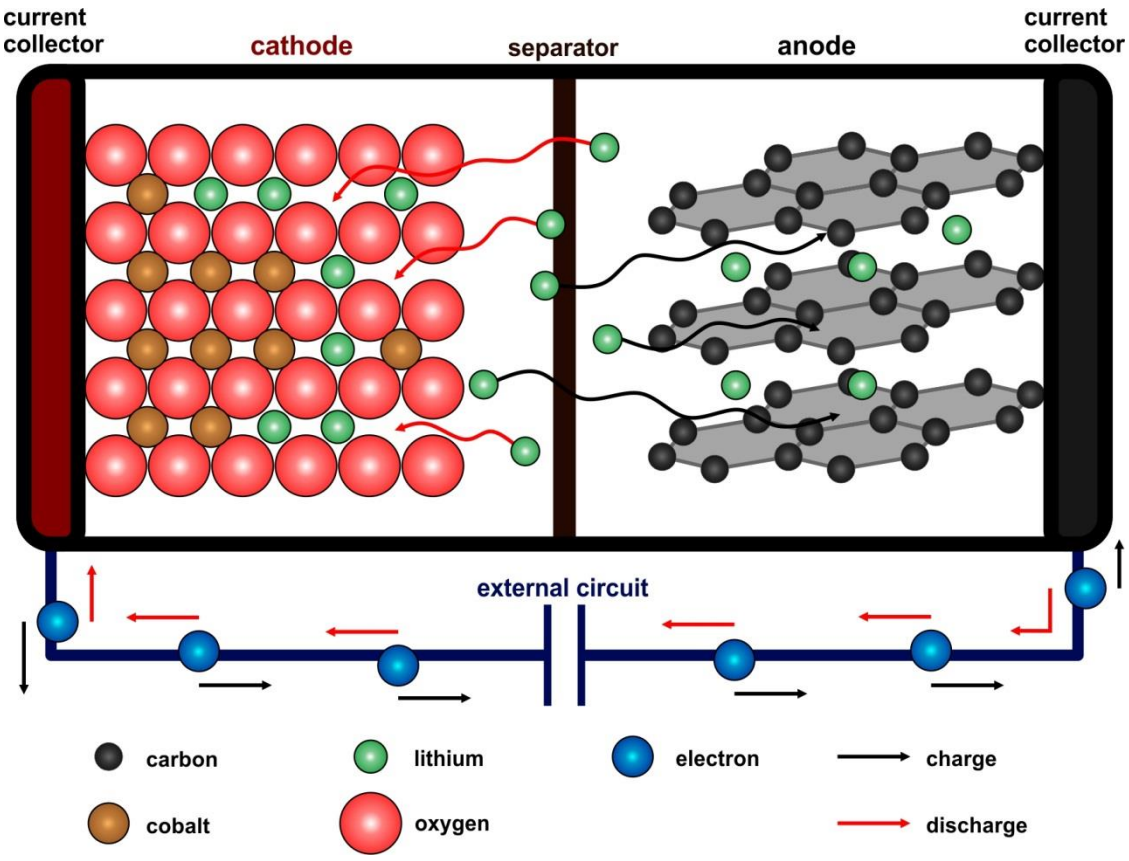


**Figure 3.2:** Schematic principle of a Li-ion battery. During charging/discharging, Lithium intercalates into the anode/cathode accompanied by an external electron flow.

### Li-Si compounds

The alkali metal lithium is the lightest solid element with a density of 0.534 g/cm³ and a body-centered cubic (bcc) structure (see Figure 3.3) with a lattice constant of 0.351 nm[48]. It is highly reactive[49] and in low concentrations usually present in form of minerals (e.g. amblygonite, lepidolite) and salts (e.g. lithium chloride), but does not

naturally occur in its pure form. Mining is tedious, since lithium salts are extracted from brines and concentrated by solar evaporation in prepared reservoirs where each period lasts up to two years[50]. According to the USGS report of 2017, the highest reserves and mine productions were calculated for Chile, China, Argentina and Australia[51]. Before lithium was utilized for batteries, there were only few applications, e.g. for medication against bipolar disorder and depression[52,53], military weapons (conversion to tritium[54]) or optics ($Li_2CO_3$, $Li_2O$[55]). But, with the enormous increase in fabrication and demand for Li-ion batteries starting in the 1970s[56,57], the value of lithium increased as well.

Silicon on the contrary, is the second most frequent element in the earth's crust[58]. It is a semiconductor with a diamond cubic crystal structure (see Figure 3.3) and a high melting point of 1410 °C. The lattice constant amounts 0.543 nm and the interatomic distance is 2.35 nm[59]. For extraction $SiO_2$ gets reduced in a simple process with carbon and depending on the field of application further refinement steps are applied, e.g. the Siemens procedure (treatment with $HSi_3Cl$), or zone refinement[60]. Main applications are glass fabrication, production of wafers for the semiconductor industry or usage as additives in compounds, e.g. Al-Si[61] or steels[62].

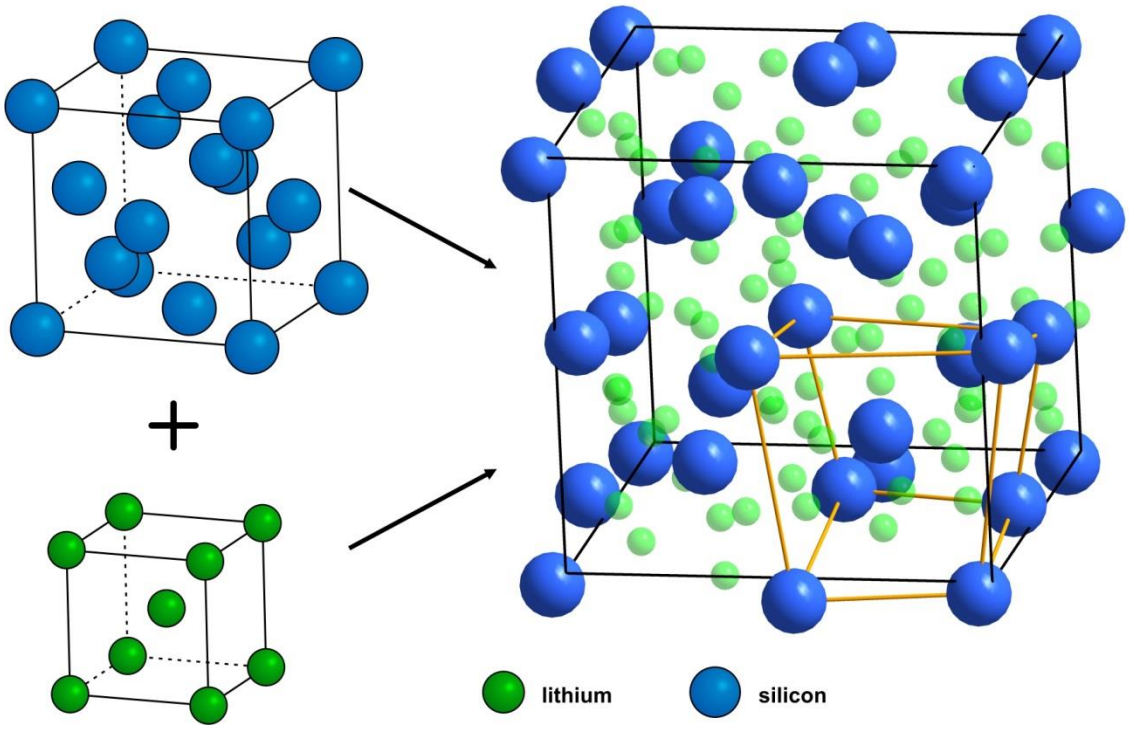


**Figure 3.3:** Lithium and silicon (left) were found to form many different compounds, e.g. $Li_{15}Si_4$ (right). A distorted subcube is sketched with yellow edges. The dark blue silicon atoms are the central atoms of those subcubes. For pure silicon the atoms on tetrahedral positions are outlined in darker blue.

The binary Li-Si system bears many stable and metastable stoichiometric phases listed in Table 2. Established and structurally characterized phases[63,64] considered within this part are $Li_{13}Si_4$[65], $Li_{15}Si_4$[66–68], $Li_{4.11}Si$[69] and $Li_{22}Si_5$[70]. In case of the Li-Si anode, a direct phase determination was rarely possible due to the restriction to delithiated Si wires and the high sensitivity of Li-Si phases. In general, during lithiation of the anode the initially pure and crystalline silicon absorbs Li and forms amorphous and rarely crystalline compounds. In Figure 3.3, as a showcase, crystalline cubic $Li_{15}Si_4$[71] is depicted to demonstrate occurring lattice distortion of silicon after Li uptake. Principally, its resulting unit cell is a distorted variant of a bcc cell doubled in all three dimensions with a lattice constant of 1.06 nm and interatomic distances for silicon with a minimum of 0.45 nm. Each silicon atom is coordinated by a lithium octahedron with two different Li-Si bonding lengths and those octahedra are connected via edges and faces. Cubic silicon exhibits eight silicon atoms per unit cell, for $Li_{15}Si_4$ it is 16. Taking into account the lattice constants, the volume for $Li_{15}Si_4$ is about a factor of $\left(\frac{1.06}{0.543}\right)^3 \cdot \frac{8}{16}$ = 3.72 higher than for pure silicon. Practically, for this type of battery a maximum expansion factor of four was observed[72,73]. Furthermore, many studies revealed that crystalline Li-Si phases are detrimental for a batteries long-time performance. It was shown that frequent phase transitions increase internal stresses and finally cause degradation, and should be avoided[66,74].

**Table 2:** Phases in the system Li-Si and respective space-groups.

| Composition | Space-group |
|---|---|
| $Li_{22}Si_5$ | F4-3M, F23 |
| $Li_{21}Si_5$ | F4-3M |
| $Li_{17}Si_4$ | F4-3M |
| $Li_{16.42}Si_4$ | CMCM |
| $Li_{15}Si_4$ | I4-3D |
| $Li_7Si_2$ | PBAM |
| $Li_{13}Si_4$ | PBAM |
| $Li_7Si_3$ | R3-MH |
| $Li_2Si$ | C12/M1 |
| $Li_{12}Si_7$ | PNMA |
| LiSi | I41/AZ |

### 3.3 First characterization of Li-Si compounds

Different from pure silicon samples, which are electron beam-stable and highly inert, Li compounds are highly moisture- and air-sensitive and demand for careful handling. Thus, TEM experiments on Li-containing samples were conducted prior to the battery experiments to examine the feasibility of handling sensitive Li compounds in the TEM and record first data. By that, occurrence of crystalline Li-Si phases and their resistance against the electron beam could be studied in advance to facilitate determination and analysis of compounds formed through lithiation. Furthermore, the inert gas sample transfer (see Chapter 2.43), a procedure to handle sensitive samples, which has been developed at the MPI Stuttgart, was adapted to be applied at the facilities at Kiel University. The first investigated compositions were: a compound with the stoichiometric formula $Li_{15}Si_4$ due to the net weights, and $Li_{16.42}Si_4$, both synthesized by Zeilinger et al.[69]. Respective TEM experiments were conducted at the TEM facilities of the MPI Stuttgart by Viola Duppel.

$Li_{15}Si_4$

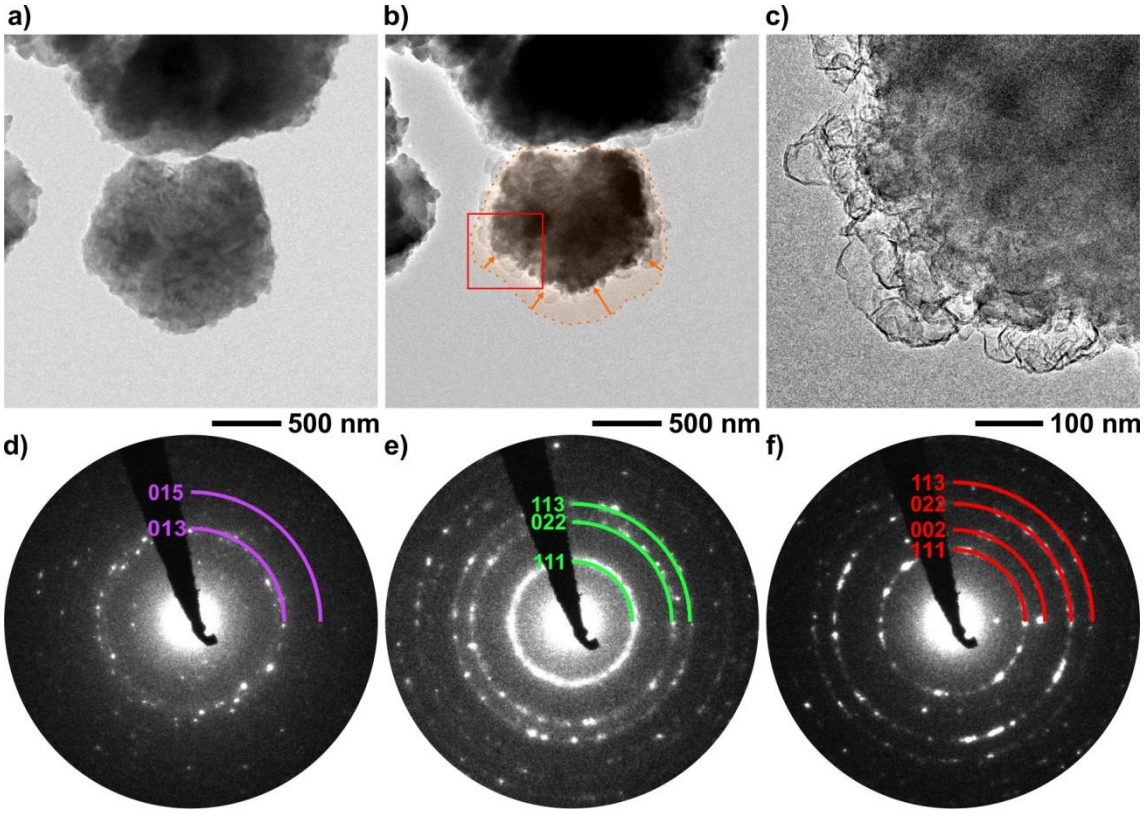


**Figure 3.4:** a) Li-Si particle after first image. b) Oxidation to Si and volume decrease of the particle at the center after beam irradiation. c) Magnified view on area marked in (b) shows $Li_2O$ shells at the particle's edge. d-f) SAED patterns for (a-c) depict microstructural changes as Li-Si (d) gets oxidized to recrystallized Si (e) and $Li_2O$ (f) by beam irradiation, documented by corresponding indexed reflection rings.

As already reported for other Li compounds[68,75] the herein investigated samples were very beam-sensitive. Depicted in Figure 3.4, beam-exposed particles were damaged after a short time. The particle agglomeration shown in Figure 3.4 a shrank about 15 % (in projection) compared to Figure 3.4 b. By SAED, microstructural changes are highlighted as initially present $Li_{15}Si_4$ (Figure 3.4 d) is oxidized to silicon (Figure 3.4 e) and Li did immediately oxidize. At higher magnification the resulting $Li_2O$ at the edges of the particle is visible as shown in Figure 3.4 c. Respective EDX measurements do only display oxygen since the utilized detector is not technically able to detect Li. Here, a dedicated windowless detector (to eliminate X-ray absorption) with a low zero width (< 30 eV, to enable detection of Li X-rays) is required. The oxygen is assumed to originate from initially present $SiO_2$ due to surface-oxidized silicon. The SAED pattern (Figure 3.4 f) from the respective region contains reflections arranged in rings, typical for a polycrystalline material (in this case the small $Li_2O$ fragments). Further calculated d-values correspond to reference data for cubic $Li_2O$[76].

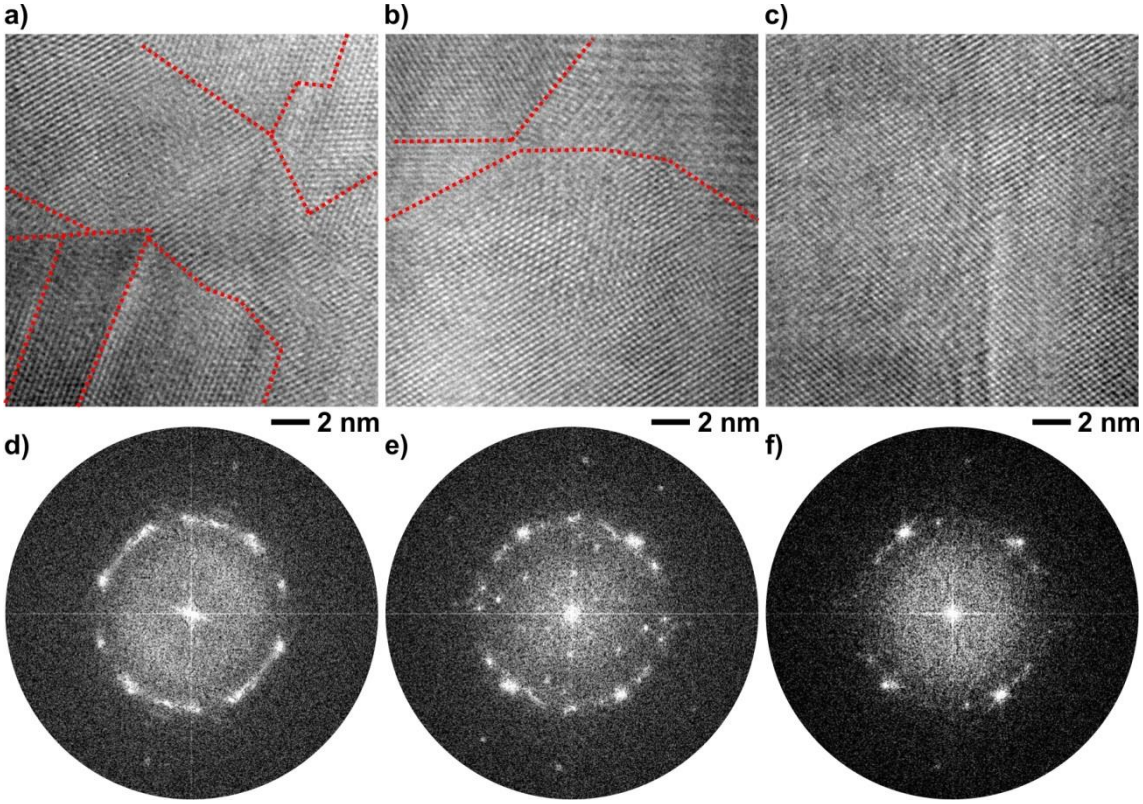


**Figure 3.5:** a-c) HRTEM micrographs and (d-f) corresponding FFT patterns depict the increasing symmetry of silicon after beam-induced recrystallization from $Li_{15}Si_4$.

After modification by the electron beam, near to pure silicon was formed. A study of its microstructure is presented in Figure 3.5 a-c. After the extraction of lithium, the remaining atomic structure of silicon is not favorable anymore and recrystallizes to

reduce its free energy as already reported by Park et al.[77] for low-dimensional Si-types. HRTEM micrographs from three different positions depict the occurrence of defects which remained after recrystallization. EDX measurements display pure silicon and the observed d-values correspond to cubic silicon[59]. From (a) to (c) the beam intensity during recrystallization decreased: Position (a) was the first to be analyzed, thus, it was directly exposed to the beam. Recrystallization occurred in short time at high beam intensity, whereas in parallel, position (b) next to it was only exposed to a fraction of the beam power resulting in slower recrystallization. Position (c) was irradiated with low intensity for even longer time and recrystallization also proceeded slower. Consequently, the defect (red dotted lines) concentration decreases from (a) to (c). Associated calculated FFT patterns (Figure 3.5 d-f) depict the increasing crystallinity starting with multiple small domains, which form rings (Figure 3.5 d) to end up with less and bigger domains and concentrated reflections (Figure 3.5 f)

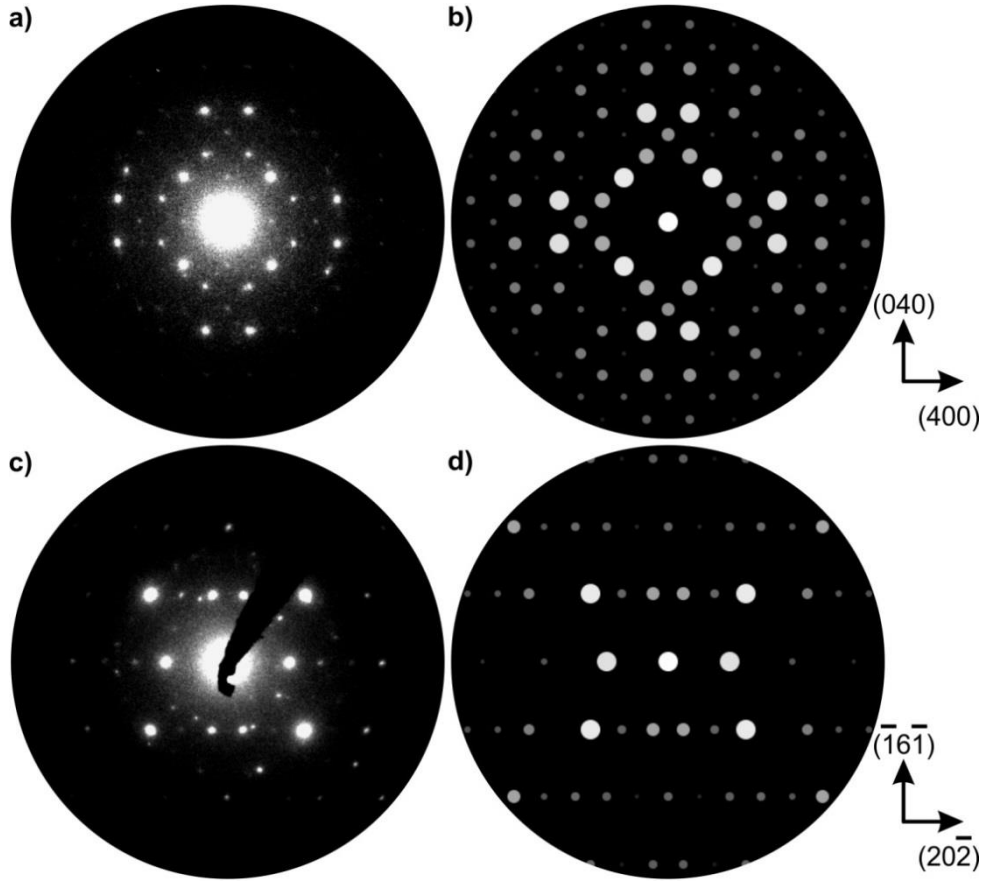


**Figure 3.6:** a, c) PED patterns from $Li_{15}Si_4$ for zone axes [001] and [313]. b, d) Corresponding simulated ED patterns.

Although $Li_{15}Si_4$ is a very volatile compound, a careful adjustment of the electron beam prevents severe damage of the sample material. At a small beam spot size and in SAED mode measurements were rendered possible since the beam intensity for this

technique is reduced due to the parallel beam mode. To reduce the beam exposure even further, PED was applied. A rough alignment of the sample is sufficient since slight deviation from the exact zone axis can be compensated by the beam precession. Recorded PED patterns are displayed in Figure 3.6: (a) represents the [001] direction for $Li_{15}Si_4$. Compared to the simulation based on reference data[71] (Figure 3.6 b) it still contains dynamic reflections, e.g. the four spots next to the primary beam representing (002) and (020) which are not allowed for kinematic scattering. Nevertheless, the relative intensities agree well with the simulation. The pattern from Figure 3.6 c can be assigned to the [313] direction of $Li_{15}Si_4$ (Figure 3.6 d). Here, slight dynamic reflections also remained.

$Li_{16.42}Si_4$

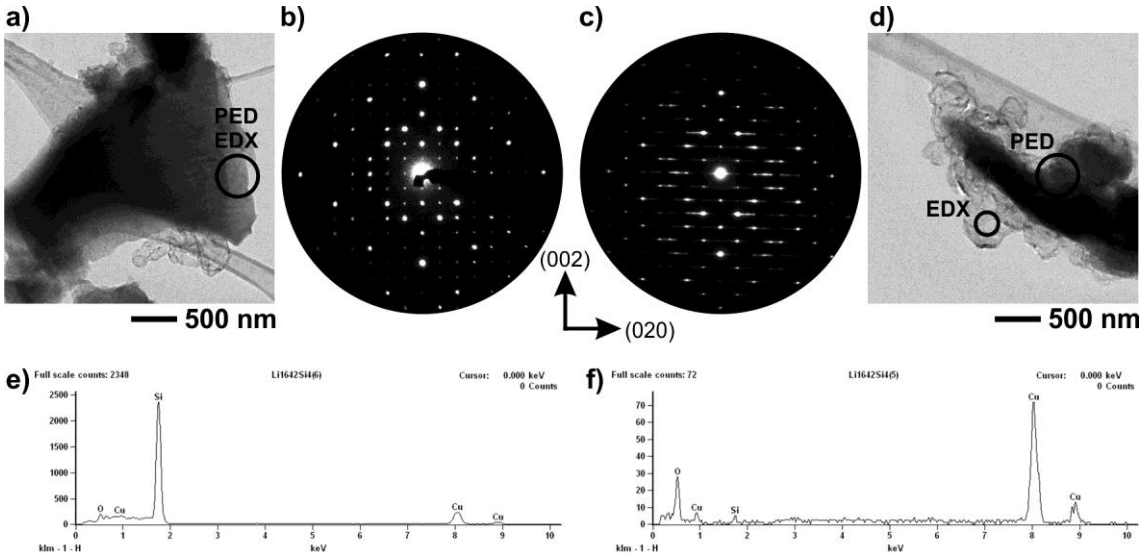


**Figure 3.7:** a) BF-TEM image of a wedge-shaped $Li_{16.42}Li_4$ particle. b) Experimental PED pattern of the [100] zone axis from the position marked in (a). c) SAED pattern from the position marked in (d) shows diffuse scattering attributed to planar defects. d) Beam-induced agglomeration of $Li_2O$ shells at the sample's surface. e) EDX spectrum from the circled position in (a). f) EDX spectrum from the position marked in (d).

The exact stoichiometry of this compound was determined by Zeilinger et al.[63] from phase transitions detected through differential scanning calorimetry and powder XRD results. Obtained by annealing at 610 °C, it was assigned as high-temperature phase, which was found to slowly decompose below 470 °C. As demonstrated by following TEM micrographs, the compound was successfully transferred to the TEM before considerable decomposition deployed. Ground in an agate mortar, particles of several micrometers in size (see Figure 3.7 a) were obtained. TEM measurements were performed at the thinner edges of the wedge-shaped particles, which have been tilted and aligned towards the electron beam. Figure 3.7 b shows an exemplary PED pattern,

which corresponds to the [100] direction of $Li_{16.42}Si_4$. The corresponding EDX spectrum (Figure 3.7 e) does only show silicon since lithium cannot be detected. As for $Li_{15}Si_4$, decomposition occurred caused by the electron beam. Formation of $Li_2O$ shells (see Figure 3.7 d) at the particles' surface was observed accompanied by lattice transformation apparent in diffuse scattering in the corresponding SAED pattern (Figure 3.7 c). An EDX spectrum from the edge (Figure 3.7 f) depicts the absence of silicon and a high oxygen concentration being assigned to the presence of $Li_2O$. The copper peak arising from the utilized copper TEM grid is strongly emphasized since the count rate is much lower (compare scales).

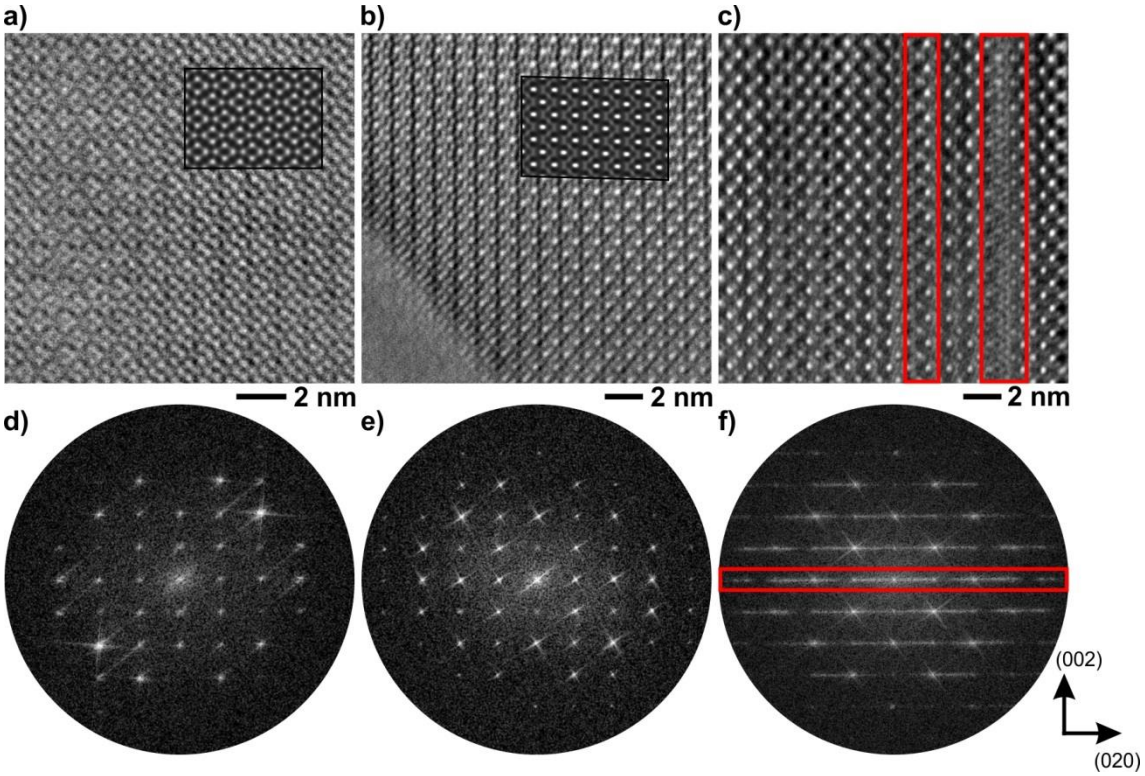


**Figure 3.8:** HRTEM study at the edge of a $Li_{16.42}Si_4$ particle oriented along zone axis [100]. a, b) Micrographs from two different positions with corresponding simulations in insets and calculated FFT patterns (d, e). c) HRTEM micrograph from a comparable position after high-intensity beam irradiation shows preferentially oriented defects (in red boxes). f) FFT pattern calculated from micrograph (c) with diffuse streaks in [010] direction.

The origin of the diffuse scattering in [010] direction is attributed to preferentially oriented planar defects depicted in a comparison of HRTEM micrographs at a thin initially crystalline edge. Two micrographs (Figure 3.8 a, b) with different patterns obtained at positions near the particles' edges are compared to simulated patterns and can be assigned (see FFT patterns, Figure 3.8 d, e) to the same zone axis [100], but with different defocus values: $\Delta f$ = -52 nm (a) and $\Delta f$ = -90 nm (b). For both simulations

the thickness was determined to 10 nm. A third micrograph (Figure 3.8 c) was recorded after beam irradiation. Planar defects marked by red bars were identified. They were also detected by diffuse streaks in the corresponding FFT pattern (Figure 3.8 f) which is related to the SAED pattern from Figure 3.7 c.

### 3.4 Si-microwire anodes

After recognizing the vast potential of silicon microstructures in the field of batteries, considerable efforts were made to optimize their geometry (explained in detail in Chapter 3.4.1), stability and reproducibility. As a charge carrier acceptor/donor, the anode has to adsorb ions efficiently and provide reversibility for many cycles. Therefore, layered or framework materials like graphite[78,79] and spinels[80,81] (Chapter 5) are favored due to their large surface area combined with a high structural stability. The Si-microwire anode exhibits an array of ordered Si microwires (see Figure 3.9 a, b) that feature a large surface area and can adsorb a high amount of Li ions by forming Li-rich Li-Si compounds. Compared to metals, the semiconductor silicon has a lower electrical conductivity at room temperature, which limits charging speed and enhances degradation. As a remedy, the backside of the wire structure is plated with a copper layer, which works as a current collector.

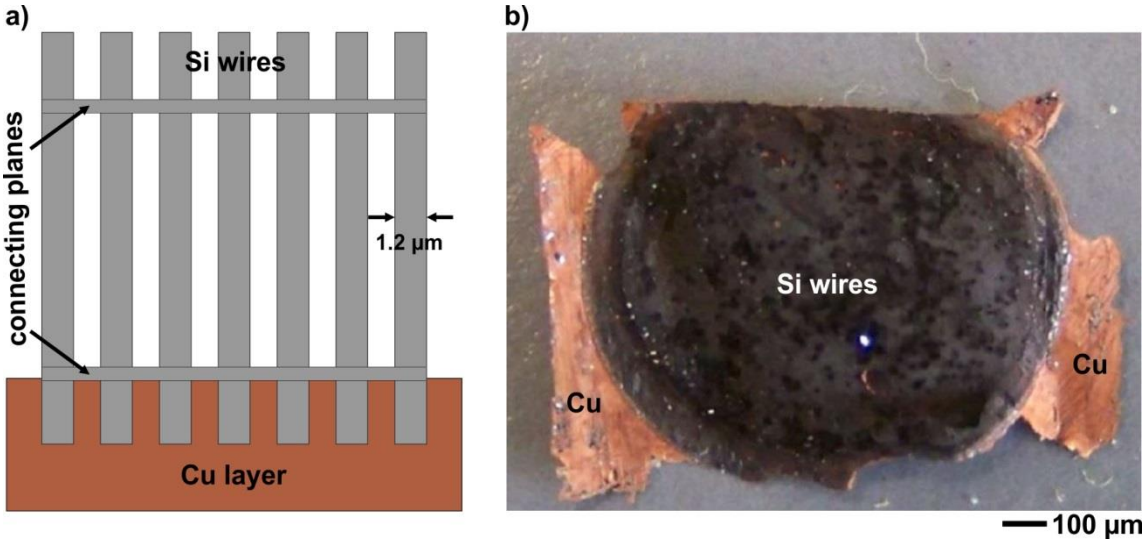


**Figure 3.9:** a) Schematic of a Si-microwire array with connecting planes and a backside copper layer. b) Exemplary anode before charging.

During lithiation, structural changes of initially crystalline silicon occur, as discussed in Chapter 3.6. Crucial for a long-term performance and the profitable application of a battery is the reversibility of the occurring chemical as well as physical processes during discharging. A major issue is the influence of the evolving SEI[82,83] on the anode (and cathode) stability. A lot of research is done in this field but still fundamental

processes are not yet fully understood. Thus, differential cycling conditions and SEI compositions are examined in Chapter 3.6 in order to compare resulting anode performances.

### 3.4.1 Fabrication of Si-microwire anodes

The underlying process for etching silicon was developed by Föll and Lehmann[84] in 1990. In a top-down approach, an array of aligned microwires is obtained by electrochemical etching of a standard p-type silicon wafer shown in Figure 3.10. The regular pattern is obtained by a pre-structuring step, followed by KOH etching, which creates a pattern of inverse pyramids with their tips pointing into the wafer. The pyramids' faces are (111) planes, which were preferentially etched. Subsequently, the faster etching along <111> enables pore etching being exploited to finally obtain a free-standing microwire array.

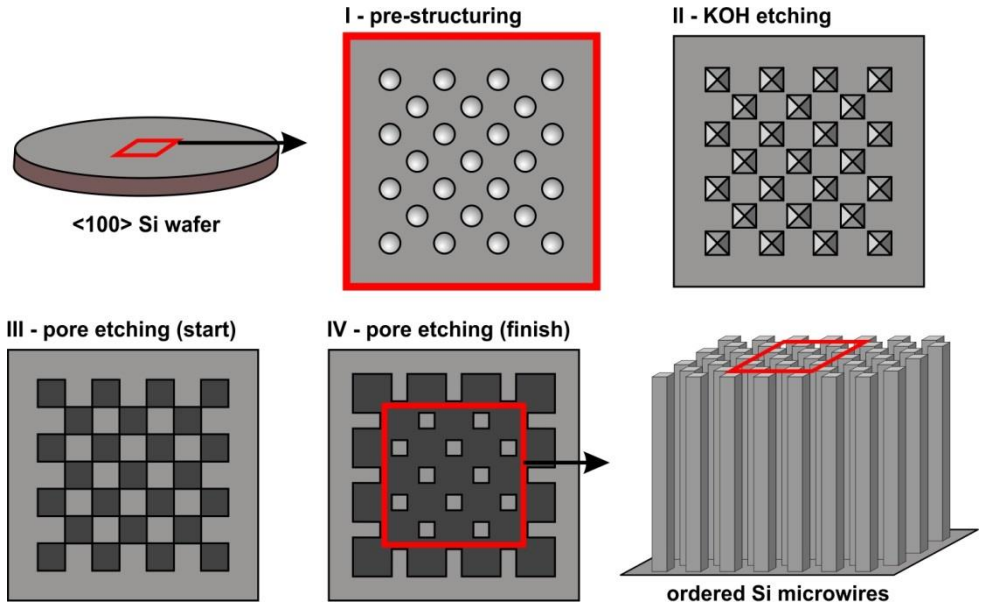


**Figure 3.10:** Schematic draft of the etching procedure of a Si wafer to obtain an ordered Si-microwire array.

The process parameters were optimized by Dr. Enrique Quiroga-González and Dr. Sandra Hansen at the Institute for Material Science at Kiel University[40] in order to fabricate stable arrays. A unique feature of this new type of anode is its wires' geometry. Thin (concerning the cross-sectional area), long wires with small distances in between supply a large surface area, which enables high absorption rates for Li ions. But with such a high aspect ratio, the wires become structurally instable[38] as they tend to bend or even break during charging/discharging. Moreover, if the distances are too short or the filling factor is too high, occurring volume expansion during charging will cause severe problems[85]. Due to the adsorption of Li ions, the resulting high pressure

will eventually pulverize the wires. The wires' length as well as their thickness is governed by the etching process. The best compromise was reached by fabricating wires with a cross-sectional area of 1.2 x 1.2 µm² and 70 µm in length. Bending and agglomeration was reported for free-standing wires resulting in a capacity decrease. This was overcome by a special etching profile, which leaves two connecting planes (see Figure 3.9 a) by applying a reduced etching rate over a short time. During cycling, those planes vanish due to an emerging SEI. Recent and hereby investigated anodes were also fabricated by Dr. Hansen[86].

## 3.5 Investigation of uncycled anodes

Through an innovative fabrication procedure (Chapter 3.4.1), a new and so far unexplored electrode type was developed. Elementary chemical and structural changes inside the electrode during application in a battery have to be examined since so far no comparable system is available. This necessitates a fundamental description of the fabricated microwire array before considering cycled types. The first part of the project comprises the characterization of unlithiated silicon microwires. Basic approaches for a suitable sample preparation are presented, which have been developed to support an application of conventional TEM methods. The original cross-section of the single wires is 1.2 x 1.2 µm², being too big as it largely prevents electron transmission. Thus, sample thicknesses in the nanometer range are required.

### 3.5.1 FIB milling

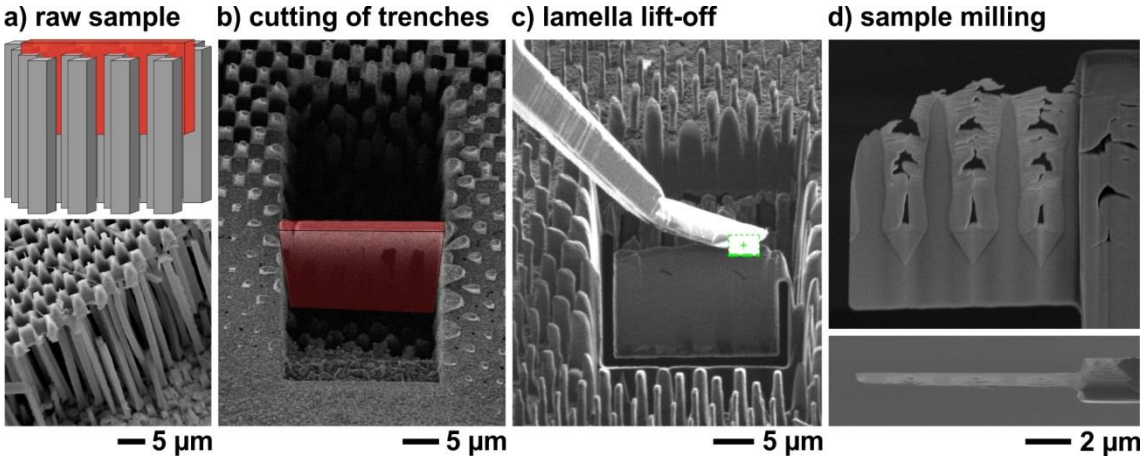


**Figure 3.11:** FIB milling procedure in detail. a) Microwire sample (bottom) and schematic position of lamella to cut (in red; top). b) Ion beam-assisted cutting of trenches to get a lamella (red) from the platinum-coated area of interest. c) Contacting and lift-off of the obtained lamella. d) Final thinning of the lamella to a thickness of 100 nm.

Already established for similarly sized samples[87], FIB milling is a well-suited procedure to prepare small structures or regions of bigger samples. The area of interest was

coated with platinum and a thin lamella, which contained four wire tips, was excavated. After final cutting, it was lifted out and thinned to appear transparent to the electron beam. The basic preparation steps are presented in Figure 3.11. Figure 3.11 a, b shows the position of the lamella which was oriented perpendicular to the array's surface. Being attached to the manipulator arm (Figure 3.11 c), the lamella was thinned to obtain four fragments of Si wires surrounded by platinum originating from the coating step of the FIB-assisted preparation (Figure 3.11 d). EDX measurements (Table 3) confirm the presence of platinum between the wires (pos. **III**) and nearly pure silicon wires with oxygen contamination of max. 3 at.%. SAED data, recorded from the wire fragments (Figure 3.12) displays their monocrystalline character. The depicted patterns correspond to the [100] zone axis of cubic silicon demonstrated by the simulated diffraction pattern. An exemplary HRTEM micrograph displays the silicon microstructure being monocrystalline for each wire.

**Table 3:** EDX results for the first FIB lamella (Figure 3.12).

| Element | Concentration in at.% | | | | | |
|---|---|---|---|---|---|---|
| | I | II | III | IV | V | VI |
| **Si** | 98.55 | 99.36 | 7.19 | 98.86 | 96.62 | 97.95 |
| **O** | 1.34 | 0.59 | 0.52 | 0.00 | 3.36 | 1.75 |
| **Pt** | 0.10 | 0.05 | 92.29 | 1.14 | 0.02 | 0.30 |

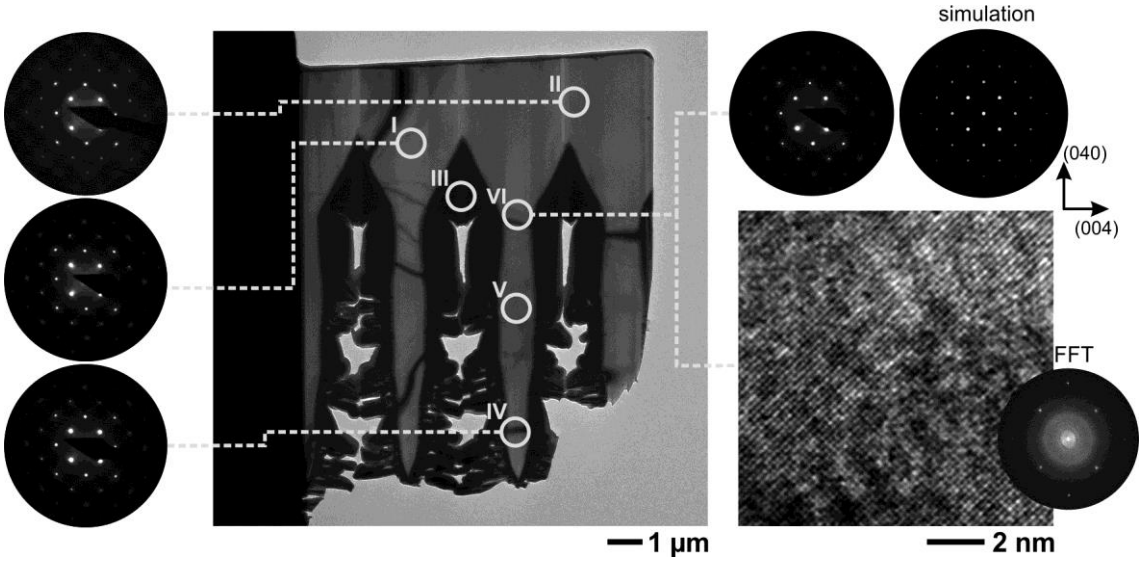


**Figure 3.12:** Analysis of the lamella shown in Figure 3.11 d. EDX results from position **I - VI** are listed in Table 3. SAED patterns from marked positions next to a simulated pattern (top right). Bottom right: HRTEM micrograph with corresponding calculated FFT pattern.

Unfortunately, only one FIB-assisted sample preparation was finished successfully. In most cases, the specimen got broken as Si wires were removed. Since the adhesive forces between Si wires and platinum coating were weak and did further decrease as their contact area shrank during milling of the lamella, the silicon fragments got partially detached from the fixed platinum parts. As sketched in Figure 3.13, without fixation the wires started to bend out of the lamella's plane. Here, continued thinning removed either the overlapping parts of the fragments, marked for selected positions, or even eventually the complete wire fragment. Furthermore, the atomic deposition is critical, especially for ensuing surface-sensitive samples. A bombardment with heavy platinum atoms causes atom implantation, which damages the initial surface and influences its chemistry. Even though Ga ions used for thinning are lighter, they are also smaller, diffuse faster into a surface and contaminate surface-near regions. Although only once, FIB milling was successfully performed to display the crystallinity of the silicon microwires. But in the following, surface-sensitive samples in particular demand for cleaner and less destructive methods.

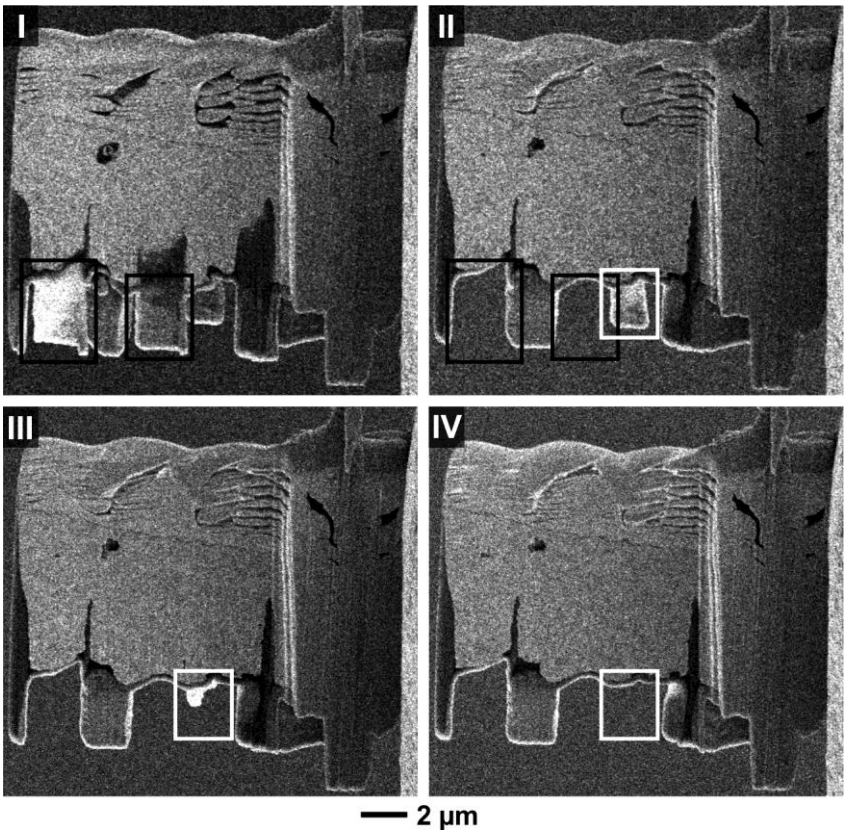


**Figure 3.13:** From **I** to **IV**: Depletion of silicon-wire fragments from the surrounding platinum during FIB milling, marked by black and white frames.

### 3.5.2 Ultramicrotomy

An easier, but less precise method is the cutting by an ultramicrotome. Two different approaches were tested to prepare TEM-suitable cross-sections of silicon microwires: 1. embedding of a piece of an anode (Figure 3.14 a) and 2. embedding of loose wires (Figure 3.14 b).

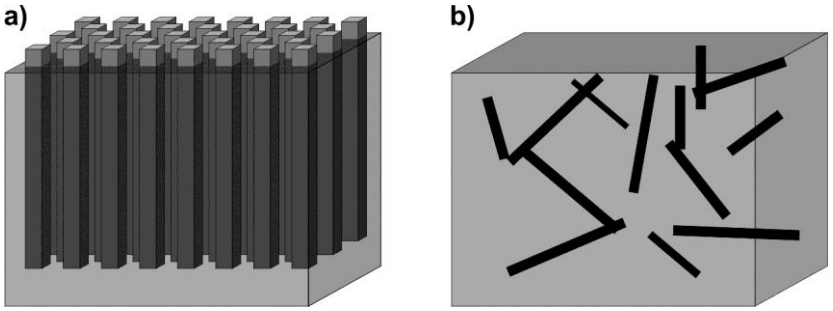


**Figure 3.14:** a) A piece of an ordered anode and (b) loose wires embedded in a polymer.

Since the cutting of a bunch of free-standing wires causes massive deformation, Si wires must be embedded. Otherwise many small, loose fragments are obtained from cutting, which are impossible to grab and place on a TEM grid. Embedding of a bigger piece of a wire array in epoxy resin, a commonly applied polymer[88], was insufficient. The embedding polymer did not totally enclose the array, but left voids in between. Also, the copper layer on the backside was too thick to cut it with the diamond blade. In a preliminary step, the copper layer was thinned by pure chemical etching in a low-concentrated sodium persulfate solution[89]. The penetration of the polymer into the array was forced by evacuation in a small vacuum vessel to about -0.5 bar. Still, the preparation of the vacuum-treated compound was unsuccessful due to remaining voids, which had reduced adhesion between polymer matrix and microwires. In the cutting step, many broken pieces were obtained instead of slices. Softer, more viscous polymers were expected to be more suitable for embedding as they provide a better infiltration into the structure. An array of microwires was covered in the ink of a text marker and led to dry afterwards. Good coverage of the remaining film is demonstrated by the SEM image (see Figure 3.15 a). It turned out that soft polymers suffered from high deformation during the cutting process and consequently the silicon wires got detached.

To avoid the presence of remaining voids, silicon wires were scratched off the copper backside (see Figure 3.15 b) and the resulting free arrays were ground to obtain many smaller packages and even single loose wires. Similar to the previous anode piece, these loose wires were embedded in a polymer. Due to the high amount of Si wires obtained from scratching and their random distribution in the polymer capsule, many wire cross-sections were found by investigation of the ultramicrotome-cut slices.

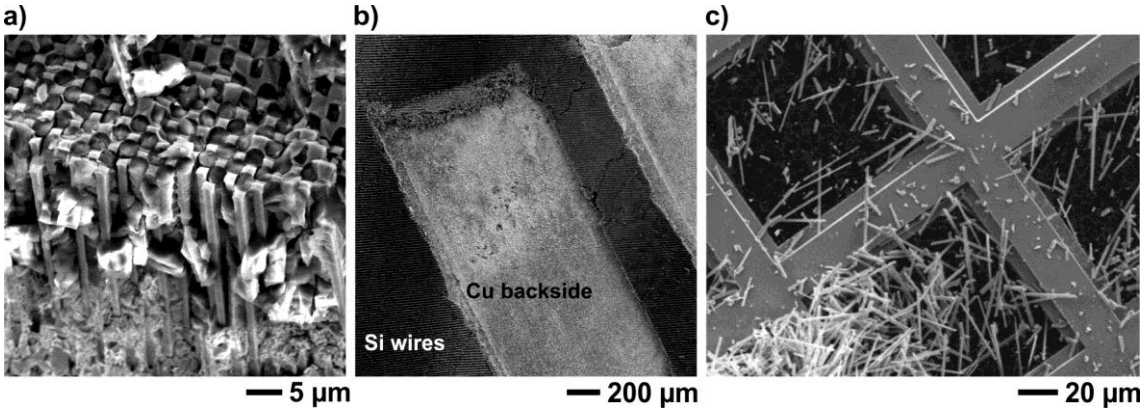


**Figure 3.15:** SEM images of (a) Si wires covered by a soft polymer, (b) a scratched sample and (c) loose Si wires and fragments on a TEM grid.

Since penetration into small interstitials was not necessary, the more viscous PTU was used, which is a two-component polymer that was mixed in a defined proportion (mass:hardener = 4:3) to make it as hard as possible. The wires were put into the liquid mixture and it was stirred for a homogeneous distribution of the wires. A small vacuum chamber was used to pull out remaining air, which was located at the interface of Si wires and polymer and decreases adhesion between both components. For solidification, the mixture was put into small water-soluble polymer capsules and heated. Next to the composition of the polymer, the heating procedure also influences the final hardness and was tested. Best results were obtained for a capsule which was heated for one hour at 80 °C. After heating, it was left to cool down a few minutes and put into a hot water bath to dissolve the capsule wall. The embedding procedure was followed by a rough cutting step to obtain an ultramicrotome-suitable sample.

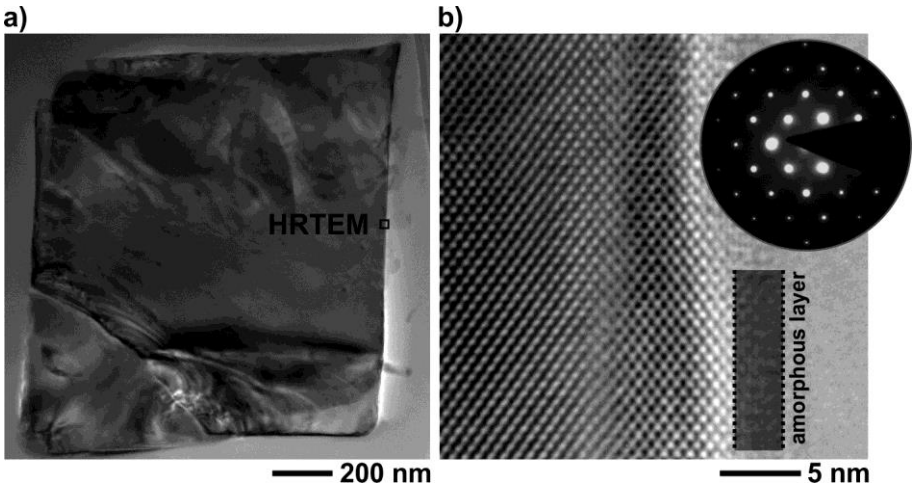


**Figure 3.16:** a) BF-TEM image of an ultramicrotome cut with an embedded Si-wire fragment. b) HRTEM micrograph and corresponding SAED pattern from the region marked in (a).

For that, the remaining polymer piece was cut with a diamond wire saw to obtain sufficiently small blocks (about 1 x 1 x 10 $mm^3$) for subsequent cutting by the ultramicrotome. Finally, slices with a thickness of only 50 nm were achieved, well suited for HRTEM analysis with an estimated thickness limit of roughly 100 nm. Still, occurring forces during cutting were high so that many wire fragments got ripped out of the polymer leaving holes, but some of them remained inside the polymer matrix. The depicted wire cross-section (Figure 3.16 a) is square-shaped due to a cut perpendicular to the wire's longitudinal axis. The HRTEM micrograph as well as the SAED pattern in Figure 3.16 b depict an overall single crystalline structure. The SAED pattern fits to the [110] direction, which was expected due to type and etching orientation of the silicon wafer. Also visible in Figure 3.16 b, a 3 nm-thin amorphous layer was determined at the wire's surface, which was frequently reported for crystalline silicon: Being exposed to oxygen and moisture, silicon forms a native silicon oxide film, which saturates foremost at a thickness of about 1 nm[90–92]. Further exposure will promote local decomposition of silicon, which will cause a higher surface roughness.

Using FIB milling and ultramicrotomy, it was shown that the fabrication process is accurate, reproducible and provides overall monocrystalline Si microwires in a regular arrangement. A procedure to handle and characterize micro-sized structures was developed and successfully applied to investigate Si microwires by TEM. Unfortunately, both methods include steps in which the samples are exposed to air. Uncycled silicon wires are inert, but cycled samples contain remaining lithium and the complex and sensitive SEI, which gets oxidized[79,82,93] easily. In search of suitable preparation techniques for cycled wires, the approach of putting scratched and ground wires directly onto a TEM grid (see Figure 3.15 c) was chosen. Here, thorough grinding of bunches of wires is necessary as only single wires and smaller packets stick to the carbon film on the TEM grid. Again, the thickness of the wires turned out to be detrimental. Due to their high aspect ratio, wires preferably break cross-sectional, but keep their initial diameter.

## 3.6 Investigation of cycled wires

The performance of a Li-ion battery depends on many factors increasing its degradation in different ways. With the uncycled wires used as reference, structural and chemical changes after cycling under different conditions were evaluated. Variables, which were considered, comprise cycling speed, number of cycles, electrolyte composition and elevated temperature. The basic electrolyte applied in the first experiments (Chapter 3.6.1, 3.6.2) is *Selectilyte LP 30* purchased from *BASF*, which contains $LiPF_6$ solved in dimethyl carbonate (DMC) and ethylene carbonate (EC).

Sample preparation

In contrast to uncycled wires, the cycled wires are air-sensitive due to their complex surface being partially amorphous and covered by the SEI. Thus, preparation by FIB milling and ultramicrotomy was not suitable due to inevitable contact to air as depicted in the following example of a FIB lamella shown in Figure 3.17 a. As described in the previous chapter, it suffered from severe damage, but remaining fractions of wires are recognizable.

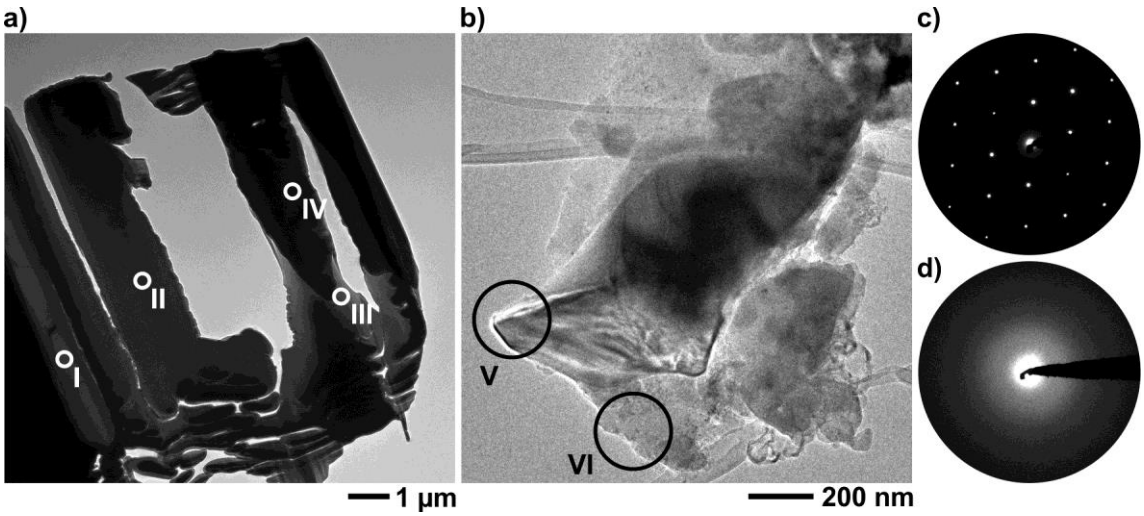


**Figure 3.17:** a) BF-TEM image of a FIB lamella which contains Si wires cycled once. EDX results for positions **I** - **IV** are listed in Table 4. b) BF-TEM image of Si-wire fragments after mechanical preparation with corresponding SAED patterns from (c) position **V** and (d) position **VI**.

Four different positions were measured by EDX to locally compare the oxidation levels, the impact of the FIB-assisted preparation and the propagation of the SEI (see Table 4).

**Table 4:** EDX results for the cycled wires-containing FIB-lamella (Figure 3.17 a).

| Element | Concentration in at.% | | | |
|---|---|---|---|---|
| | I | II | III | IV |
| **C** | 0.00 | 5.94 | 35.12 | 9.29 |
| **O** | 0.00 | 29.75 | 26.11 | 37.86 |
| **F** | 1.60 | 14.89 | 8.43 | 15.14 |
| **Si** | 97.71 | 45.46 | 22.56 | 31.03 |
| **P** | 0.70 | 3.96 | 7.79 | 6.68 |

Position **I** is located at the former inner part of a wire, which mainly consists of silicon. The positions **II - IV** exhibit high fractions of oxygen from immediate oxidation of lithium brought into contact with air, being reported in related publications[94]. Detected fluorine and phosphorus were assigned to originate from the applied Li-

containing salt $LiPF_6$[95] and carbon from polymeric electrolyte additives discussed in Chapter 3.6.3. Furthermore, gallium and platinum were detected being artefacts of the FIB-assisted preparation as described in Chapter 2.4.1. In order to avoid oxidation, the samples were handled and also prepared inside a glovebox and later transferred inside an argon-filled bag (see Chapter 2.4.3). Inside the glovebox the wires were scratched off the copper backside and further ground thoroughly to be put onto a TEM grid. Figure 3.17 b depicts a fragment of a ground crystalline wire surrounded by amorphous SEI particles documented by corresponding SAED patterns (see Figure 3.17 c, d).

### 3.6.1 De-/lithiation mechanisms

Initially, an anode consists of highly crystalline and ordered Si microwires. During lithiation, Li ions from the counter electrode are transferred through the electrolyte to the anode, where they are incorporated into the individual wires and form alloys (see Figure 3.18 a). The Li-containing electrolyte enters the Si wires and partially decomposes[82]. Within this project, a $LiPF_6$-based electrolyte was used as a Li-containing agent. In the positive electrode-electrolyte reaction, $Li^+$ and $PF_6^-$ form through decomposition of $LiPF_6$[83,89]. EDX elemental mapping (see Figure 3.18 b) of a silicon wire after 35 charge/discharge cycles demonstrates the presence of remaining fluorine and phosphorus in the grown SEI, which was not removed after cycling.

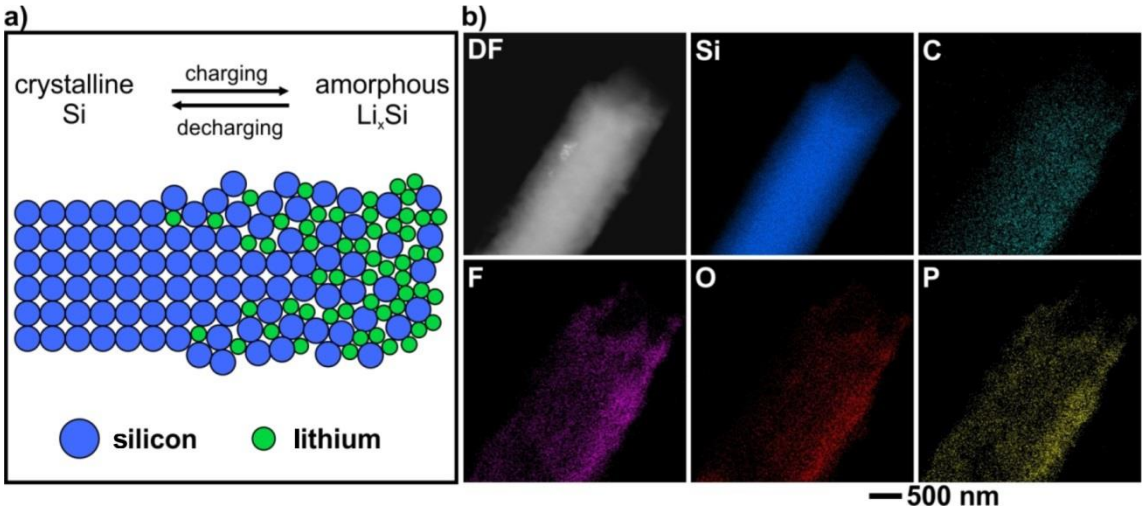


**Figure 3.18:** a) Schematic model of Li incorporation into crystalline silicon. b) HAADF-STEM image and EDX elemental maps of a cycled Si wire

At this point, it should be emphasized that a remaining SEI is wanted in order to investigate its properties and understand its influence on the electrodes' performance. During Li incorporation, different preferential amorphous Li-Si compounds are formed (see Table 2) accompanied by a volume increase up to a factor of four[64,96–99]. In the

delithiation reaction of the anode, Li-Si phases become oxidized as lithium gets extracted, and subsequently the wires' volume decreases. Essential for the long-time performance is the reversibility of these two mechanisms. Especially chemical and mechanical properties of the SEI are major factors and their decisive parameters will be discussed in the following chapters aiming to optimize set-up and treatment of the final anode.

### 3.6.2 Charging parameters

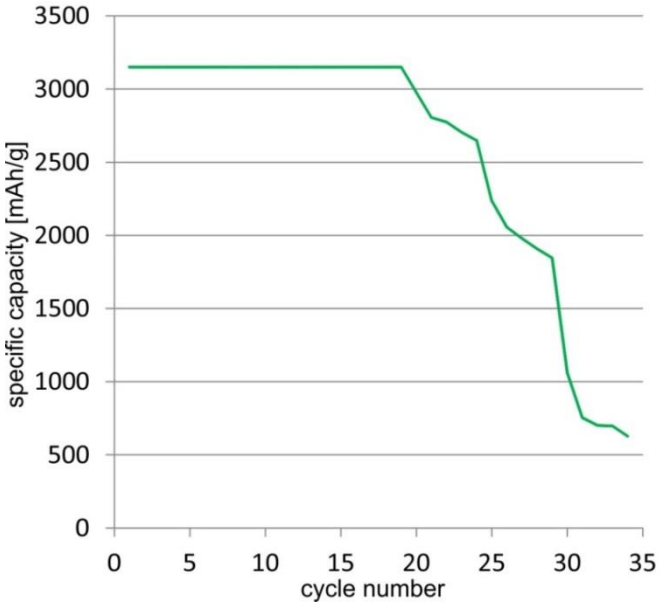


**Figure 3.19:** Capacity of an early sample with the standard electrolyte over the first 34 cycles.

Already after the first cycles, a severe impact of the charging set-up on the anode condition was noticed as the anode started to decompose from the surface. Electrochemical experiments carried out in parallel (see Figure 3.19) exhibit a large drop of the specific capacity after increasing the charging from C/2 to 1 C at cycle no. 20. This drop is attributed to a mechanical decomposition, more specifically, to the loss of anode material due to flaking off the surface. During SEI formation, high current densities due to higher charging rates occur that cause a sharper amorphization front and increase structural disintegration at the wires´ surfaces[89]. Furthermore, the generation of defects is expected to reduce the ion conductivity, and consequently the capacity by partial passivation of areas with a high defect concentration. To overcome degradation, and in addition increase the compatible charging speed, an effective protection is necessary, which encloses the Si wires, but is still permeable to the electrolyte. The first experiments focused on the influence of the cycling speed and numbers of cycles on the wires' structure as well as the SEI formation. Four different set-ups were tested: two with the anode cycled once and two with the anode cycled

five times. For both numbers of cycles one sample was cycled at a charging rate of C/2 and one at C/10, meaning two/ten hours for complete charging. The cycling as well as the electrochemical characterization was carried out by Dr. Hansen. After cycling, the anodes were disassembled in the glove box and prepared for TEM analysis.

Slower charging

After one cycle at the lower charging rate (C/10), the wires were overall intact being crystalline and without a remarkable change of their thickness and surface shape. But an inhomogeneous 5-40 nm-thin SEI was detected on top of the wires partially frayed surface (Figure 3.20 a). Near the surface, dislocations were observed (Figure 3.20 b) which arise from imperfect recrystallization during delithiation. From the HRTEM micrograph (Figure 3.20 b, inset) an exemplary dislocation line can be assigned to <111> and it is located between two crystalline domains separated by a systematic shift of ½ ½ ½. As simulated by Wang et al.[100], defects in crystalline silicon hinder ion diffusion. The dislocations, which remain after cycling of crystalline silicon, decrease the Li-ion movement, release and absorption. As a consequence, a local passivation and subsequently a decrease of the anode's capacity occurs. The scattered presence of defects and the varying thickness of the SEI indicate that the reaction of the electrolyte with the silicon anode proceeded incompletely.

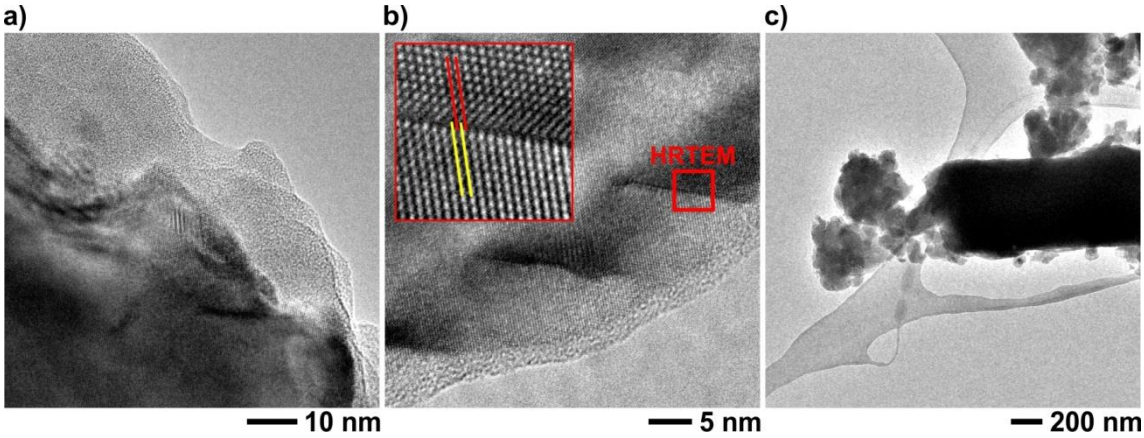


**Figure 3.20:** Silicon wire after one charge/discharge cycle at C/10: HRTEM micrographs of (a) the frayed silicon surface covered by an irregular thin SEI and (b) defects near the surface. The present shift between two domains is indicated in the inset by yellow and red lines. Silicon wire after five charge/discharge cycles at C/10: c) BF-TEM image of a degraded wire.

After five cycles, wires with reduced diameters of around 600 nm were identified (see Figure 3.20 c). Due to an incomplete discharge process, the amorphous outer parts of the silicon wires remain amorphous. Previous studies[101,102] by other groups showed that a volume decrease from delithiation induces tensile stress, which gets released by crack formation. Generated cracks end at the lithiation boundary and promote the

peeling off of amorphous parts at the surface. In case of the silicon wires, a peeling off during discharge or lastly during preparation is expected. A schematic model is depicted in Figure 3.21.

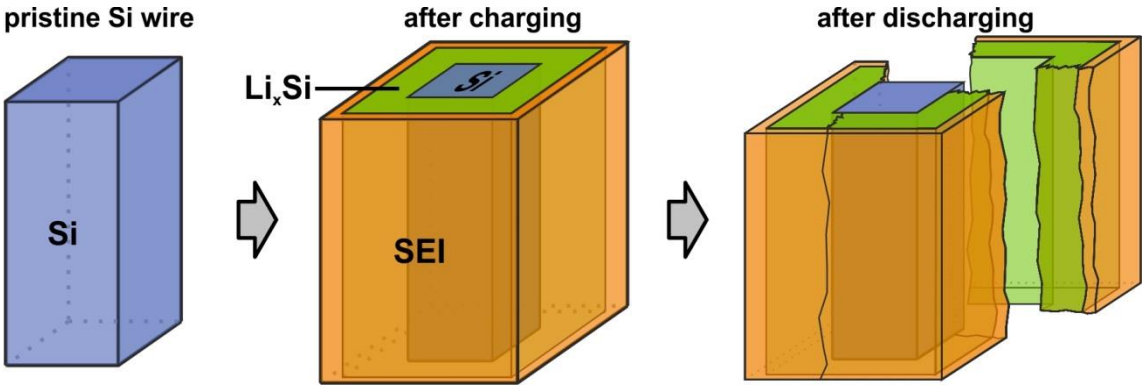


**Figure 3.21:** Degradation mechanism of a silicon wire during charging.

During charging, the electrolyte reacts with the pristine silicon wires. Lithium gets incorporated and Li-Si phases form at the surface accompanied by volume expansion and an aggregation of a surrounding SEI. Crack formation and propagation decreases the structural stability at the outer part and causes splintering of fragments. The wires' dimensions shrink after each cycle as long as crystalline silicon is present and high stresses occur. Finally, thin amorphous wires remain. Lee et al. stated that the critical thickness for further fracturing is approximately 300 nm[101].

Faster charging

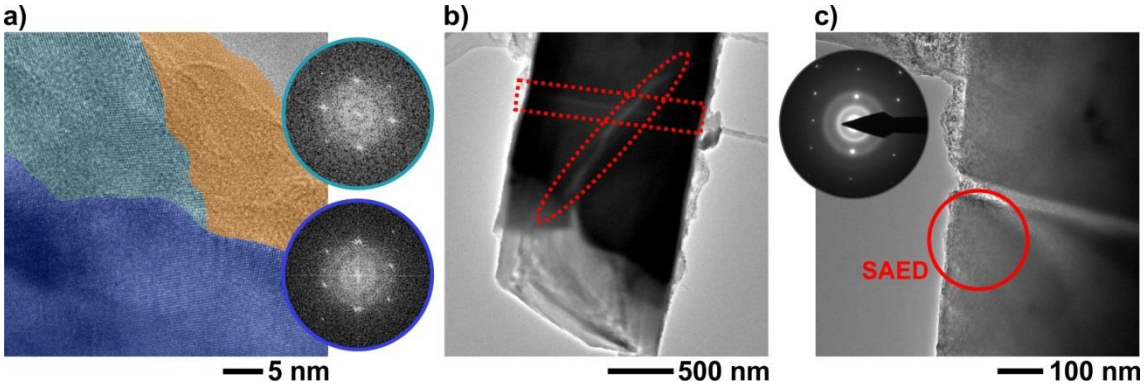


**Figure 3.22:** a) HRTEM micrograph of a Si fragment (light blue) attached to a wire's surface (dark blue) next to the amorphous SEI (orange). Insets show corresponding FFT patterns from the crystalline regions. b) BF-TEM image of a Si wire with cracks in red-dotted frames. c) Detailed BF-TEM image of a wire's surface at a crack with corresponding SAED pattern from the marked position.

Applying a higher charging rate of C/2 right from the first cycle on caused severe degradation. Disruption of (lithium-) silicon fragments occurred already after the first cycle. Figure 3.22 a shows a crystalline silicon particle attached to a wire's surface. A

plausible explanation might be that evolving stress in the outer parts cannot be compensated and gets released by cracking. Afterwards, the resulting particles get again attached to the surface. This observation supports a mechanism suggested by Iaboni et al. in which a fractioning of the outer shell is caused by a vast volume increase[103]. The sample cycled five times featured strong degradation effects. Deep cracks were identified as shown in Figure 3.22 b. A more detailed study (Figure 3.22 c) reveals the surrounding of a crack. The initially crystalline wire is covered by an amorphous surface represented by Debye-Scherrer rings[104] in the SAED pattern (Figure 3.22 c, inset).

### 3.6.3 Electrolyte dependence

For the fabrication of high-energy Li-ion batteries, the electrolyte is a crucial part as it determines the chemical environment of a battery. The aggregating SEI, which forms at the interface of the anode material and the electrolyte, is not totally understood, but proven to be very sensitive. Thus, many concepts to stabilize the emerging silicon-SEI compound were developed with the basic idea to fabricate a stabilizing shell, which supports enlargement and stresses in the forming compound[105–107]. For silicon microwires a related concept was followed aiming to modify the SEI by utilizing different electrolyte additives[89]. In general studies on electrolytes[79,93–95,108], the influence of common additives was investigated in terms of stability and long-term performance of the anode. For the first experiments the commercial carbonate-based electrolyte *Selectilyte LP 30* from *BASF* was used. It contains 1 M $LiPF_6$ in a 1:1 mixture of DMC and EC. In the following, selected additives were integrated to investigate the anode material after cycling.

#### Propylene carbonate

Chemically related to the basic electrolyte, propylene carbonate (PC) was added in two different amounts. Resulting compounds contained 5 (PC-5) and 50 wt.% PC (PC-50). The actual anodes were cycled 34 times with different charging rates. Based on the results of the previous experiments, a lower charging rate of C/10 was applied for the first four cycles to afford the formation of a stable SEI. The following ten cycles were carried out at C/2 and, eventually, 1 C was applied. TEM investigation of PC-5 revealed that the microwires were almost intact after 34 cycles. Figure 3.23 a depicts a study of an intact Si wire with a diameter of approximately 1.3 µm. The core of the wire was found to be crystalline, demonstrated by an exemplary SAED pattern obtained next to the surface which corresponds to silicon (compare Figure 3.16 b). Due to the rough wire surface and silicon-SEI interface, the SEI thickness can only be estimated, according to the positions of the crystalline SAED patterns closest to the surface, to

about 150 nm. A higher magnified detail of the SEI (Figure 3.23 b) points out its amorphous nature represented by blurred rings the SAED patterns (Figure 3.23 a, b).

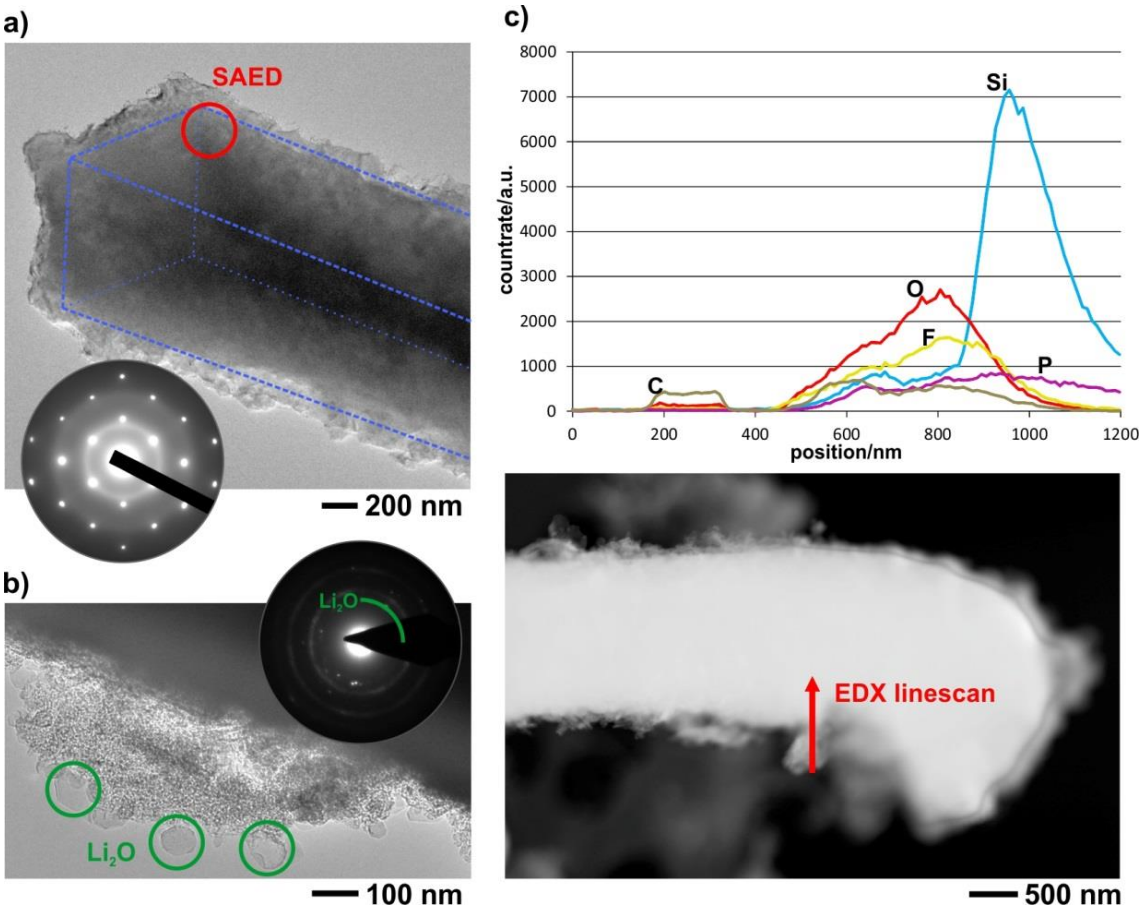


**Figure 3.23:** PC-50: a) BF-TEM image of an intact microwire with SAED pattern from marked region in the inset. b) Magnified detail of the SEI with marked $Li_2O$ crystals and a corresponding SAED pattern in the inset. c) EDX linescan (top) from the region marked in the STEM image (bottom) displaying the count rates for selected elements.

Remaining Li in the form of $Li_2O$ was identified. Marked by green circles in Figure 3.23 b, distinctive $Li_2O$ shells were found as well being marked in the corresponding SAED pattern. An EDX linescan was performed at the surface (Figure 3.23 c) in order to analyze the composition of the SEI. The corresponding diagram compares the count rates for identified elements. Being tilted around its longitudinal axis by 45° the projected thickness of the wire is low at the edges and increases to the center. Thus, the silicon signal increases from edge to center at first, but drops with increasing thickness due to absorption. Next to the increasing silicon signal, elevated oxygen and fluorine levels were recorded. Oxygen originates from $Li_2O$ and fluorine from the Li-containing salt of the electrolyte. Furthermore, phosphorous, as well originating from the salt, and carbon, presumably from the PC, were detected. During cycling, the

capacity for PC-5 was measured remaining remarkably stable at a high level (see Figure 3.24). With a higher PC content the PC-50 wires look similar to PC-5 without significant changes in microstructure or thickness and shape of the SEI. But their capacity decreases significantly during cycling, and is eventually much lower than that of PC-5, which is explained by the formation of a thicker SEI.

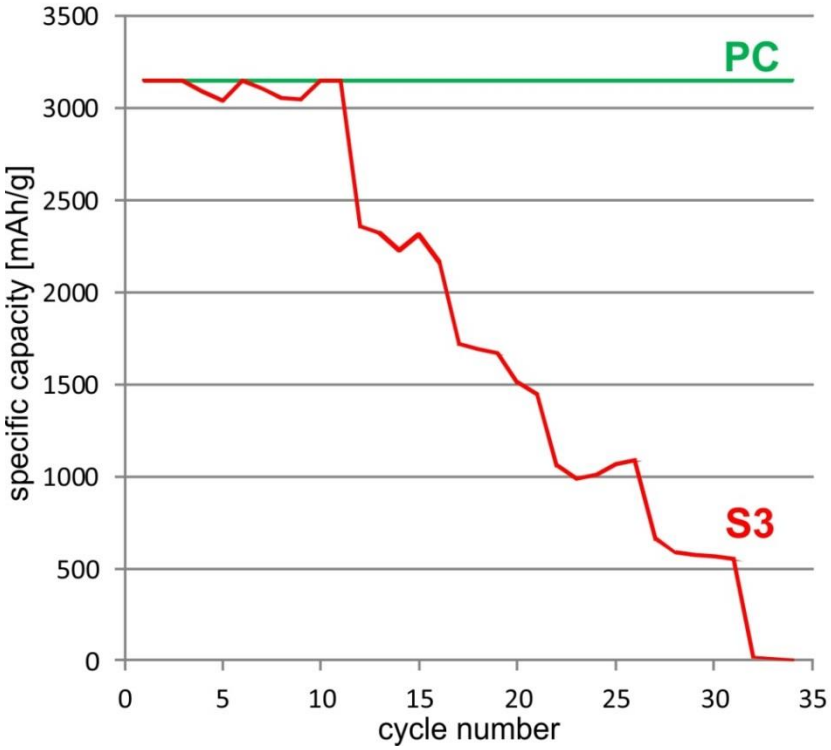


**Figure 3.24:** Comparison of capacities for the first 34 cycles for the samples PC-5 (green) and S3 (red).

S3

The ternary polymer blend S3 consists of lithium bis(trifluoromethanesulfonyl)imide (LiTFSi), dimethyl ether (DME) and 1,3-dioxolane (DIOX) and a similar composition was already reported to work well for another type of lithium-sulfur battery[109]. The cyclic performance was worse compared to former electrolytes. By increasing the charging rate from C/10 to C/5 after 11 cycles, strong capacity fading for the following cycles was recognized (see Figure 3.24). The reason is assumed to be a change in the silicon microstructure upon cycling. TEM analysis revealed that the Si wires became polycrystalline with scattered remaining crystalline domains (see Figure 3.25 a). The detailed HRTEM micrograph (Figure 3.25 b) depicts a single domain with a measured plane distance of 0.31 nm, characteristic for Si. Furthermore, no SEI was observed indicating its instability and coincides with the wire's diameter which decreased to about 830 nm. Even entirely amorphous wires with a thickness of only 340 nm were identified (see Figure 3.25 c). By performing EDX linescans (see Figure 3.25 d), high

oxygen and fluorine concentrations were detected even at the wire's core. Oxygen originates from LiTFSi which decomposes and $SiO_2$ forms. For fluorine an incorporation in form of LiF[110] during charging is assumed, which partially remains inside the wire due to a low conductivity and suppresses recrystallization. Through the impact of fluorine and oxygen, the Si wires subsequently get amorphous and passivated.

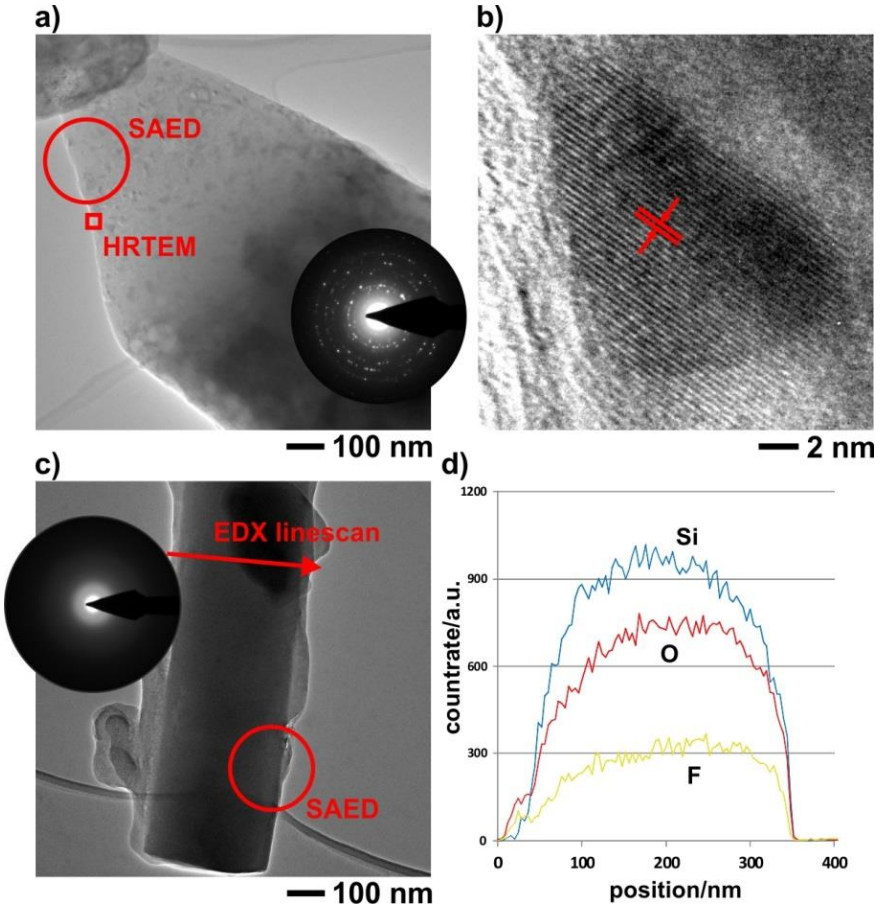


**Figure 3.25:** a) BF-TEM image of a Si-wire fragment with marked positions from the SAED pattern (in inset). b) HRTEM micrograph of a crystalline Si particle from position marked in (a). Two adjacent lattice planes are marked by red lines and arrows. c) BF-TEM image from a thin amorphous Si wire and SAED pattern from circled position in the inset. d) EDX linescan data from position marked in (c).

### Elevated temperature

As results at room temperature (with PC as additive) were very promising, a further parameter, namely the temperature, was changed. Elevated temperatures were reported to be very harmful for batteries since enhanced self-discharge occurs, which finally leads to complete failure of the battery[111,112]. To simulate operation conditions the battery set-up was heated in a steel housing to 65 °C. The first sample contained the standard electrolyte *Selectilyte LP 30*. The charging rate for cycling at elevated temperature was kept at C/10 for the first ten cycles and C/2 for the following cycles.

After 35 cycles, the sample exhibits noticeable changes of microstructure and performance. The silicon core features multiple cracks (see Figure 3.26 a) but the resulting fragments still are monocrystalline. The SAED image observed at a region next to a crack bears the monocrystalline pattern from one big fragment and additional rings presumably as residues from smaller fragments due to cracking. A drop of the capacity directly after the increase of the charging rate was detected (see Figure 3.26 b), which is explained by a decrease of electron and ion conductivity caused by those cracks. The elemental maps (Figure 3.26 a) display elevated concentrations of O, F, P and C not only at the wire's surface, as observed for PC-5, but also at the interfaces, generated by the cracks. The fragments are chemically isolated from each other by an expanded internal SEI. The thickness of the SEI at the surface is still comparable to the one from PC-5.

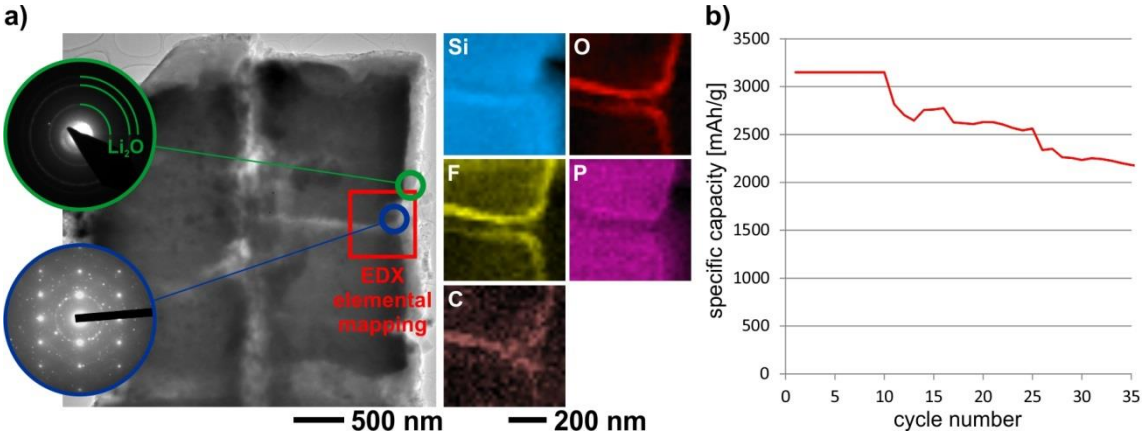


**Figure 3.26:** a) BF-TEM image of two neighboring microwire fragments after cycling at elevated temperature with SAED patterns from two selected positions and EDX elemental maps at an internal crack. b) Capacity of a sample with the standard electrolyte for the first 35 cycles at elevated temperature.

Boron nitride

Recent publications reported higher ion conductivity and temperature stability by using BN additions in Li-ion battery electrolytes[113,114]. Thus, within this work, it was also tested for compatibility in Si-microwire batteries. Before cycling, the Si-wire tips were coated with BN nanoplatelets through reduced pressure-assisted infiltration of a 1 wt.% BN-containing aqueous dispersion. Depicted in Figure 3.27 a, the wires were cycled without remarkable decomposition after 35 cycles. The STEM image depicts a 2.2 µm-thick wire and EDX elemental mapping reveals an intact silicon core region with a diameter of roughly 1.0 µm, which corresponds to the initial wire's diameter. Furthermore, a homogeneous distribution of F and P, originating from the electrolyte, was measured. Through SAED, the presence of LiF, assumed to originate from a decomposition of $LiPF_6$, was detected. Due to the characteristics of the EDX detector, a

detection of boron is not technically possible. Further experiments by Dr. Hansen demonstrated that the coated wires' stability was maintained at higher temperature of 80 °C[89], whereas wires without BN coating failed (compare Figure 3.27 b). The drop for the BN-treated sample at cycle 9 and 10 was caused by a short drop out of the measurement set-up.

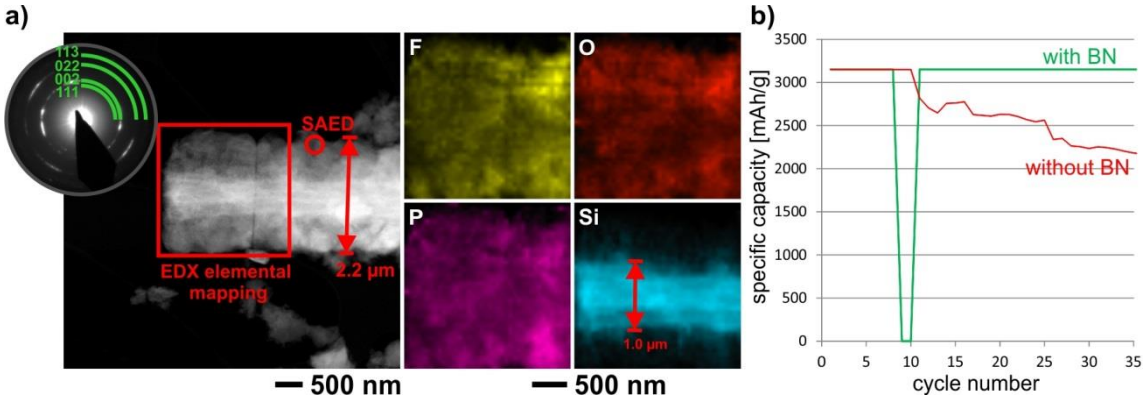


**Figure 3.27:** a) HAADF-STEM overview image of a BN-treated Si wire with EDX elemental maps and SAED pattern from the marked areas. The circular arcs correspond to LiF. The red arrows specify the thicknesses of the whole wire and the enclosed silicon core. b) Capacities of a BN-coated sample for the first 35 cycles at elevated temperature (green) and for comparison the sample without BN (red).

## 3.7 Summary

Bearing a sensitive cycling behavior, the examination of ideal fabrication and working conditions for Si microwires is very challenging. Their size and aspect ratio turned out to be detrimental for TEM preparation and analysis, the air sensitivity of lithiated samples is especially crucial. Non-battery Li-Si experiments including HRTEM and PED were carried out to probe the characteristics of common $Li_xSi$ phases for an easier identification and handling during the battery-related experiments. Preparation procedures applying FIB-milling and microtomy were developed as well, which finally render TEM-focused examination of microstructure and composition of micro-sized wires possible.

The negative influence of high charge/discharge current on the stability of the wires was identified. Elucidated by HRTEM data and elemental mappings, the formation of a stable SEI in the first cycles is found to be essential to avoid decomposition and passivation of the anode material and to enable high charging rates. An effective measure is the tuning of the electrolyte. The most promising electrolyte configuration is a DMC/EC mixture with a 5 wt.% addition of PC. Applying this configuration, a reversible cycling of the anode is realized without remarkable loss of capacity. Furthermore, an initial coating of Si wires with BN improves the cycling stability,

especially at elevated temperatures. A slightly elastic and stabilizing SEI is also understood to be of great importance, supporting expansion and compression and absorbing evolving stresses during cycling; otherwise cracks form and promote degradation and passivation of the anode material.

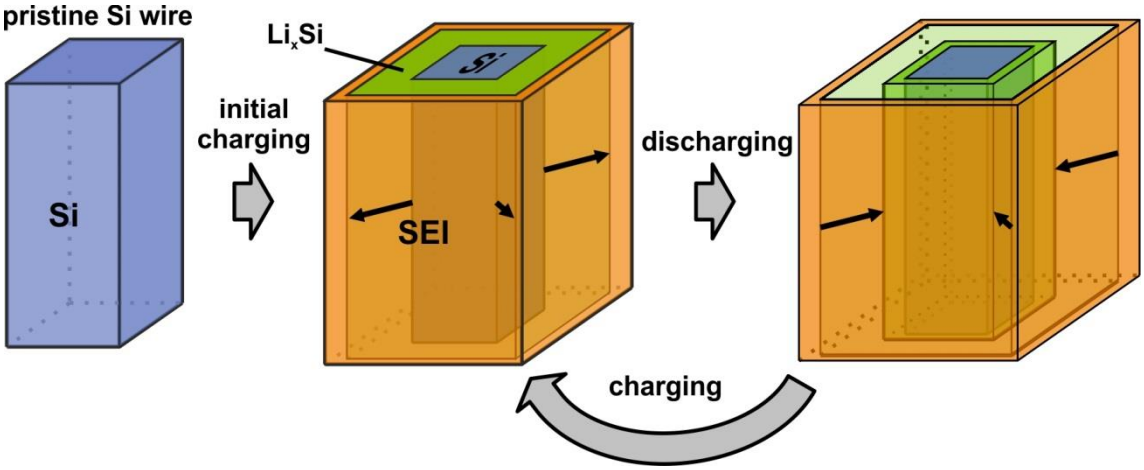


**Figure 3.28:** Schematic ideal reversible charge/discharge cycle for Si microwires.

The idealized case is depicted in Figure 3.28. The pristine Si wires get charged and absorb Li to form $Li_xSi$ phases surrounded by an evolving SEI. During discharge, $Li_xSi$ phases decompose, Li ions leave the wire and Si remains, which recrystallizes to reduce its entropy.

# 4 Amorphous silicon

A different approach to exploit the vast potential of silicon-based anodes for secondary cells is the application of amorphous silicon (*a*-Si). Unlike its crystalline analog, *a*-Si cannot suffer from structural degradation since it has no long-range order. Common synthesis procedures are thin-film deposition[115,116] and core-shell fabrication by deposition of particles with silicon[117,118]. The theoretical capacity of amorphous silicon was determined to be equal[98] to that of crystalline silicon. By fabricating a porous material, internal stresses are minimized in order to reduce degradation and capacity fading.

In the first part of this chapter two recently synthesized forms of amorphous silicon[68] obtained by chemical extraction from a Li-Si and a Na-Li-Si compound are compared. Assisted by TEM investigations, their structure and stability is analyzed, especially the influence of elevated temperature. In a continuative experiment, germanium was incorporated to obtain an amorphous $Si_{1-x}Ge_x$ compound. Applying the resulting compound in an anode, the potential advantage of the high conductivity of germanium[119] is examined. Materials presented herein were fabricated by Dr. Michael Zeilinger at the Department for Chemistry at TU Munich and characterized at the Institute for Material Science at Kiel University. It has to be considered that Li could not be detected by EDX experiments. Thus, specified elemental concentrations exclude Li.

The second part highlights hollow silicon structures recently developed by Dr. Iris Hölken at the Institute for Material Science at Kiel University. In a sacrificial template synthesis, hollow silicon nano- and microstructures were fabricated being supposable materials for new types of Li-ion batteries since they offer more degrees of freedom for expansion and compression during charging/discharging.

## 4.1 Amorphous silicon/-germanium

### 4.1.1 *a*-Si

Instead of forming amorphous silicon layers by deposition techniques, a silicon-containing compound can be dissolved softly so that pure silicon remains in form of amorphous nanoparticles (Figure 4.1). Starting with $Li_{15}Si_4$ (see Figure 3.3), lithium was extracted by liquid ammonia[68] and left a black air- and moisture-sensitive powder after drying.

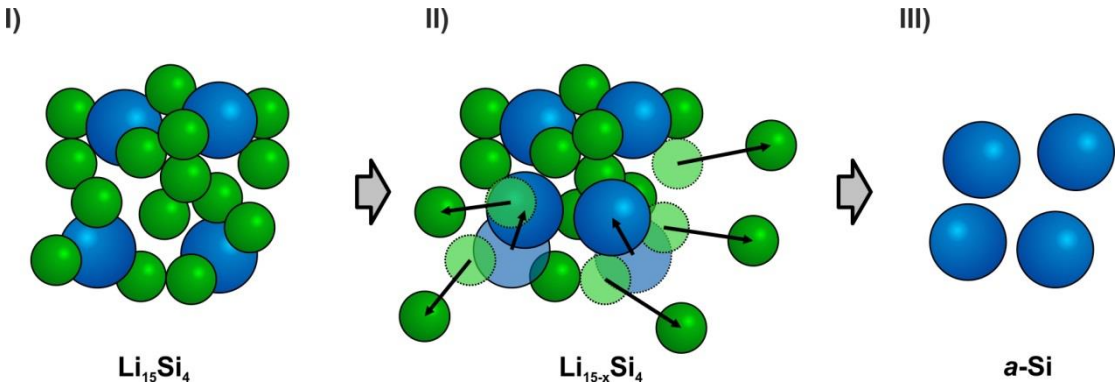


**Figure 4.1:** Schematic synthesis of amorphous silicon (III) by extraction of lithium (II) from $Li_{15}Si_4$ (I).

In first EDX experiments on *a*-Si oxygen levels up to 70 at.% were detected depicting strong local oxidation. The oxygen concentration, being even higher than 66.7 at.% in case of pure $SiO_2$, is assumed to originate from $Li_2O$ formed from remaining lithium which as well got oxidized, but cannot be detected by EDX. In order to avoid strong oxidation, the powder samples were handled inside a glovebox and transferred inside an Ar-filled bag as described in Chapter 2.4.3. Subsequently, the oxygen level was reduced to about 10 at.%. Generally, agglomerations of nanoparticles were identified which showed higher oxygen concentrations at the edges, being typical for surface oxidation[92]. In the core regions oxygen levels of about 5 at.% were detected whereas in the surface regions they showed up to 30 at.% O. In Figure 4.2 b a typical framework of amorphous silicon is displayed, which consists of elongated particles with diameters below 20 nm. The corresponding SAED pattern in the inset contains rings of diffuse intensity with d-values of 0.312 nm and 0.174 nm. The first (inner) ring corresponds to the (111) d-value of cubic silicon[59]. The second (outer) ring has a diffuse outline and contains virtually two rings: Corresponding to d-values of 0.192 nm [Si – (220)] and 0.164 nm [Si – (311)], those are emphasized in darker blue. Due to a non-existent long-range order, there are no sharp distinctions concerning bond length and distance of neighboring atoms. Changing to high magnification, crystalline domains with diameters of 5-10 nm could be determined as depicted in Figure 4.2 c. An FFT pattern for such a nanoparticle gave two spots from apparent lattice planes which correspond to (002) for cubic silicon. Aside from small scattered crystalline domains, it can be concluded that the extraction process to produce amorphous silicon worked out well.

A stronger oxidized region is displayed in Figure 4.2 a. Compared to the previous one it appears more porous with less entangled particles, but with similar diameter of below 20 nm. The presence of remaining Li or $Li_2O$, respectively, is expected to influence the structure of Si after extraction. The corresponding SAED pattern (Figure 4.2 a, inset) features amorphous rings with diameters complying with reciprocal distances of about 0.271 nm and 0.148 nm being reported for a different Si type with space-group $Ia\bar{3}$[120].

Li et al. reported that delithiation of $Li_xSi$ compounds usually occurs incompletely[121]. Amorphous silicon contains many dangling bonds[122,123] due to the presence of a high surface area and many lattice mismatches. Those dangling bonds likely get saturated by trapping remaining lithium, which is subsequently pinned and unable to leave the compound during delithiation.

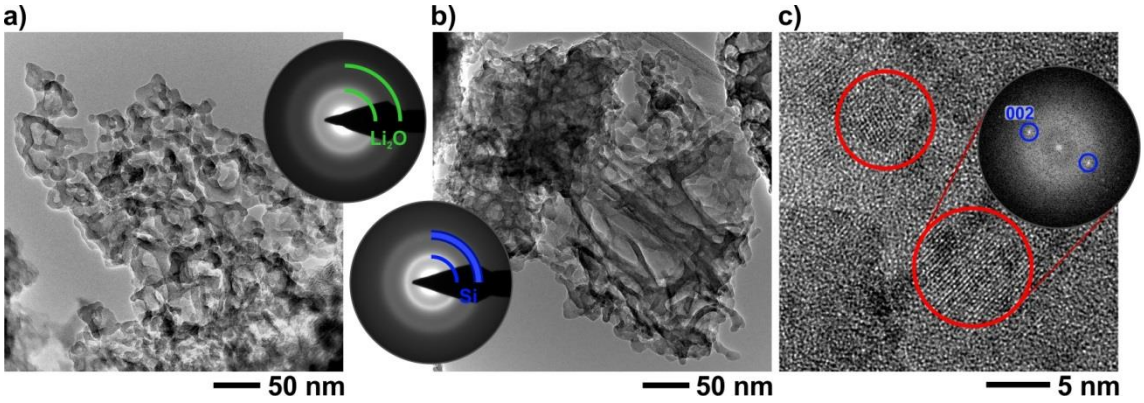


**Figure 4.2:** TEM study of different morphologies in *a*-Si with corresponding SAED patterns in insets. a) Highly porous structure with elevated oxygen content. b) Less porous structure from region with lower oxygen content. c) HRTEM micrograph from nanocrystalline Si domains in amorphous Si.

*In situ* heating

By applying differential thermal analysis (DTA), Zeilinger et al. determined a phase transition from amorphous to crystalline at 658 °C, which is far above practically relevant temperatures a battery is ever exposed to. So, a phase transition due to heat was excluded. For the present *a*-Si, *in situ* heating was performed with parallel imaging by BF-TEM and SAED to examine occurring changes of morphology and microstructure. Starting from room temperature, the sample was heated in 50 °C steps at a rate of 6 °C/min to eventually 700 °C. During heating, particle coalescence started at 150 °C and the porosity decreased. A surface-near region is studied at T = RT and T = 650 °C (Figure 4.3). Especially at the surface an increase in particle size upon heating was recognized. An evaluation of the corresponding SAED patterns offers changes concerning the crystallinity. The peak-to-background ratio was determined for the most intense three inner rings. Figure 4.3 c maps the angular intensity of the ring for the biggest d-value (I) at T = RT and T = 650 °C. From 60° to 115°, the signal was blocked by the beam stopper. The corresponding profiles do not show noticeable differences, thus, it can be ruled out that the degree of crystallinity changed during heating. Different from the DTA experiments, a transition to crystalline Si was not observed. A presumable reason is insufficient heating of particles due to a weak contact to the TEM grid.

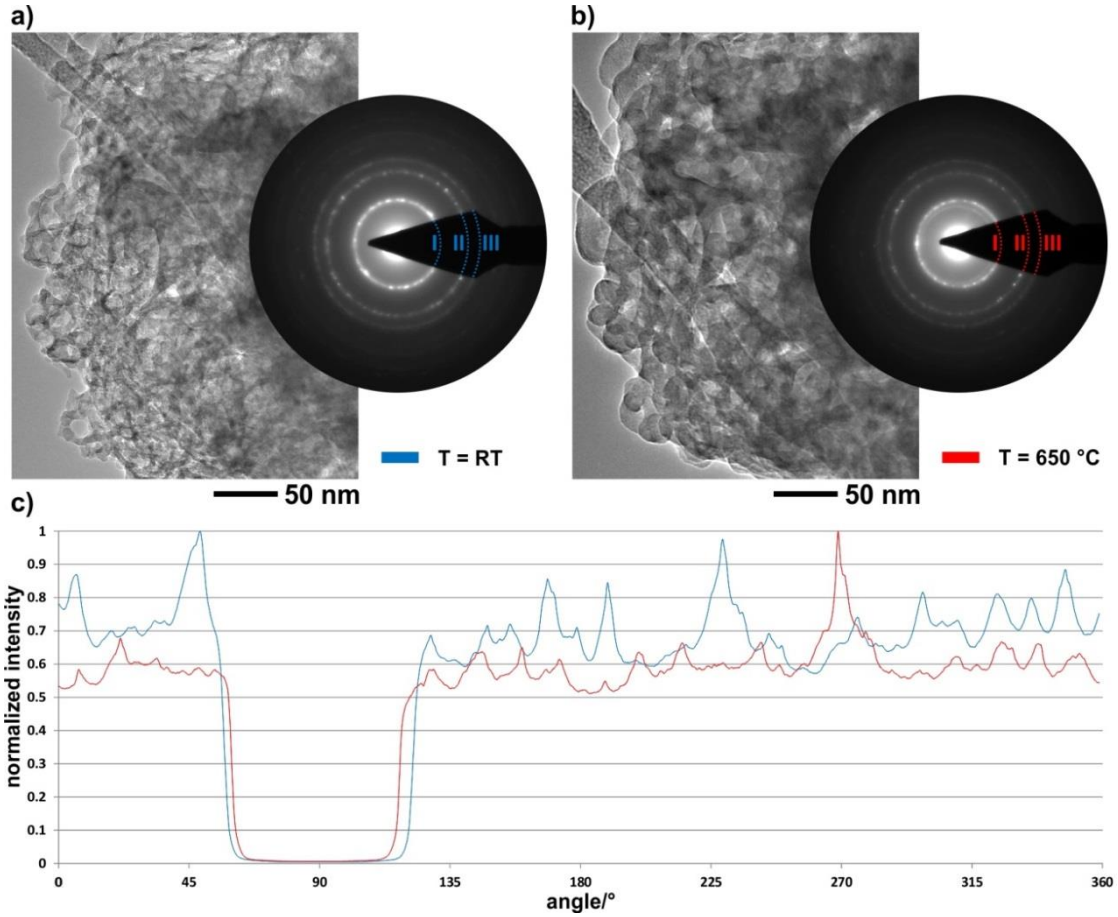


**Figure 4.3:** BF-TEM images and corresponding SAED patterns of *a*-Si at (a) T = RT and (b) T = 650 °C. c) Angle-intensity plot for inner diffraction rings (I) from the SAED patterns of (a) and (b).

### 4.1.2 *a-allo*-Si

After successful synthesis of amorphous silicon from $Li_{15}Si_4$, the sodium-containing silicon compound $Li_3NaSi_6$ was selected to perform an extraction in order to obtain a different modification. Here, after extraction of Li, remaining polyanionic silicon layers were expected to topotactically convert to an allotrope of amorphous silicon (*a-allo*-Si) through oxidation. In former works[124,125], a germanium allotrope was synthesized from $Li_7Ge_{12}$, which is structurally related to $Li_3NaSi_6$. Both contain homoatomic, consisting of only one atom species, layers (Ge/Si) including pentagons which form channels. Those channels provide, for instance, the absorption and conduction of Li ions, which might be useful for battery technology. In case of $Li_7Ge_{12}$, the crystalline morphology could be preserved after extraction of Li[126] and a similar approach was consequently performed for $Li_3NaSi_6$. By using water as a solvent, a nearly complete conversion was reported already[124]. A reproduction of this result was focused on by applying a treatment with ethanol followed by HCl[68]. Similar to the procedure for *a*-Si, the samples were transferred inside an Ar-filled bag to minimize oxidation. The oxygen

content was approximately defined to 10 at.% in average and a maximum of 15 at.% at the edges. Its particle size was remarkably bigger than for *a*-Si. Figure 4.4 a presents agglomerations of particles with minimum sizes of 50 nm. Respective diffuse amorphous rings in the SAED pattern were assigned to $Li_2O$ indicating an incomplete conversion from $Li_3NaSi_6$ to *a*-Si. Through EDX analysis, remaining sodium was also detected. SAED and HRTEM reveal the presence of nanocrystalline Si domains, three of which are marked in Figure 4.4 b. The presented FFT pattern contains two pairs of reflections, which were assigned to cubic silicon. The domains' sizes were determined to 10-20 nm in diameter, double the size compared to the former *a*-Si indicating the metastable state of *a-allo*-Si. Still, an *ab initio* differentiation of *a*-Si and *a-allo*-Si from imaging was not possible. But through powder XRD investigations performed by Zeilinger et al.[68], a qualitative differentiation was possible since the peaks in the pair distribution function for *a-allo*-Si correspond to crystalline Si, whereas an allocation of the peaks for *a*-Si was not explicit.

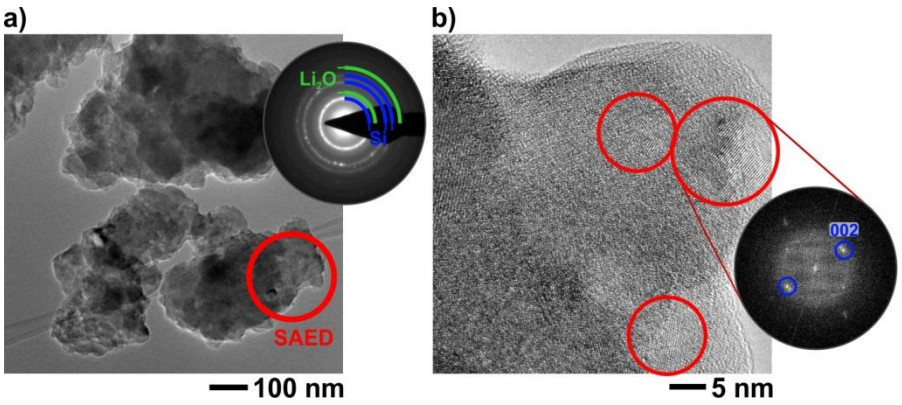


**Figure 4.4:** a) BF-TEM image of *a-allo*-Si with SAED pattern from circled position in the inset. b) HRTEM micrograph from nanocrystalline Si domains near a particle's edge with calculated FFT pattern from circled region.

*In situ* heating

Different from *a*-Si, the *a-allo*-Si was reported to exist as a metastable phase which irreversibly transforms to *a*-Si at 515 °C[124]. The transition temperature from amorphous to crystalline was determined by DTA to 565 °C[68]. An *in situ* heating experiment was performed starting from room temperature with a ramping of 6 °C/min and 50 °C steps ending up at 700 °C. Here, coalescence already started below 100 °C without remarkable change during further heating (compare Figure 4.5 a, b). The corresponding SAED patterns appear similar; both contain rings, emerging from present nanocrystalline silicon domains. The angular intensity profiles for the inner rings (I) do not differ in their peak-to-background ratio or the number of peaks. Here as well, the beam stopper blocked the signal between 60° and 115°. Although the

sample was heated to about 135 °C beyond the expected transition point, no transition was observed. Aside from unwanted deviation during heating, which possibly occurred in case of *a*-Si, a transition from *a-allo*-Si to *a*-Si is assumed since their morphologies after heating appear quite similar. In a continuative experiment, *a-allo*-Si was investigated with focus on minimal beam impact. Hence, the sample was treated by the focused electron beam for about 2 minutes. Before and after treatment, measurements were performed with reduced beam intensity and inserted aperture.

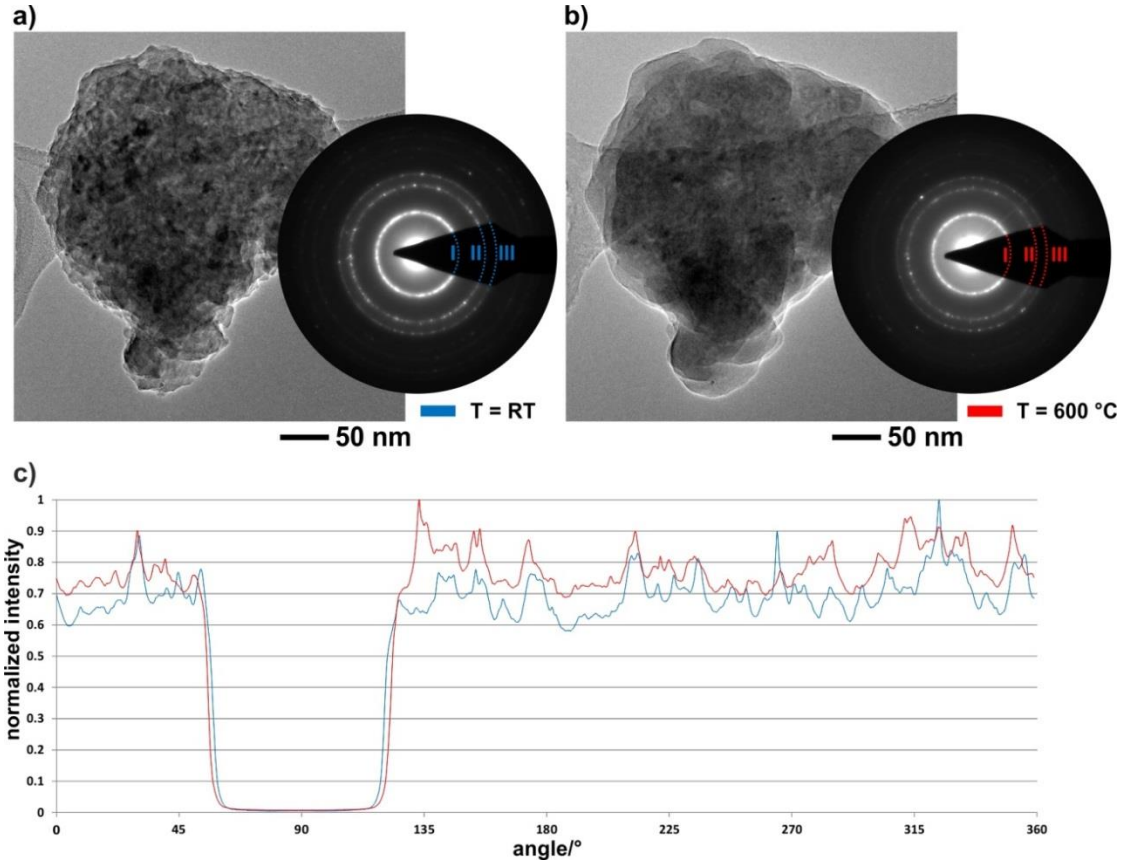


**Figure 4.5:** BF-TEM images and corresponding SAED patterns of *a-allo*-Si at (a) T = RT and (b) T = 600 °C. c) Angle-intensity plot for inner diffraction rings (I) from the SAED patterns of (a) and (b).

The morphology before the treatment (Figure 4.6) looks different than it does afterwards. Temperature-induced coalescence proceeded and the surface of the initially grainy particles became very smooth. In the corresponding SAED patterns, amorphous blurred rings present at room temperature transform to quite sharp rings with distinct spots as a result from beam-induced crystallization. By EDX analysis, the fraction of oxygen was determined to 8.5 at.% without a change, whereas the sodium signal reduced from 9.0 to 1.0 at.%. A similar effect was reported for sodium-containing glasses, where sodium got ionized by the electron beam and further moved away due to an electron-imposed electric field gradient[127]. In initial *a-allo*-Si, remaining

$Na_8Si_{46}$ impurities were detected by Zeilinger et al., which were subsequently oxidized to pure silicon, likely forming crystalline domains in case of small particles to reduce its surface energy[128].

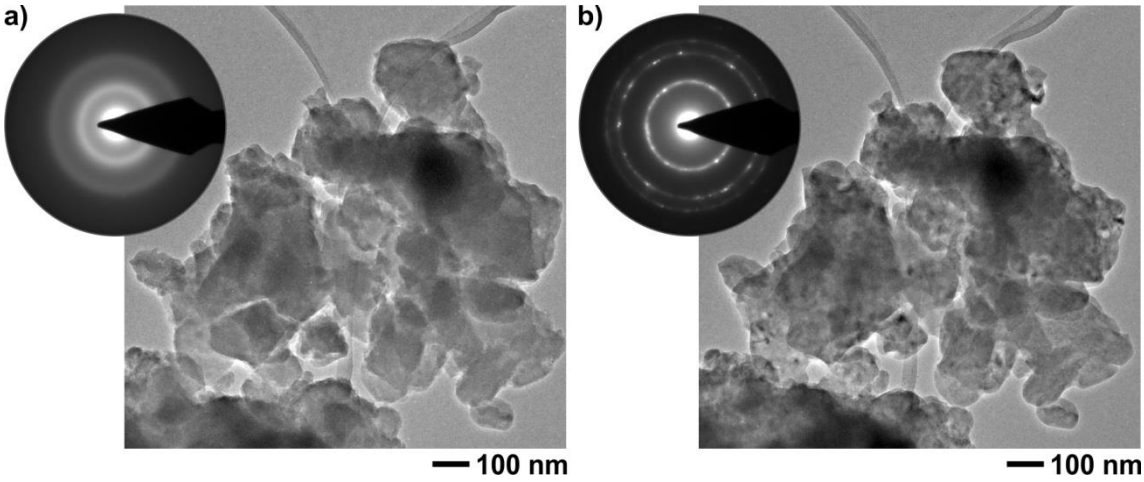


**Figure 4.6:** BF-TEM image and corresponding SAED pattern of *a-allo*-Si (a) before and (b) after extended beam treatment.

### 4.1.3 *a-allo*-SiGe

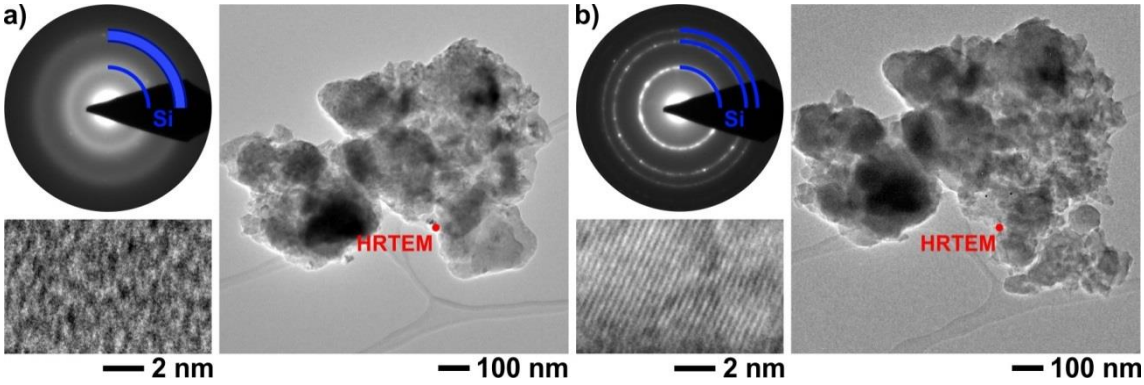


**Figure 4.7:** BF-TEM image with corresponding SAED pattern and HRTEM micrograph from marked position (a) before and (b) after extended beam treatment.

As for the synthesis of *a-allo*-Si, $Li_3NaSi_6$ was applied with Si being partially substituted by Ge. After extraction of Na and Li, a morphology similar to that of the pure-Si pendant was observed, consisting of agglomerated nanoparticles with sizes around 20 nm (see Figure 4.7). The Si:Ge ratio was determined by EDX analysis to 93:7. Ge and Si share a common structure type and are partially miscible according to Dismukes et al.[129]. For low Ge levels (e.g. 7 at.%) the change of lattice parameters amounts only 0.3 % and is hardly detectable, e.g. by SAED patterns. But SAED revealed that the Si-Ge compound transformed from amorphous to crystalline upon beam irradiation (compare Figure 4.7 a, b), and the respective HRTEM micrograph in Figure 4.7 b

depicts the present Si lattice planes. The distribution of germanium was further investigated by STEM. Since Ge has a higher atomic number than Si – 32 compared to 14 –, it effects electron scattering more strongly and causes stronger intensities in DF-mode. Inhomogeneous concentration levels for Ge were examined by an EDX linescan (see Figure 4.8) performed at a region with inhomogeneous STEM signal intensity. In the brighter region, a Ge ratio of 9-11 at.% was observed.

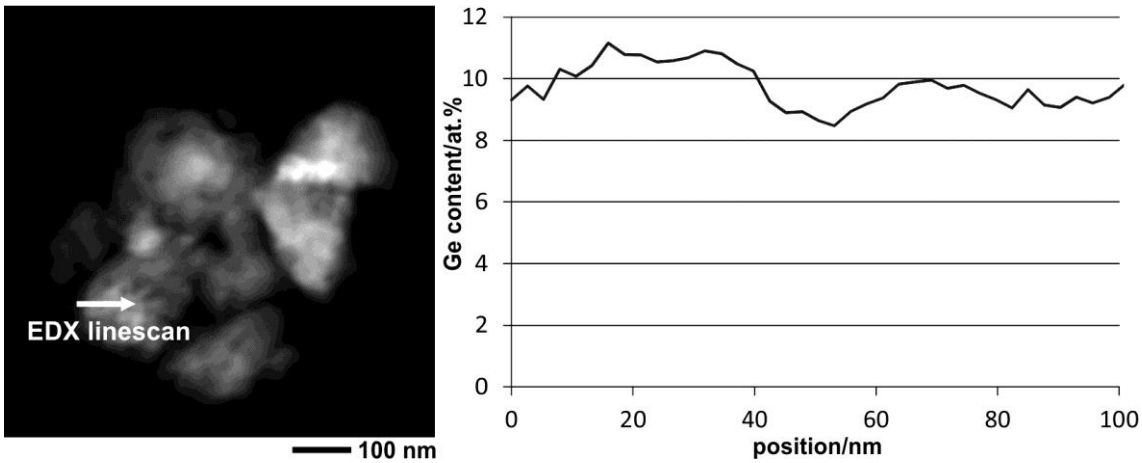


**Figure 4.8:** HAADF-STEM image of *a-allo*-SiGe. The profile recorded from the marked region depicts the stoichiometric ratio of Ge in relation to the sum of Ge and Si.

### 4.1.4 Electrochemical characteristics

With their high porosity the herein regarded amorphous silicon types were expected to provide large intercalation capacities for charge carriers, e.g. Li ions. Thus, *a-allo*-Si and *a-allo*-SiGe powders were tested as anode material for rechargeable batteries. Both types were equipped with a copper current collector to increase their conductivity. The initial charging capacity for *a-allo*-Si was measured to 3200 $mAhg^{-1}$ (see Figure 4.9, left), which is similar to the microwire type. In the following, the first discharge capacity, representing the practically available capacity, constituted 1300 $mAhg^{-1}$ which is only 40 % of the previous value. After 10 cycles the charging rate was increased from C/20 to C/10 and the capacity decreased to 400 $mAhg^{-1}$ after 20 cycles. At this point, the rate was increased to C/2 at a stable capacity to end up at 300 $mAhg^{-1}$ after 100 cycles. Besides, the conductivity was determined to be poor since the open circuit voltage was only 300 mV (for comparison: 2.8-4.2 V for Li-ion batteries[3]). Like silicon, germanium belongs to the class of semiconductors, but it offers a much higher (about a factor $10^4$, T = RT, undoped) electrical conductivity than silicon does, and is expected to diminish the low conductivity. Herein obtained experimental results (provided by Dr. Hansen) for *a-allo*-SiGe anodes state that the anodes suffered from large capacity losses although the conductivity was increased due to the presence of germanium. The starting capacity was 1600 $mAhg^{-1}$ and after

10 cycles only 900 $mAhg^{-1}$ remained (see Figure 4.9, right). After doubling the charging rate to C/10, the capacity dropped to 500 $mAhg^{-1}$. Due to a poor cycling performance, the integration of germanium was not developed any further focusing on more promising compounds.

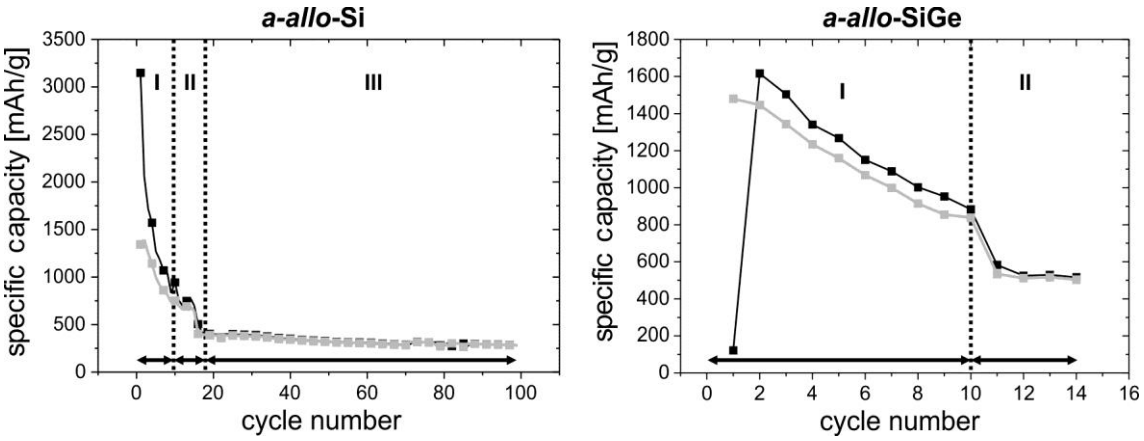


**Figure 4.9:** Comparison of the specific capacities during the first cycles for *a-allo*-Si (left) and *a-allo*-SiGe (right). The black curves refer to the charging capacities, the grey curves to the discharge capacities. The actual charging rates were C/20 (regions **I**), C/10 (regions **II**) and C/2 (region **III**).

## 4.2 Aero-silicon

By applying a sacrificial template synthesis, innovative silicon structures were obtained by Hölken et al. at the Institute for Material Science at Kiel University[130]. Basically, two different kinds of template shapes were utilized: tetrapodal and spherical ZnO. ZnO tetrapods were first reported and investigated more than 70 years ago[131]. Recently in Kiel, by flame transport synthesis[132], tetrapodal ZnO with hexagonal symmetry and a wide variety of sizes in the µm range was synthesized. Spherical ZnO features hollow sphere-shaped shells of ZnO. It was purchased from Sigma-Aldrich (Westerhausen, Germany).

The actual type of ZnO particles was covered by silicon via applying a silane flow in a plasma-enhanced physical vapor deposition (PECVD) process. Afterwards ZnO was etched away with a hydrochloric acid solution and hollow spherical- (S-Si) and tetrapodal-shaped silicon particles (T-Si) remained.

### 4.2.1 Spherical silicon

After etching, agglomerations of spherical particles with sizes between 0.2 and 1.0 µm were observed. Mainly closed, bubble-like particles were present which were nanocrystalline (see Figure 4.10 a), but also scattered open (flat) fragments, which were overall amorphous (Figure 4.10 b) with scattered small crystalline domains,

remained. Since the particles were coated by PECVD, the directed flow of the plasma created an inhomogeneous coating profile with strong variation of the thickness between 15 and 200 nm depicted in Figure 4.10 c.

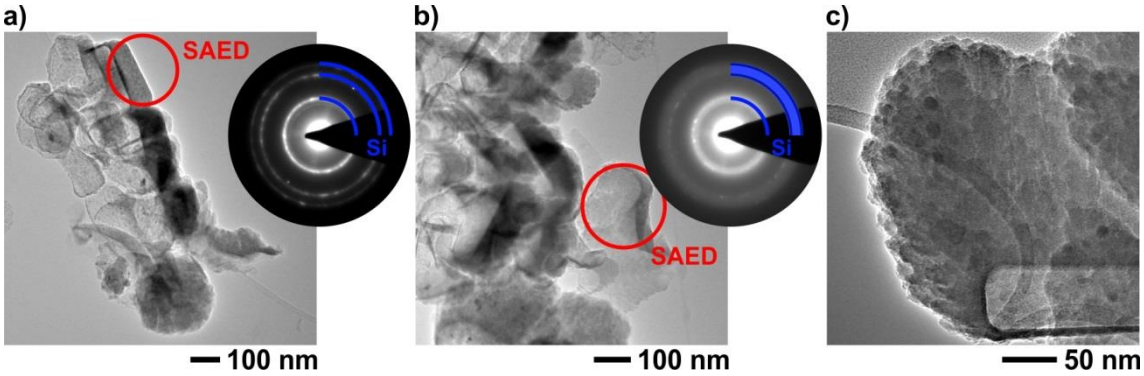


**Figure 4.10:** BF-TEM images of spherical-shaped silicon particles. a) Particle with nanocrystalline wall with corresponding SAED pattern from circled position. b) Presence of overall amorphous particles with corresponding SAED pattern from circled position. c) Detailed study of a particle surface.

Also, the nucleation process of silicon on zinc oxide was expected to promote selective growth. At higher magnification a puff-like structure was identified and columnar growth[133] was observed with increasing wall thickness. By EDX analysis, efficient etching was confirmed since no remaining ZnO was detected, but an oxygen concentration of about 10 at.% was determined. In fact, ED and HRTEM measurements (not shown) did not indicate any $SiO_2$. Thus, the O content was assigned to $SiO_x$ present as amorphous surface contamination.

### 4.2.2 Tetrapodal silicon

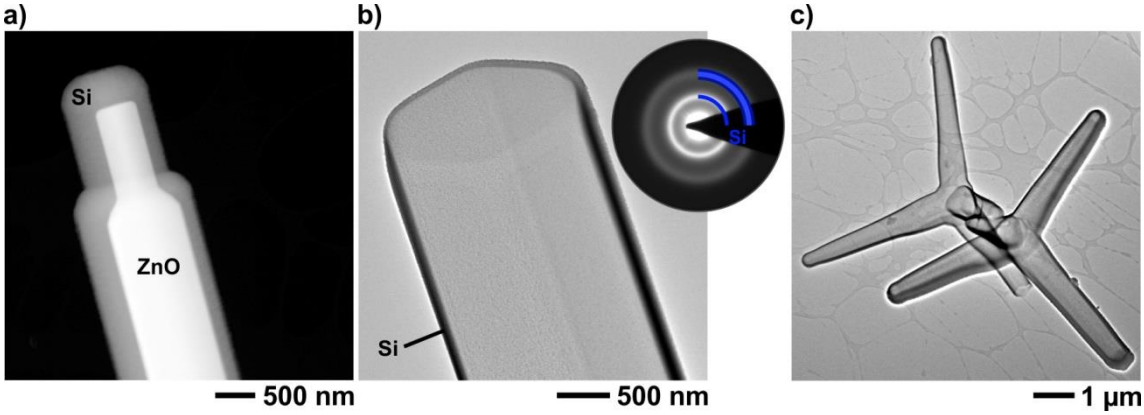


**Figure 4.11:** DF-STEM image of the tip of a Si-coated ZnO tetrapod. b) BF-TEM image of a silicon tip after etching away ZnO with corresponding SAED pattern in the inset. c) BF-TEM image of two adjacent *a*-Si tetrapods.

Different from spherical particles, the filling factor for tetrapodal-shaped particles is lower since large voids remain in agglomerations upon interlocking of their long arms. Consequently, the variation of their wall thickness is strongly reduced since the effect of shadowing from the plasma source is lower. For the first samples the wall thickness amounts between 30 and 50 nm at the tips. Figure 4.11 a depicts the tip of a ZnO tetrapod after coating by Si which appears darker in DF-contrast mode due to its lower atomic number. A comparable tetrapod arm after etching is shown in BF-contrast mode Figure 4.11 b, and as reference, two neighboring and intact tetrapods are displayed in Figure 4.11 c. In the following, two strategies were focused on: 1. reduction of the wall thickness to synthesize small and light tetrapods and 2. increasing the thickness to obtain bigger and more robust tetrapods, e.g. for battery applications.

Thin tetrapods

The particle size was determined by using small ZnO tetrapods as template structure. The coating thickness was adjusted by the PECVD parameters *time* and *$SiH_4$ flow* (see Table 5).

**Table 5:** PECVD process parameters for thin and thick silicon walls.

| Wall type | Time | $SiH_4$ flow |
|---|---|---|
| thin | 15 min | 120 sccm |
| thick | 25 min | 240 sccm |

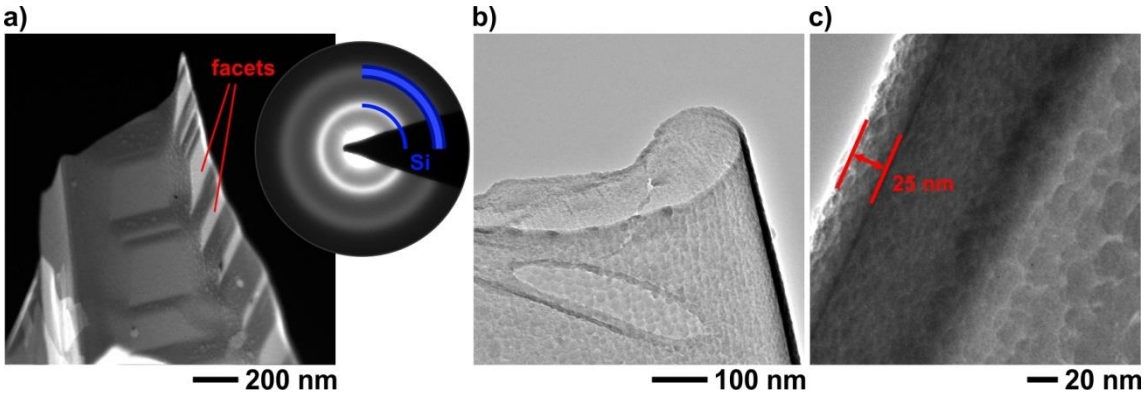


**Figure 4.12:** a) STEM image of a broken tetrapod arm with a faceted surface and corresponding SAED pattern in the inset. b) BF-TEM image from a similar position. c) Higher magnified BF-TEM image of a tetrapod wall.

For thin walls a lower silane concentration as well as a shorter process time was applied. With decreased wall thickness the tetrapods are more fragile, yet still a high amount was intact. A slightly faceted profile was observed (see Figure 4.12 a), which was effected by the ZnO template and was not compensated by deposition. The wall

thickness was measured to about 25 nm (Figure 4.12 b, c) near the tip and 100 nm at the center. Furthermore, defined and homogeneous domains of 20 nm in diameter were recognized at the surface. Hence, the silicon walls show a pre-state of columnar growth as they consist of a monolayer of Si domains where each domain represents a seed for a growing column in case of further deposition. According to SAED (Figure 4.12 b), the silicon is completely amorphous.

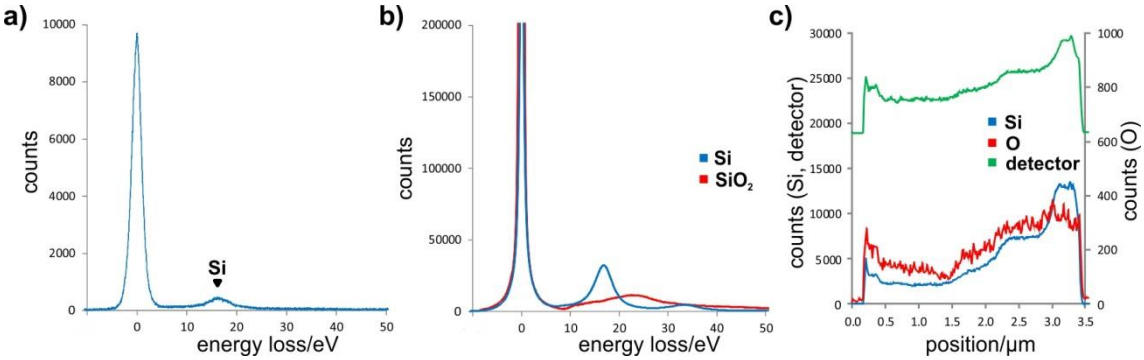


**Figure 4.13:** EEL spectra: a) measured at a thin tetrapod wall and (b) reference curves for Si[134] and amorphous $SiO_2$[135]. c) STEM-EDX linescan across a tetrapod's arm.

The oxidation level was determined by EDX analysis to 3-5 at.%, which is slightly lower than for S-Si particles. Here, EELS was applied to examine the presence of $SiO_2$. An EEL spectrum from a tetrapod wall is presented in Figure 4.13 a. Next to the zero-loss peak, the excerpt reveals a plasmon peak at 17 eV which is characteristic of pure silicon also depicted by a reference spectrum (Figure 4.13 b). According to the second curve, the presence of $SiO_2$ in T-Si is excluded since the characteristic plasmon peak at 24 eV was not detected. The STEM-EDX linescan across a tetrapod arm reveals a homogeneous oxygen level since the oxygen signal correlates with the silicon signal. Thus, it can be reasoned that oxygen is present in form of minor $SiO_x$ surface contamination.

To examine the behavior in case of high-temperature applications, an *in situ* heating experiment was performed. Starting at room temperature the sample was heated to 500 °C in 100 °C steps, to 750 °C in further 50 °C steps and finally to 1000 °C in 20 °C steps while in parallel BF-TEM and corresponding SAED images were captured. No changes were detected until spontaneous crystallization occurred at 780 °C which agrees with previous studies on amorphous Si[136]. The initially smooth shapes of amorphous Si domains change and sharp edges appear (compare Figure 4.14 a, b). The corresponding SAED pattern features defined Debye-Scherrer rings indicating the formation of nanocrystalline Si domains. Further heating promotes grain coarsening demonstrated by bigger dark particles in Figure 4.14 c and sporadic stronger reflections in the diffraction rings in the corresponding SAED pattern. Apart from

microstructural changes the overall shape of the tetrapods does not change, no holes or fractures were recognized.

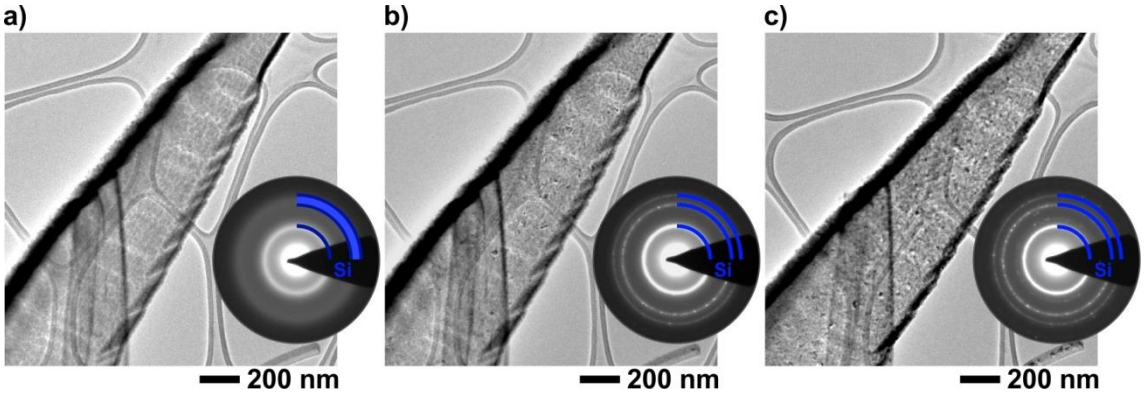


**Figure 4.14:** BF-TEM images and corresponding SAED patterns in insets during *in situ* heating of amorphous T-Si. a) T = RT. b) Spontaneous crystallization at T = 780 °C. Gradual grain coarsening depicted at T = 920 °C.

Thick tetrapods

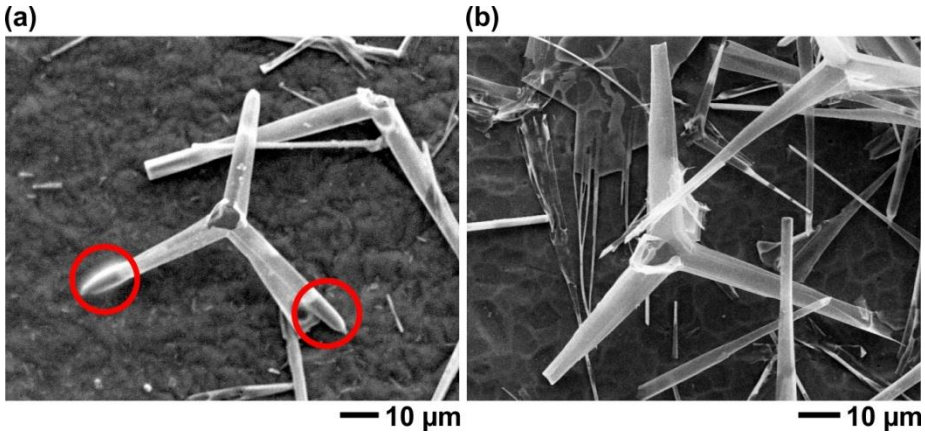


**Figure 4.15:** SEM images of thick tetrapods. a) Remaining ZnO in tetrapod tips marked by red circles. b) Fractured tetrapod with one arm missing.

To synthesize thicker tetrapods a similar starting template as for the thin tetrapods was utilized, but with increased size. The tetrapods' arm lengths measure about 20-50 µm and 3-10 µm in diameter. Listed in Table 5, the PECVD procedure was modified to provide a higher $SiH_4$ concentration during deposition at an increased process time. The SEM image from tetrapods after etching (Figure 4.15 a) reveals that the increased wall thickness hinders the etching of ZnO since small fractions likely remain in the tetrapods' tips. Therefore, the etching time was increased as well. After longer etching time, ZnO-free tetrapods were obtained (see Figure 4.16 a). Despite increased wall thickness, their toughness is not remarkably higher than for the thin tetrapods. Many

broken tetrapods were recognized (see Figure 4.15 b), which is explained by their increased size and their resulting higher prying effects.

TEM characterization of the long-time etched Si tetrapods confirms a successful removal of ZnO. By EDX analysis, only Si and O (20 at.%) were detected, indicating a high content of $SiO_2$. The wall thickness was measured to 50-85 nm (Figure 4.16 b, c) being thinner than it was for previously investigated tetrapods. Especially at the tips, the thickness was determined to be lower, which explains the high amount of broken tips.

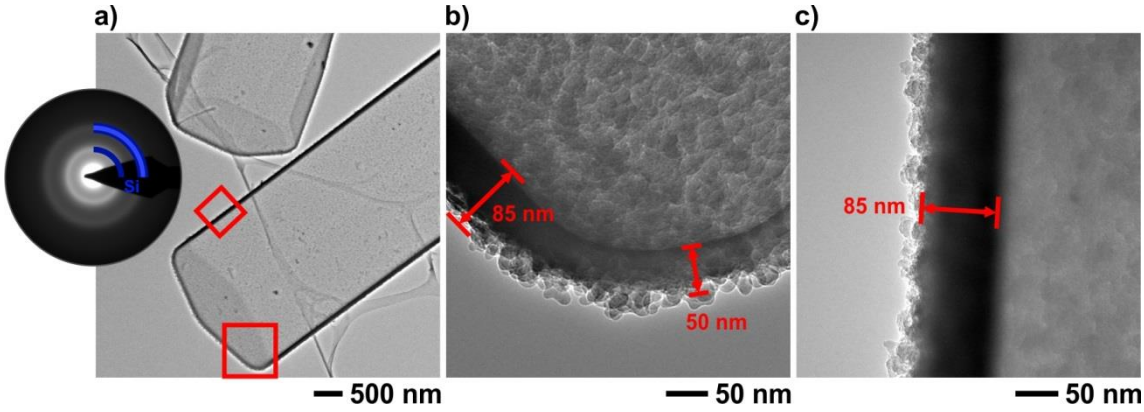


**Figure 4.16:** a) BF-TEM image of two adjacent thick tetrapod tips after long-time etching. The SAED pattern of the lower tetrapod is shown in the inset. b) Detail from lower square region in (a). c) Detail from upper square region in (a).

The morphology of the particles differs slightly from the previously presented thin-walled ones. The inner surface, which was in contact with the template, remained even, but the outer surface appears grainy and rough. By deposition, a shell of agglomerated particles forms with increased sizes compared to the previous tetrapods. Their amorphous character is demonstrated by SAED (Figure 4.16 a) revealing blurred rings which correspond to silicon.

### 4.3 Summary

Applying different synthesis approaches different types of silicon products were fabricated and determined to be principally amorphous. By chemical extraction, highly porous Si structures were obtained which show particle coalescence starting from 150 °C, but stay amorphous up to 650 °C before irreversible crystallization starts. Furthermore, the amorphous allotrope was found to be more beam- and temperature-sensitive. Hence, if the porosity is beneficial, e.g. to supply a large surface area, this type of amorphous silicon must not by heated to temperatures above 150 °C (100 °C for the allotrope). Although a direct differentiation from, for example, HRTEM micrographs was not possible due to the overall amorphous character of both

modifications, it was shown that they form nanoparticles of different sizes. A subsequent electrochemical characterization revealed a low conductivity and poor long-term performance of the amorphous Si applied in a battery anode. Due to perfect miscibility, a related compound with additional germanium was synthesized. It provides higher conductivity, but suffers from strong capacity fading during the first cycles. Furthermore, beam-induced recrystallization was observed. Occurring in a battery caused, for example, by heat, recrystallization reduces the compound's porosity and surface area and, eventually, its capacity.

Hollow amorphous silicon structures were fabricated by sacrificial template synthesis on ZnO. Inhomogeneous orientation-dependent growth was shown to cause strong variations of thickness and, locally, of surface characteristics with potential pull linkages. Here, tetrapodal-shaped template particles offer a more homogeneous deposition profile than do spherical-shaped particles due to a lower packing density. Their wall thickness is shown to be adjustable by the deposition process in order to fabricate thin-walled light particles or more robust, thick-walled particles, e.g. for application as battery materials. In case of thick-walled particles, their decreased structural stability upon increased size has to be considered, which needs to be compensated by increased wall thickness.

# 5 Spinel-type transition metal oxides

Conversion reactions are chemically simple and effective processes for energy storage and release in batteries. The first available rechargeable battery developed by Goodenough et al.[4] already included a $LiCoO_2$ cathode. During charging, cobalt(II) oxide was reduced by a Li-containing electrolyte to form metallic cobalt and lithium oxide. Currently applied battery types comprise, for example, e.g. $LiCoO_2$[137] (LCO), $LiNi_{0.33}Mn_{0.33}Co_{0.33}O_2$[138] (NMC) and $LiNi_{0.8}Co_{0.15}Al_{0.05}O_2$[139] (NCA), all of which are layered compounds with theoretical specific capacities of about 270 $mAhg^{-1}$.

Unlike intercalation compounds, e.g. carbon, conversion materials can incorporate more than one Li ion per formula unit. There are generally two classes of conversion materials applied as battery materials: 1. alloy forming materials, e.g. Si (see Chapter 3) and 2. transition metal compounds. First applications of transition metal compounds were reported by Poizot et al., who examined oxides of Co, Ni, Cu and Fe exhibiting capacities of about 700 $mAhg^{-1}$ and good capacity retention[140]. Even higher capacities can be achieved by substitution and mixing of different transition metals, but with worse cycling stability [141,142].

In the following, different recently synthesized spinel-type transition metal oxides applicable as anode materials are compared, including two types without cobalt. Spinel-type minerals[143] (Figure 5.1) are primarily $AB_2O_4$-type metal oxides with a distorted cubic close-packed lattice formed by $O^{2-}$ ions with $B^{3+}$ ions occupying half the octahedral holes and $A^{2+}$ ions occupying one-eighth of the smaller tetrahedral holes. Compositions focused on within this work are $CoFe_2O_4$, $CoMnFeO_4$ and $NiFe_2O_4$, which have been synthesized by Dr. Stefan Permien at the Institute of Inorganic Chemistry at Kiel University[144]. Electrochemical experiments were also performed by Dr. Permien.

The general cycling mechanism of spinel-type batteries is sketched in Figure 5.1. In the discharge reaction, the metal cations are reduced to metal atoms that formed nanoparticles accompanied by $Li_2O$ and SEI formation. Due to the high amount of oxygen, up to eight Li ions per formula unit can be converted. Thus, much higher capacities than for, for instance, $LiCoO_2$ are expected. Upon charging, the metal nanoparticles are oxidized again and Li gets recovered. Currently, these materials bear many drawbacks, most prominently a strong capacity fading already starting from the first cycles[145]. Furthermore, large volume changes during cycling and passivation of the nano-sized particles are detrimental for their performance[146]. The main task is to elucidate and compare the morphological as well as microstructural changes during cycling for the regarded electrolyte materials. Subsequently, the materials' suitability for battery applications will be estimated based on the monitored changes. Therefore, all three compounds mentioned above are characterized before and after cycling by *ex situ* TEM.

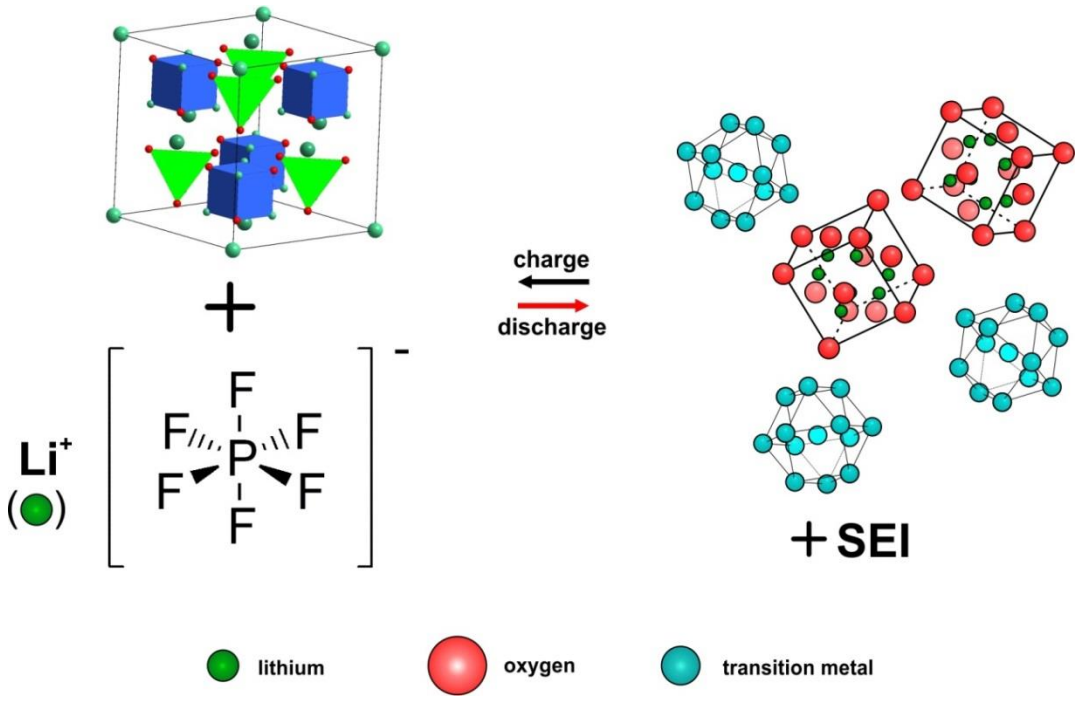


**Figure 5.1:** Charge/discharge mechanism of a spinel-type conversion battery.

Sample preparation

All materials were supplied by Dr. Permien in form of black powders sealed in glassy ampules. Being highly sensitive to oxygen and moisture, all samples were handled and prepared in a glovebox under argon atmosphere. A thorough mechanical grinding procedure was applied to the electrode materials, which still contained remaining agglomerations of spinel particles and dried SEI. A small amount of homogeneous fine powder was dropped onto a TEM grid. Mounted to the holder the sample was transferred to the TEM in an argon-filled bag and inserted during $N_2$ counterflow.

### 5.1 $CoFe_2O_4$

The spinel compound $CoFe_2O_4$ with a theoretical specific capacity of 916 $mAhg^{-1}$ was considered as potential anode material in previous studies[147,148]. Compared to commercialized products known shortcomings are a strong capacity fading and large volume changes during charging/discharging[149]. Reduced graphene oxide (rGO) was added to $CoFe_2O_4$ as it was already reported to increase the electrical conductivity of the compound[150]. For synthesis iron and cobalt nitrate were mixed with nitric acid and ball-milled. The resulting viscous product was decomposed by heating to obtain spinel nanoparticles according to the following process:

$$Co(NO_3)_2 \cdot 6\,H_2O + 2\,Fe(NO_3)_3 \cdot 18\,H_2O \rightarrow CoFe_2O_4 + 8\,HNO_3 + 20\,H_2O$$

Suspended in water, rGO was added to obtain a slurry which was let to dry. An electrochemical characterization was performed by Dr. Permien for both, uncycled and cycled samples[151]. As intended, the rGO-supported sample shows higher cycling stability. Its starting capacity of about 900 $mAhg^{-1}$ is slightly lower than that of the rGO-free sample due to the lower capacity of graphene. But after 90 cycles at C/5, the rGO-containing sample exhibits a superior capacity of 700 $mAhg^{-1}$, which is nearly double the capacity of the rGO-free type. Thus, the rGO-supported spinel compound was investigated by TEM before cycling, after uptake of 2 Li ions per formula unit and also after cycling for ten times.

Before cycling

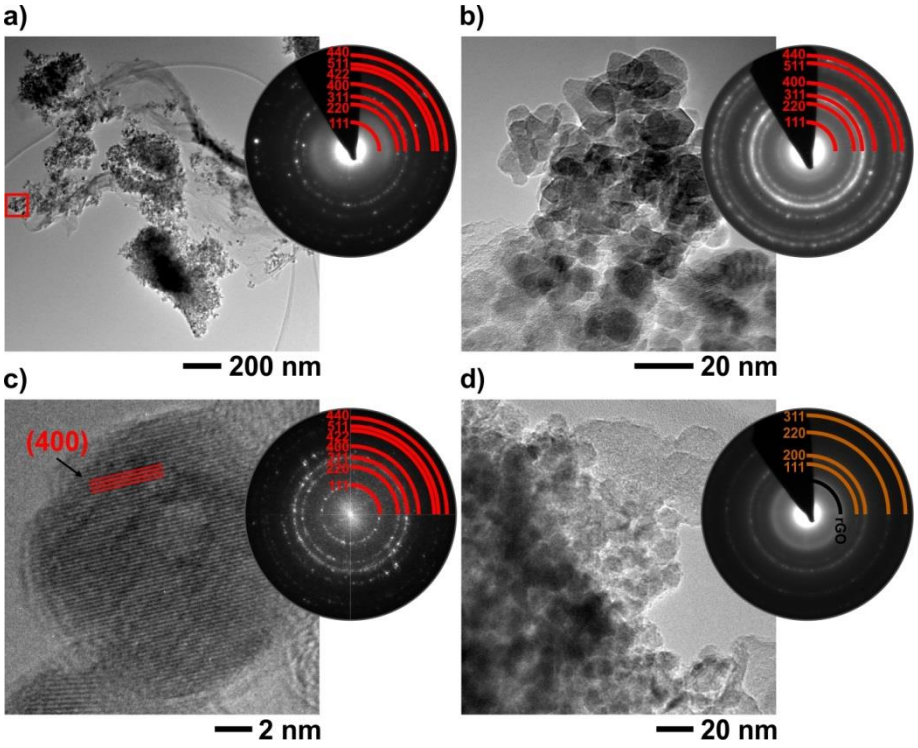


**Figure 5.2:** Uncycled $CoFe_2O_4$/rGO compound. a) BF-TEM image of agglomerated $CoFe_2O_4$ nanoparticles attached to a rGO sheet. b) Detailed BF-TEM image of a small agglomeration of nanoparticles with corresponding SAED pattern. c) HRTEM micrograph of a single particle. Parallel red lines indicate $CoFe_2O_4$ (400) planes. The inset depicts the corresponding calculated FFT pattern. d) BF-TEM image of the uncycled compound after uptake of 2 Li ions per formula unit. Reflections of the corresponding SAED in the inset correspond to cubic CoO (brown lines) and carbon (black line).

The thusly prepared sample consists of agglomerated nanoparticles with sizes of 6-15 nm (see Figure 5.2 b) in good contact to rGO (Figure 5.2 a). The crystalline character of the nanoparticles is demonstrated by the HRTEM micrograph (Figure 5.2 c) of a single particle with clearly visible (400) planes from $CoFe_2O_4$, and SAED data (Figure 5.2 b, inset) which exhibits circularly arranged reflections that correspond to $CoFe_2O_4$[152] in

accordance with XRD results[151]. By TEM-EDX analysis, the ratio of Co:Fe was determined to 1.00:2.01. XRD data recorded after Li uptake indicates the presence of a monoxide phase. TEM-EDX analysis of a part of the sample (Figure 5.2 d) reveals a Co:Fe ratio of 1.00:1.92 meaning a slight excess of Co. By SAED analysis (Figure 5.2 d, inset), reflections corresponding to cubic CoO were determined. Possible explanations for the increased Co content are a segregation of Co/Fe oxide during Li uptake or an incomplete synthesis of the spinel with excess CoO.

After 10 cycles

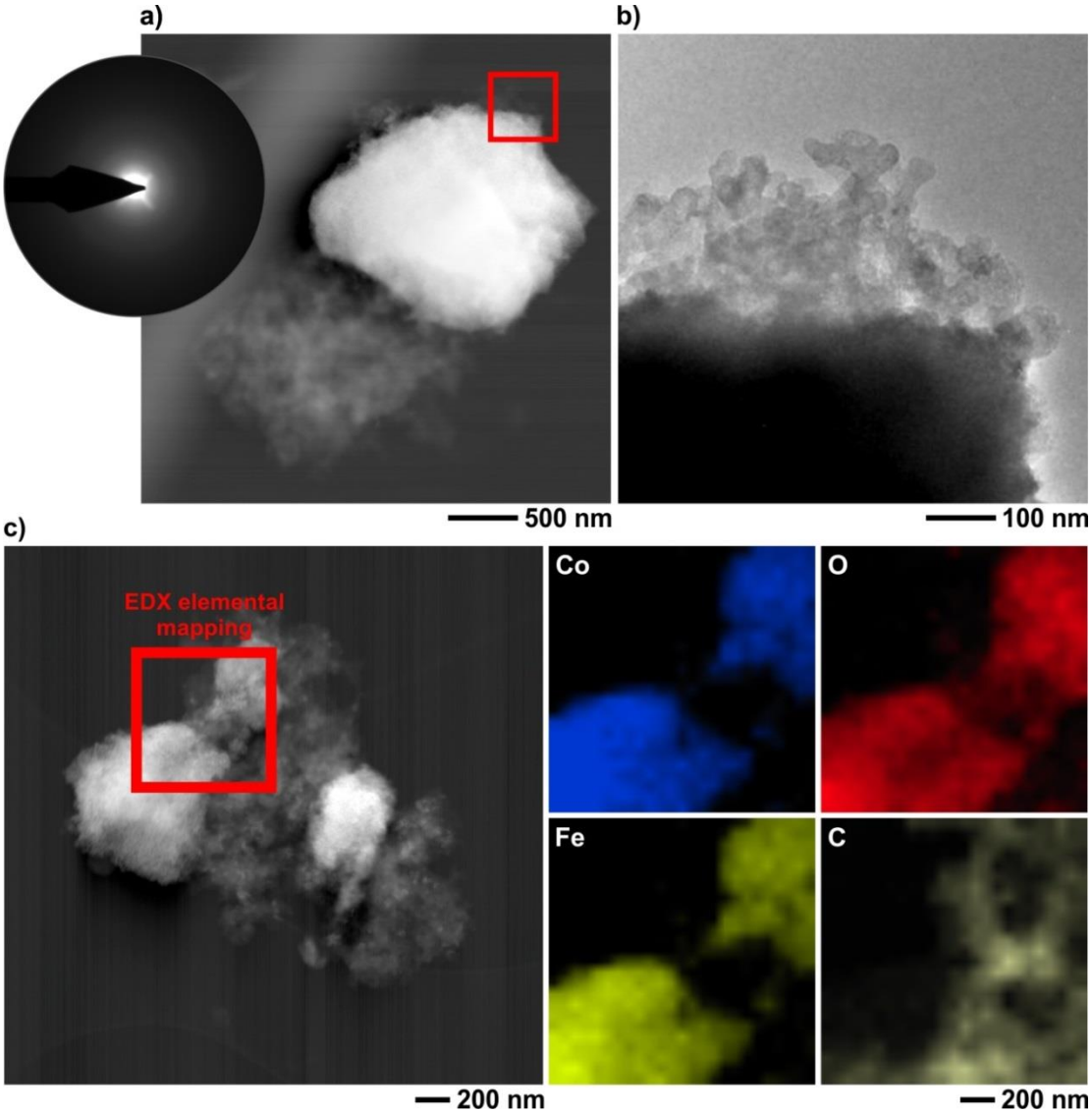


**Figure 5.3:** $CoFe_2O_4$/rGO after cycling. a) HAADF-STEM image of an oxide particle attached to carbon and a corresponding SAED image. b) Magnified view (BF-TEM) from surface region marked in (a). c) HAADF-STEM image of cycled $CoFe_2O_4$/rGO (left) and EDX elemental maps for Co, Fe, O and C (right) from the region marked on the left side.

For the first charging process, a reduction of $Fe^{3+}$ to $Fe^{2+}$ accompanied by a lattice transformation from spinel to rock-salt structure was reported[151]. During the proceeding Li uptake, $Fe^{2+}$ and $Co^{2+}$ are reduced to their metallic state:

$$CoFe_2O_4 + 2\,Li \rightarrow\ Li_2CoFe_2O_4$$

$$Li_2CoFe_2O_4 + 6\,Li \rightarrow Co + 2\,Fe + 4\,Li_2O$$

By charging Fe and Co are oxidized again:

$$Co + 2\,Fe + 4\,Li_2O \rightarrow CoO + Fe_2O_3 + 8\,Li$$

Different from the initially present spinel phase, the cycled product does not exhibit a long-range order. A mixed-oxide compound was assumed as specified by the reaction equations. Figure 5.3 a depicts an oxide particle in HAADF-STEM mode attached to carbon. SAED data (Figure 5.3 a, inset) reveals its entirely amorphous structure. At higher magnification (Figure 5.3 b) the particle was shown to consist of a network of small agglomerated particles with sizes between 25 and 50 nm. An EDX analysis revealed a Co:Fe ratio of 1.00:2.08 being close to the favored ratio of 1.00:2.00. Three particle agglomerations with sizes between 0.5 and 1.0 µm were analyzed. Next to the particles a light carbon structure was identified. To examine a potential segregation of Co and Fe species, EDX elemental mapping of the cycled oxide compound was performed as depicted in Figure 5.3 c. The maps for Co, Fe and O look similar, thus, an overall homogeneous distribution of CoO and $Fe_2O_3$ is concluded. The C map looks different from the other maps since the oxide particles are surrounded by carbon, depicting its suitability as promoting agent for cycling.

### 5.2 $CoMnFeO_4$

Commonly applied conversion-type batteries usually contain one (CoO) or two metals ($CoFe_2O_4$). Within this chapter, the potential of the three metals-containing $CoMnFeO_4$ as cathode material is examined. Already presented in former works[153,154], this compound was so far not considered for use in batteries, but the related compound $NiFeMnO_4$ exhibited a capacity of 750 $mAhg^{-1}$ after 50 cycles[155]. For synthesis similar to the previous $CoFe_2O_4$, nitrates were mixed with nitric acid and deionized water[146]:

$$2\,Co(NO_3)_2 \cdot 12\,H_2O + \ 2\,Fe(NO_3)_3 \cdot 18\,H_2O\ + 2\,Mn(NO_3)_2 \cdot 8\,H_2O \rightarrow 2\,CoMnFeO_4 + 14\,HNO_3 + 30\,H_2O + \ H_2$$

It should be noticed that the oxidation number of Mn gets increased from +2 to +3 during compound formation. Different from Ni and Fe, Mn has a complex atomic structure, the α-Mn type. By X-ray absorption near edge structure spectroscopy

(XANES), it was discovered that during the first charging procedure Mn ions are first irreversibly reduced from $Mn^{3+}$ to $Mn^{2+}$ accompanied by a partial loss of capacity[146]. Electrochemical analysis exhibited a starting capacity of 970 $mAhg^{-1}$, and 717 $mAhg^{-1}$ after 50 cycles at C/10. With a 26 % loss of capacity after the first 50 cycles this compound performs worse than $CoFe_2O_4$ with about 22 % loss after 90 cycles. By TEM, the spinel compound (containing 10 wt.% carbon and 10 wt.% binder) was investigated before cycling and after cycling for three times at C/10.

Before cycling

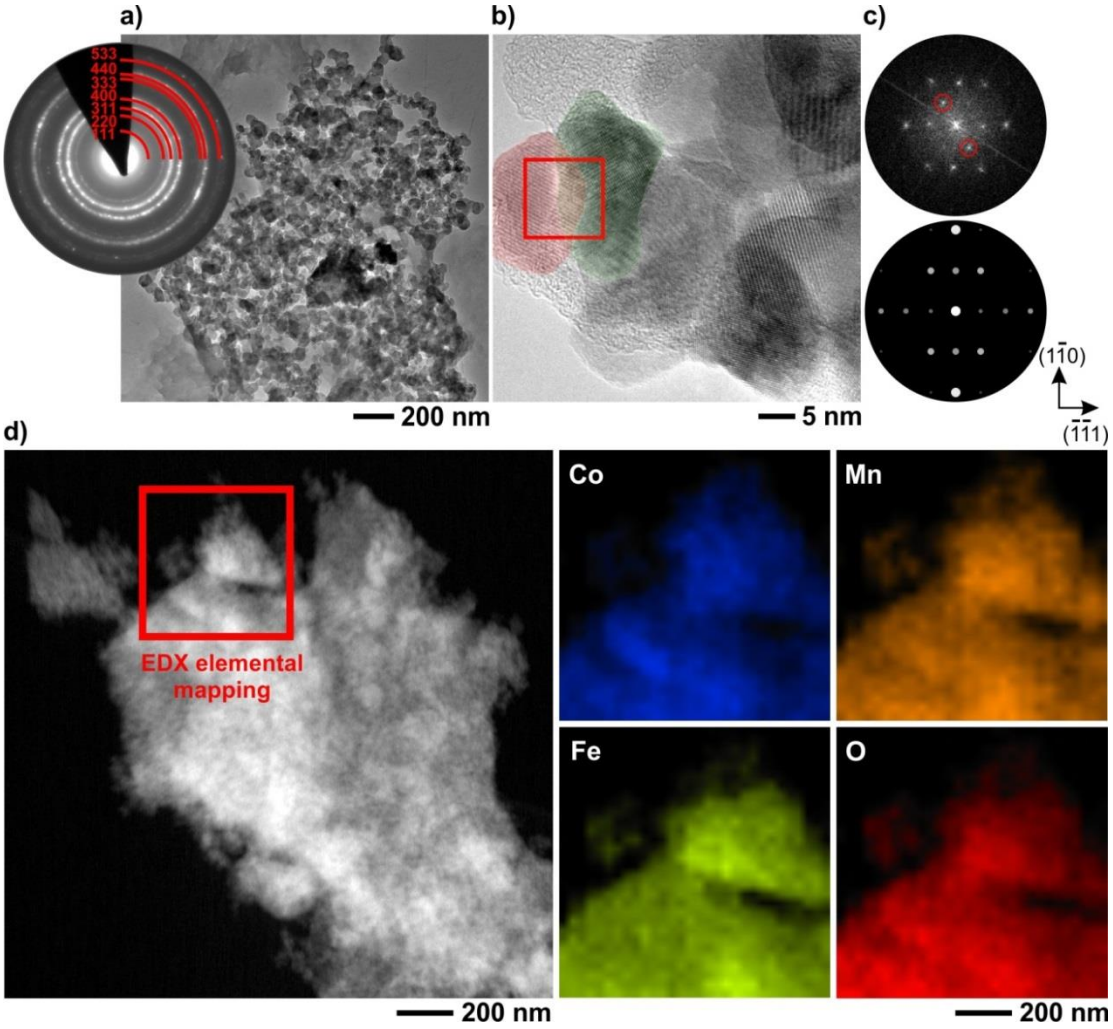


**Figure 5.4:** $CoMnFeO_4$ before charging. a) BF-TEM image of agglomerated nanoparticles with corresponding SAED pattern in the inset. b) HRTEM micrograph of coalesced particles (colored red and green). c) Calculated FFT pattern (top) from square-shaped region marked in (b). The red-circled intensities and their higher orders originate from the red-colored particle in (b). Simulated ED pattern (bottom) for the [112] zone axis of $CoFe_2O_4$. d) EDX elemental maps for Co, Mn, Fe and O.

In its uncycled state $CoMnFeO_4$ is present as porous framework of agglomerated nanoparticles (Figure 5.4 a) with an average size of 8 nm. By HRTEM, the particles are

shown to be crystalline (see Figure 5.4 b) and respective SAED patterns depict similar ring patterns as for $CoFe_2O_4$. The corresponding d-values are distinctive for the expected spinel structure that was already determined by XRD data[146]. FFT patterns of crystalline particles agree with to simulated ED patterns (see Figure 5.4 c) with small deviations. The d-value for (111) was measured to 0.482 nm, being close to the reported value of 0.485 nm for $CoFe_2O_4$[152]. Frequently, coalesced particles were determined (see Figure 5.4 b). EDX elemental mapping of a surface-near particle was performed for the three metals Co, Mn and Fe (see Figure 5.4 d). For the investigated region no concentration gradients were identified and a homogeneous distribution of the metal oxides is assumed. By EDX, the ratio Co:Mn:Fe was determined to 1:00:1.15:1.10 offering a slight lack of Co, which is assumed to result from the synthesis procedure.

After three cycles

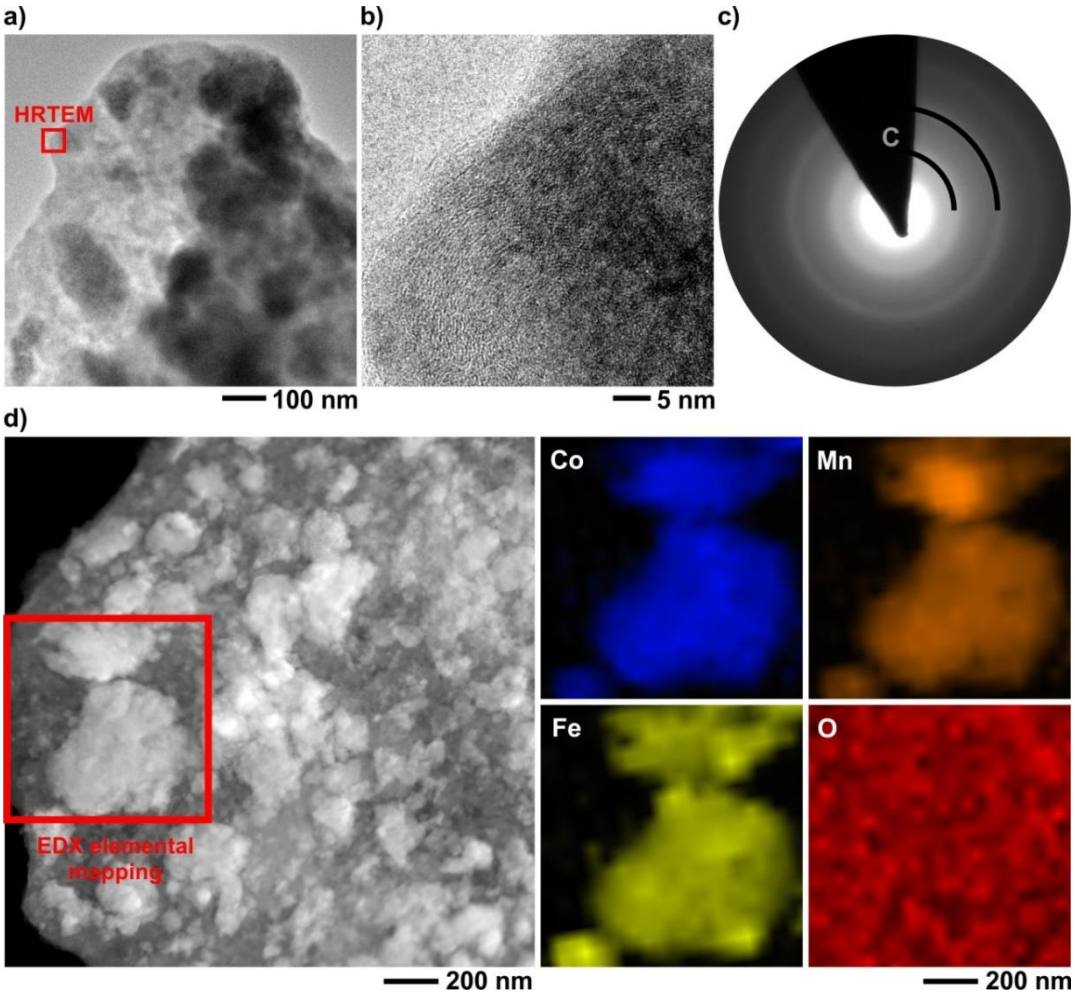


**Figure 5.5:** $CoMnFeO_4$ after three charge/discharge cycles. a) BF-TEM of metal oxide particles surrounded by the SEI. b) HRTEM micrograph of square-shaped region marked in (a). c) SAED pattern from (a). d) EDX elemental maps for Co, Mn, Fe and O.

By comparing BF-TEM images of $CoMnFeO_4$ before (Figure 5.4 a) and after the first cycles (Figure 5.5 a), a transformation of the initially agglomerated nanoparticles was noticed forming particles with sizes of up to 300 nm surrounded by an SEI matrix. Their amorphous nature is demonstrated by HRTEM (Figure 5.5 b) and SAED (Figure 5.5 c) data. The amorphous rings marked in the SAED pattern correspond to C from the TEM grid. The elemental maps reveal local concentration gradients for Mn (see Figure 5.5 d) which was not detected before cycling. By EDX, the Co:Mn:Fe ratio was determined to 1.00:1.10:1.00, but a correlation between Mn excess and segregation of Mn could not yet be confirmed. The consistent distribution of oxygen is explained by the oxygen-containing SEI.

### 5.3 $NiFe_2O_4$

The cobalt-free spinel compound $NiFe_2O_4$ was obtained by a solvothermal synthesis of a mixture of hydrated nickel and iron nitrate according to the following reaction:

$$Ni(NO_3)_2 \cdot 6\,H_2O + 2\,Fe(NO_3)_3 \cdot 18\,H_2O \rightarrow NiFe_2O_4 + 8\,HNO_3 + 20\,H_2O$$

Electrochemical characterizations before and after cycling revealed large capacity fading[144]. A critical point was the large capacity drop (about 20 %) detected after the first cycle. In order to reduce subsequently strong capacity fading, CNTs were added during synthesis, which were reported to improve the cycling stability by crosslinking of particles[156]. The capacity was measured to 1001 $mAhg^{-1}$ after the first cycle, and remained near to constant for the following 40 cycles (933 $mAhg^{-1}$) at C/10. Without CNTs a slightly higher capacity was detected (1092 $mAhg^{-1}$) after the first cycle, but followed by strong fading of about 60 % after 40 cycles. Cycled samples presented in the following also contain CNTs.

For a more fundamental understanding, TEM investigations were performed to monitor occurring changes on the microscale. The morphology of the pristine compounds is depicted in Figure 5.6 a. Agglomerations of nanoparticles with sizes between 10 and 80 nm were detected sharing a rhombic plate-like shape with sharp edges. The reflections in the corresponding SAED pattern correspond to $NiFe_2O_4$[157] and $Fe_2O_3$[158]. It should be noted that reflections for NiO principally overlap with reflections from $NiFe_2O_4$ due to its parental lattice type (Fm-3m[159]; $NiFe_2O_4$: Fd-3m) and the lattice parameter $a_{NiO}$ being exactly half the size of $a_{NiFe_2O_4}$. BF-TEM images depict, that the particle density was lower for the sample with added CNTs (Figure 5.6 c) which were found to form a network surrounding the $NiFe_2O_4$ plates. In the SAED patterns the CNTs were represented by diffuse rings (see Figure 5.6 d) with d-values of 0.344 nm and 0.210 nm, which correspond to graphite[160]. By EDX analysis, the carbon content of the CNT-containing specimen was quantified to 19.4 at.%. Most reflections correspond

to $NiFe_2O_4$, but similar to the specimen without CNTs, $Fe_2O_3$ was recognized at several positions. By EDX measurements, the Ni:Fe ratio at the particular regions was determined to 1.00:2.17.

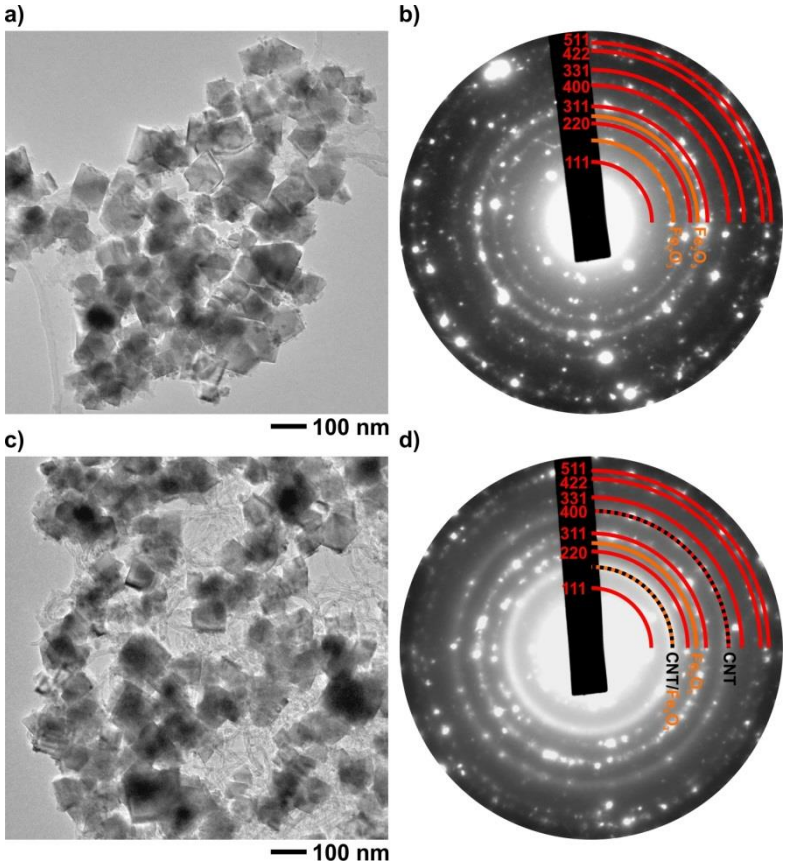


**Figure 5.6:** $NiFe_2O_4$ without CNTs: a) BF-TEM image of close-packed defined particles. b) SAED pattern from (a) with red-colored indexed rings corresponding to $NiFe_2O_4$ and orange rings from $Fe_2O_3$. $NiFe_2O_4$ with CNTs: c) BF-TEM image depicting less dense packing of particles due to surrounding CNTs. d) SAED pattern from (c) being similar to (b) except additional diffuse rings which correspond to graphite, the basic structure of CNTs.

Former experiments[145], particularly XRD and X-ray absorption spectroscopy (XAS) already uncovered chemical processes which occur during Li uptake. A reduction and subsequent movement of $Fe^{3+}$ ions was observed due to decreased intensities of spinel-typical reflections in the corresponding patterns. The basic reactions proceeding during charging and discharging are assumed to be one-step mechanisms:

Initial discharge: $NiFe_2O_4 + 8\,Li \rightarrow Ni + 2\,Fe + 4\,Li_2O$

Charging: $Ni + 2\,Fe + 4\,Li_2O \rightarrow NiO + Fe_2O_3 + 8\,Li$

Consequently, the spinel structure gets destroyed upon discharge and separated oxides form through charging. In the beginning, $Fe^{3+}$ ions are reduced to $Fe^{2+}$ ions and

$Ni^{2+}$ and $Fe^{2+}$ ions are subsequently reduced simultaneously. Two samples were measured, one after the first successful charge/discharge cycle and another after 10 of these successful cycles in order to examine the distribution of metal oxides and CNTs.

After the first cycle

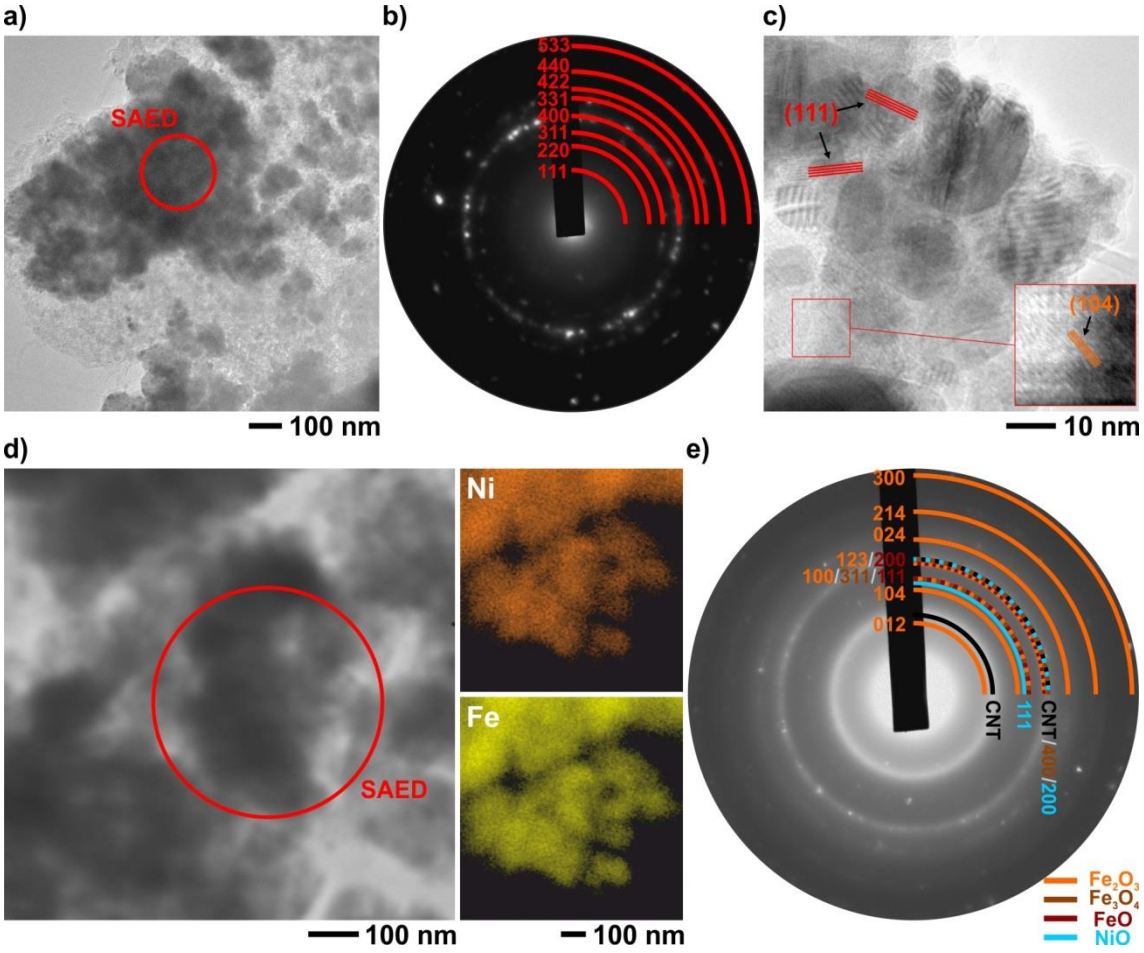


**Figure 5.7:** $NiFe_2O_4$ after the first charge/discharge cycle. a) BF-TEM image of round-shaped particles (dark) in the SEI matrix. b) SAED pattern from region marked in (a) with intensities corresponding to $NiFe_2O_4$. c) HRTEM micrograph of round-shaped particles with visible lattice planes from $NiFe_2O_4$ marked by red lines. The magnified inset depicts $Fe_2O_3$ lattice planes. d) EDX elemental maps for Fe and Ni. e) SAED pattern from region marked in (d) features reflections rings and scattered intensities corresponding to different $Fe_xO_y$ species, NiO and CNTs indicated by different colors.

The morphology of $NiFe_2O_4$ after the first cycle (Figure 5.7 a) differs remarkably from its initial state (compare Figure 5.6 c). Predominantly round-shaped particles with diameters from 10 to 200 nm were detected forming agglomerations surrounded by intact CNTs. The initially rhombic plates get decomposed through reduction in the discharge step and reassembled during charging as a mixture of NiO and $Fe_xO_y$. By SAED (Figure 5.7 e), the presence of NiO and different $Fe_xO_y$ species is demonstrated.

Due to many similar d-values and subsequent overlapping in the patterns, only a qualitative evaluation in combination with previous XRD results is possible. Higher levels of $Fe_2O_3$ compared to FeO and $Fe_3O_4$ are suggested according to their reflection intensities. The crystalline nature of those particles is demonstrated by HRTEM (see Figure 5.7 c). Parallel lines were observed and identified as (111) planes from $NiFe_2O_4$ and (104) planes from $Fe_2O_3$. Moiré patterns were frequently observed at regions where particles with different orientation or composition overlap. A macroscopic segregation of Ni and Fe, NiO and $Fe_xO_y$ respectively, was not observed. EDX elemental maps of Ni and Fe demonstrate a homogeneous distribution of both elements. Still, SAED patterns (see Figure 5.7 b) were recorded with reflections corresponding to $NiFe_2O_4$. Presumably through incomplete conversion during the first cycle, a little amount of the original spinel structure remained. EDX elemental mapping at a surface-near region was performed for both elements Ni and Fe (see Figure 5.7 d). For the investigated region no concentration gradients were identified, and a homogeneous distribution of Ni and Fe is assumed. The Ni:Fe ratio was determined to 1:00:2.28. Possible explanations for the slight excess of Fe are: 1. a Fe excess already after preparation in coincidence with the SAED patterns (Figure 5.6 b, d) which indicated the presence of $Fe_2O_3$ (still considering that NiO cannot be discriminated from $NiFe_2O_4$ by SAED). 2. diffusion of Ni/Fe at a larger scale. Thus, the charged anode would contain Ni-rich regions which were not analyzed.

After 10 cycles

No remarkable morphological changes were recognized after nine more cycles. Figure 5.8 a depicts an agglomeration of Ni and Fe compounds surrounded by the SEI matrix. By SAED, $NiFe_2O_4$ was detected (compare Figure 5.8 b) presumably remaining in core regions of thicker particles or at sites inaccessible to the electrolyte. Embedded into the SEI matrix and between $M_xO_y$ particles, intact CNTs were identified (Figure 5.8 c) indicating that this carbon species is a well-suited additive for the $NiFe_2O_4$ system. Representative of most regions of the sample, EDX elemental maps for Ni and Fe at a surface-near region (see Figure 5.8 d) demonstrate a homogeneous distribution of both elements. The Ni:Fe ratio was determined to 1.00:1.96, which is close to the ideal ratio 1.00:2.00. As for the once cycled sample the presence of NiO and different $Fe_xO_y$ species was identified by SAED (Figure 5.8 e). Thus, a reversible conversion of NiO and $Fe_2O_3$ to Ni and Fe and backwards is confirmed taking into account the electrochemical data from the successful cycling procedure[145].

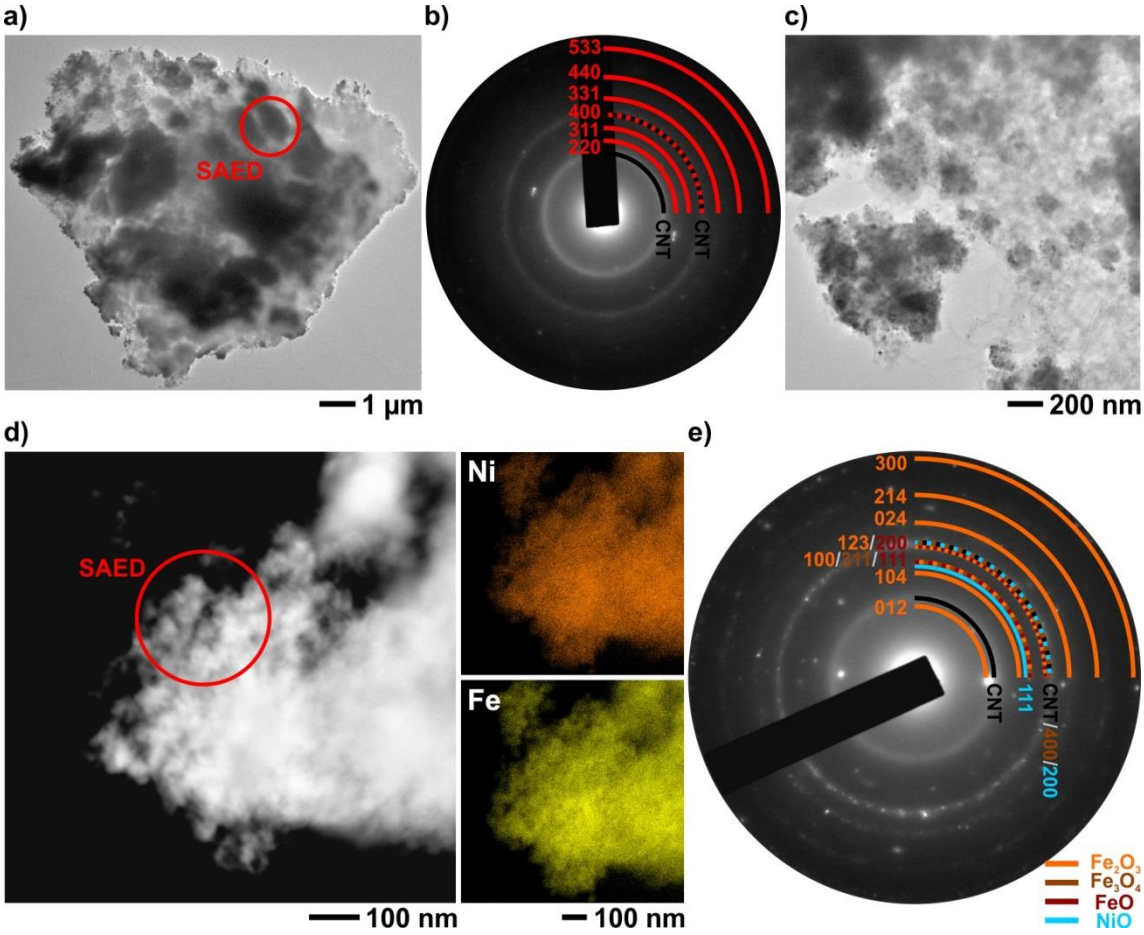


**Figure 5.8:** $NiFe_2O_4$ after 10 charge/discharge cycles. a) BF-TEM image of round-shaped particles (dark) in the SEI matrix. b) SAED pattern from region marked in (a) with intensities corresponding to $NiFe_2O_4$. c) BF-TEM image of smaller Ni/Fe compound particles next to CNT-containing SEI. d) EDX elemental maps for Fe and Ni. e) SAED pattern from region marked in (d) features reflections rings and scattered intensities corresponding to different $Fe_xO_y$ species, NiO and CNTs indicated by different colors.

## 5.4 Summary

The potential of new conversion-type cathode materials on the basis of transition metal spinels was elucidated. Different binary and ternary compositions, $CoFe_2O_4$, $CoMnFeO_4$ and $NiFe_2O_4$ in particular, were examined *ex situ* by TEM before and after cycling. Their microstructural evolution through cycling from spinel structure nanoparticles to agglomerated microcrystalline or amorphous mixed-oxide particles is demonstrated by HRTEM and SAED analysis. Elemental mappings of $CoFe_2O_4$ and $NiFe_2O_4$ reveal homogeneous distributions of the contained metals whereas $CoMnFeO_4$ shows slight segregation of Mn. Specific successfully integrated carbon modifications (rGO, CNTs) are shown to enhance the batteries' long-time performance without detrimental chemical and physical interaction. With 900 $mAhg^{-1}$ after 40 cycles ($NiFe_2O_4$) and 700 $mAhg^{-1}$ after 90 cycles ($CoFe_2O_4$) the achieved capacities are more

than the double that of commercially available rechargeable batteries[41]. The respective capacity losses amount 6 % ($NiFe_2O_4$) as well as about 25 % ($CoFe_2O_4$, $CoMnFeO_4$). It has to be considered that strong capacity losses occur in the first five cycles mainly due to an irreversible decomposition of the spinel structure. To estimate the suitability of the novel spinel materials for commercial applications, the performance after a larger number of cycles as well as the impact of elevated temperatures have to be examined.

# 6 Carbon-sulfur cathodes

Sulfurized carbon structures, recently developed by Dr. Hansen at the Institute for Material Science at Kiel University, will be introduced as a promising cathode approach to work in combination with high-performance Si-based battery anodes presented in Chapter 3. Superior to currently applied materials[3], e.g. $LiNi_{0.33}Mn_{0.33}Co_{0.33}O_2$ (NMC) or $LiNiCoAlO_2$ (NCA), providing gravimetrical capacities of 270 $mAhg^{-1}$, sulfur achieves up to 1320 $mAhg^{-1}$ by forming Li-S compounds[161]. The lithium-sulfur potential is only 2.2 V, instead of 3.6-4.0 V for the latter compounds. Yet the energy, that can be stored in total, can still be increased about a factor of four.

Compared to metals, a big drawback of sulfur is its weak conductivity, but it can be compensated by additives with high conductivity, e.g. carbon. Carbon nanotube (CNT) framework structures, developed by Fabian Schütt et al. [162] at the Institute for Material Science at Kiel University, were applied as a host matrix for sulfur to enable high electron conductivity. Both elements, carbon and sulfur, are widely available on earth and easy to extract, which is a further advantage over transition metals, manganese in particular. Moreover, the weight of the final batteries can be reduced due to a lower density of the compounded structure without heavier metals.

For energy conversion, a step-wise reaction of sulfur with the Li-containing electrolyte occurs upon cycling[161]:

$$S_8 \leftrightarrow Li_2S_8 \leftrightarrow Li_2S_6 \leftrightarrow Li_2S_4 \leftrightarrow Li_2S_2 \leftrightarrow Li_2S$$

The final product is $Li_2S$ which is insoluble and insulating[163]. Capacity fading occurs due to loss of active material through precipitation of $Li_2S$ particles inside pores and subsequent blocking of pathways for the electrolyte. To maintain consistently high cathode capacities, a stable carbon-sulfur compound with a suitable morphology has to be developed. Furthermore, the polysulfide shuttle-effect[164], which describes the diffusion of sulfur inside the cathode, has to be reduced. Detrimental effects in case of contact with sulfur are an emerging sulfur gradient and corrosion of the anode side. For this purpose, a porous cathode shape provides a comprehensive network of pathways enabling high electrolyte mobility although some pathways are partially blocked by attached insoluble polysulfides.

Fabrication

Similar to the tetrapodal silicon discussed in Chapter 4, a sacrificial template synthesis was performed to obtain a carbon network. ZnO tetrapods (Figure 6.1 a) were infiltrated by a CNT solution and heat-treated afterwards to form a surrounding network. After etching away ZnO, a highly porous and hierarchical structure remained[162], that provides a large and easily accessible surface for subsequent

infiltration of sulfur. Moreover, the presence of small and large pores effectuates a sponge-like behavior and enables a distributed storage of the electrolyte in the tetrapod arms to be directly accessible for the charge/discharge process. For later application as cathode in a battery, the tetrapodal structures were pressed to small cylindrical pellets, 2 mm thick, with a diameter of 10 mm. In the final step sulfur was introduced by applying a vapor-liquid-solid approach. Thus, elemental sulfur was heated to a temperature of 550 °C to enter the gas phase and subsequently got infiltrated into the graphite structure (see Figure 6.1 b, c, provided by Fabian Schütt).

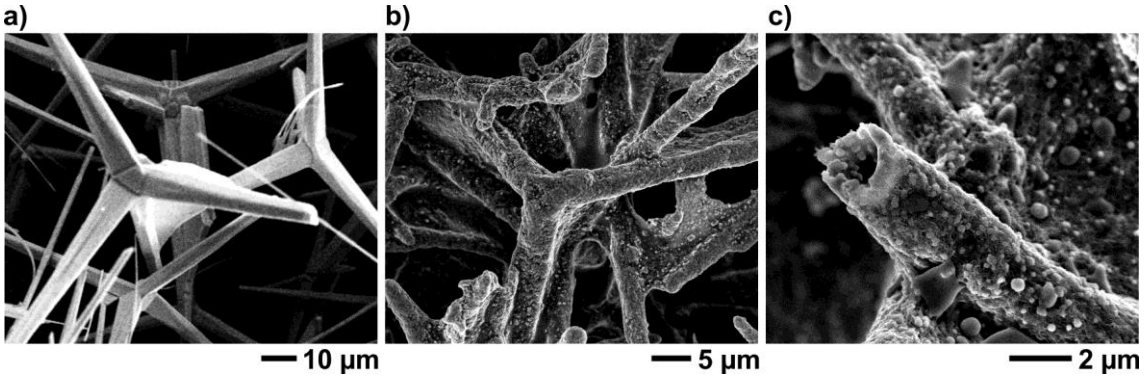


**Figure 6.1:** SEM images of tetrapodal structures. a) Pure-ZnO tetrapods. b) Tetrapodal CNT framework after sulfur infiltration. c) Broken tip of a sulfur-infiltrated tetrapod.

According to similar systems[165], the tetrapodal CNT network acts as conductive and retaining framework to compensate for the bad electrical conductivity of sulfur and to supply good accessibility by the electrolyte. Due to the carbonaceous nature of the host material, a detailed investigation of morphology and composition of the SEI by SEM/TEM will be difficult and was not done so far.

Handling of sulfur

Compared to the compounds presented in the previous chapters (Li-Si, TM spinels), an investigation of sulfur compounds is technically more challenging and rarely conducted[166]. Sulfur is potentially harmful to a TEM since it likely reacts with iron and thereby degrades sensitive parts, e.g. the pole pieces of the objective lens. Furthermore, sulfur is sensitive to the electron beam and gets evaporated, especially at the ultralow pressure in the TEM column. Thus, its handling requires care and experience to avoid damage of both – sample and instrument. Through careful and experienced preparation and handling of respective samples, first TEM observations on sulfur-containing compounds were successfully performed. To overcome radiation damage and partial evaporation of sulfur the sample was cooled during the experiment[166]. A cryo-TEM sample holder was used to cool the specimen to a

minimum of -173 °C with the aid of liquid nitrogen, directly filled into a small vessel being part of the sample holder.
The integration of sulfur into the structure also determines its stability. Elemental sulfur is more sensitive than sulfur compounds and will evaporate faster. But in case of chemical bonding of sulfur to the graphite framework, cooling might not be necessary.

### 6.1 Uncycled sample

The effectivity of the infiltration step of sulfur was investigated prior to the electrochemical cycling. A black cylindrical pellet was prepared for TEM investigation by manual grinding. The obtained fine powder was directly put onto a copper TEM grid with a lacey carbon film.

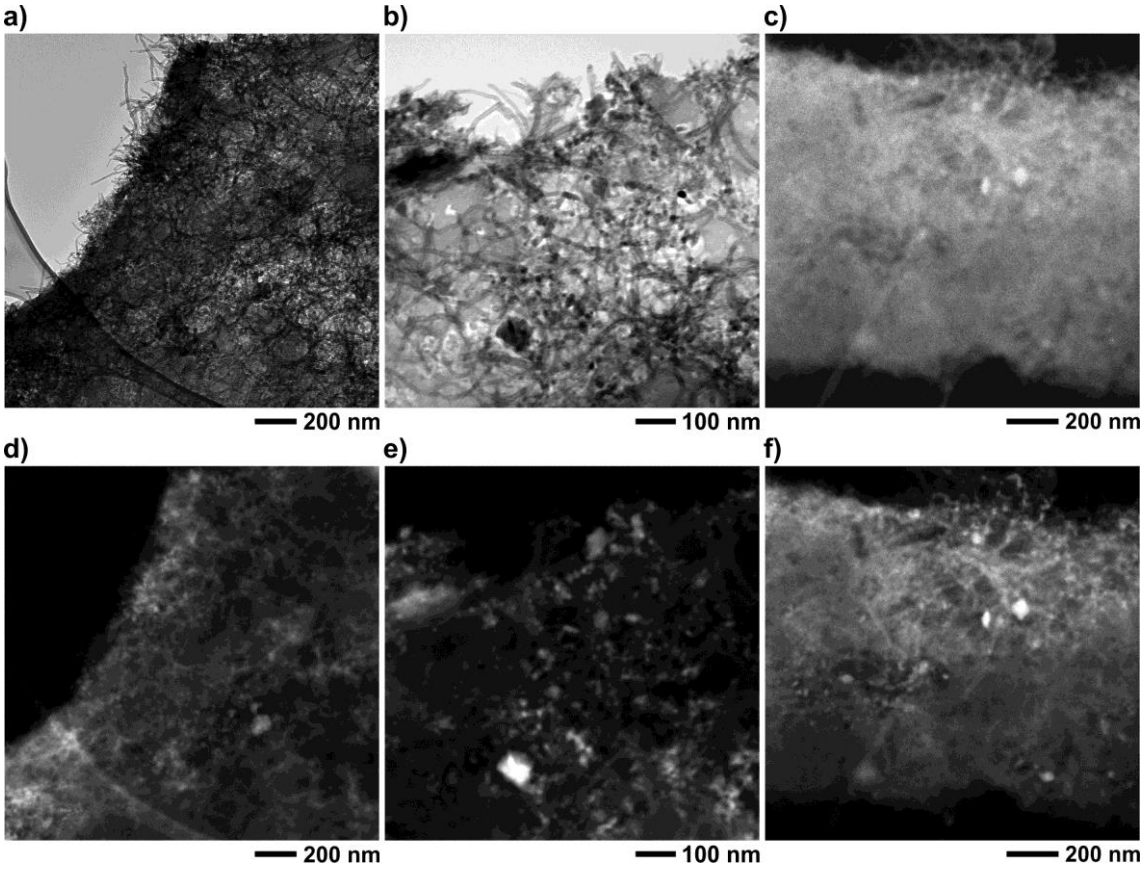


**Figure 6.2:** a, b) BF-TEM images of sulfurized CNT networks. c) EFTEM image of a CNT framework adjusted to the carbon K-edge. d-f) Sulfur K-edge EFTEM images corresponding to (a)-(c).

BF-TEM images of sulfurized carbon frameworks (Figure 6.2 a, b) depict that their porous and hollow character was maintained, and randomly oriented CNTs were observed on the surfaces of intact and fractured tetrapods. By EDX analysis, the overall carbon content was determined to 96 at.%, next to 1 at.% oxygen, due to surface contamination, and 3 at.% sulfur. An equable dispersion of small dark spots and

scattered clusters, with diameters up of 50 nm, was observed between the CNTs. EFTEM images were recorded to examine the distribution of sulfur on the nanoscale. Figure 6.2 d, e depict respective images with the energy filter being adjusted to the sulfur K-edge at E = 165 eV[167] identifying the former described dark spots and clusters as sulfur, recognizable as bright intensities. In addition, comparative mappings of carbon (K-edge at E = 284 eV[167]; Figure 6.2 c) and sulfur (Figure 6.2 f) from the same region show similar patterns and confirm a successful attachment of sulfur to carbon.

## 6.2 Cycled sample

In a first approach, a pellet of sulfurized CNT tetrapods was installed into a battery set-up to function as cathode electrode and was charged and decharged once. After cycling, the sample shows a homogeneous morphology, but the outer part looks brighter than the inner part (Figure 6.3). Therefore, two specimens were extracted, one from the outer, one from the inner region.

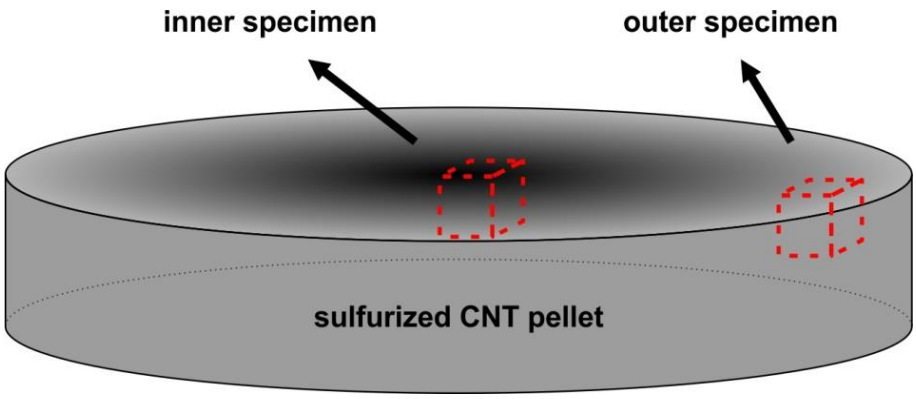


**Figure 6.3:** Schematic of a cycled cathode pellet with sketched positions of an exemplary inner and outer specimen site.

### Inner part

The basic morphology of the cycled sample did not change compared to its non-cycled state. TEM analysis reveal the existence of intact tetrapods (Figure 6.4 a) and tetrapod fragments (Figure 6.4 b) that suffered fracturing from preliminary grinding. Regarding single tetrapods, CNTs were examined (see Figure 6.4 c) to form a closed stable surface. According to their random orientation and generally complex structure[168], no distinct spots but rings corresponding to graphite were recognized, and marked by grey arcs in the corresponding SAED pattern (see Figure 6.4 c, inset).

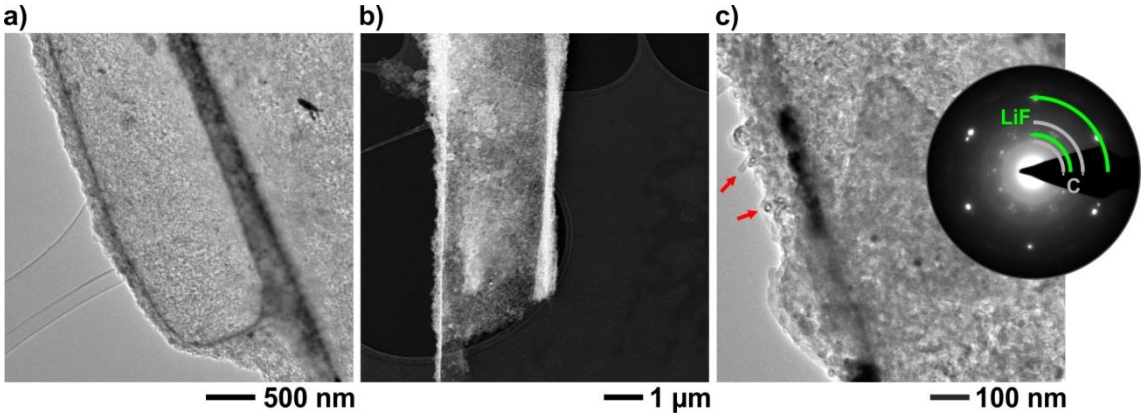


**Figure 6.4:** a) BF-TEM image of a CNT tetrapod's tip. b) DF-STEM images of a fractured CNT tetrapod arm. c) BF-TEM image of a tetrapod wall with recognizable CNTs marked by arrows and corresponding SAED pattern in the inset.

Next to the tetrapod's surface, scattered crystalline domains were found and, by SAED, identified as LiF. Most likely due to decomposition of the electrolyte $LiPF_6$, fluorine ions and, eventually, LiF remained. Phosphorous on the contrary was not detected at the inner region. Results of a first elemental analysis are presented in Figure 6.5.

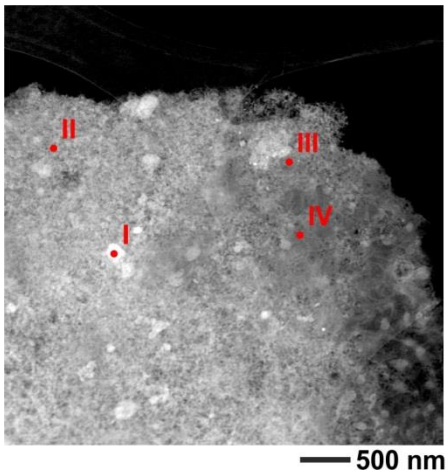


| Element | Concentration in at.% | | | |
|---|---|---|---|---|
| | I | II | III | IV |
| C | 41.78 | 76.89 | 82.19 | 84.50 |
| S | 34.73 | 5.46 | 2.97 | 4.19 |
| F | 14.52 | 4.22 | 2.11 | 3.18 |
| O | 6.66 | 12.47 | 11.45 | 7.22 |
| Si | 2.28 | 0.94 | 1.26 | 0.89 |

**Figure 6.5:** DF-STEM image of a CNT tetrapod wall from the inner region of the cathode. Elemental concentrations for the marked positions are listed in the table on the right.

The chemical composition was determined at four positions by EDX point analysis. Position **I** is located at a 200 nm-sized particle with higher intensity that was detected to exhibit an elevated concentration of sulfur and fluorine and a reduced concentration of oxygen (see table in Figure 6.5). Presumably due to a high fluorine level, oxidation of Li was suppressed, which has to be examined more closely. Positions **II – IV** show similar elemental ratios, particularly a high carbon content. Small concentrations of silicon are assigned to originate from the Si anode side through diffusion.

Additionally, the distribution of sulfur was examined by EFTEM presented in Figure 6.6. At two positions, the tip (Figure 6.6 a, c) and the middle-part of a tetrapod arm (Figure 6.6 b, d), BF-TEM images were recorded that display the structure's wall as a dark outline. 100 – 200 nm-sized darker domains are recognizable (Figure 6.6 b), located on top of the surface. EFTEM images adjusted to 165 eV, the K-edge of sulfur, depict a preferred concentration of sulfur on top of the surface in coincidence with the described small domains.

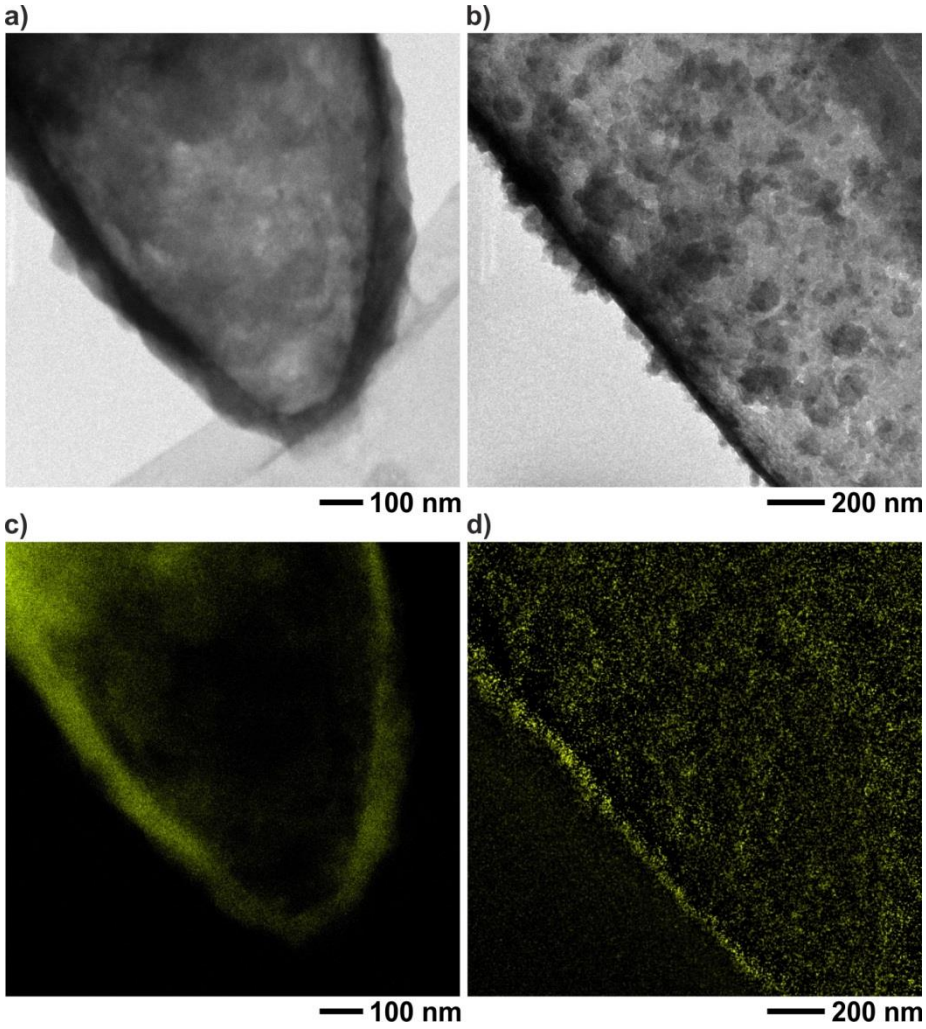


**Figure 6.6:** BF-TEM images of (a) tip and (b) part of an arm of a tetrapod and (c, d) corresponding false-colored EFTEM images of sulfur.

### Outer part

The outer region's microstructure was identified to be similar to the inner region. An excerpt of the entangled CNT network is presented in Figure 6.7 a. The corresponding SAED pattern features weak Debye-Scherrer rings[22] from graphitic CNTs and particularly defined reflections from LiF (compare Figure 6.4 c, inset).

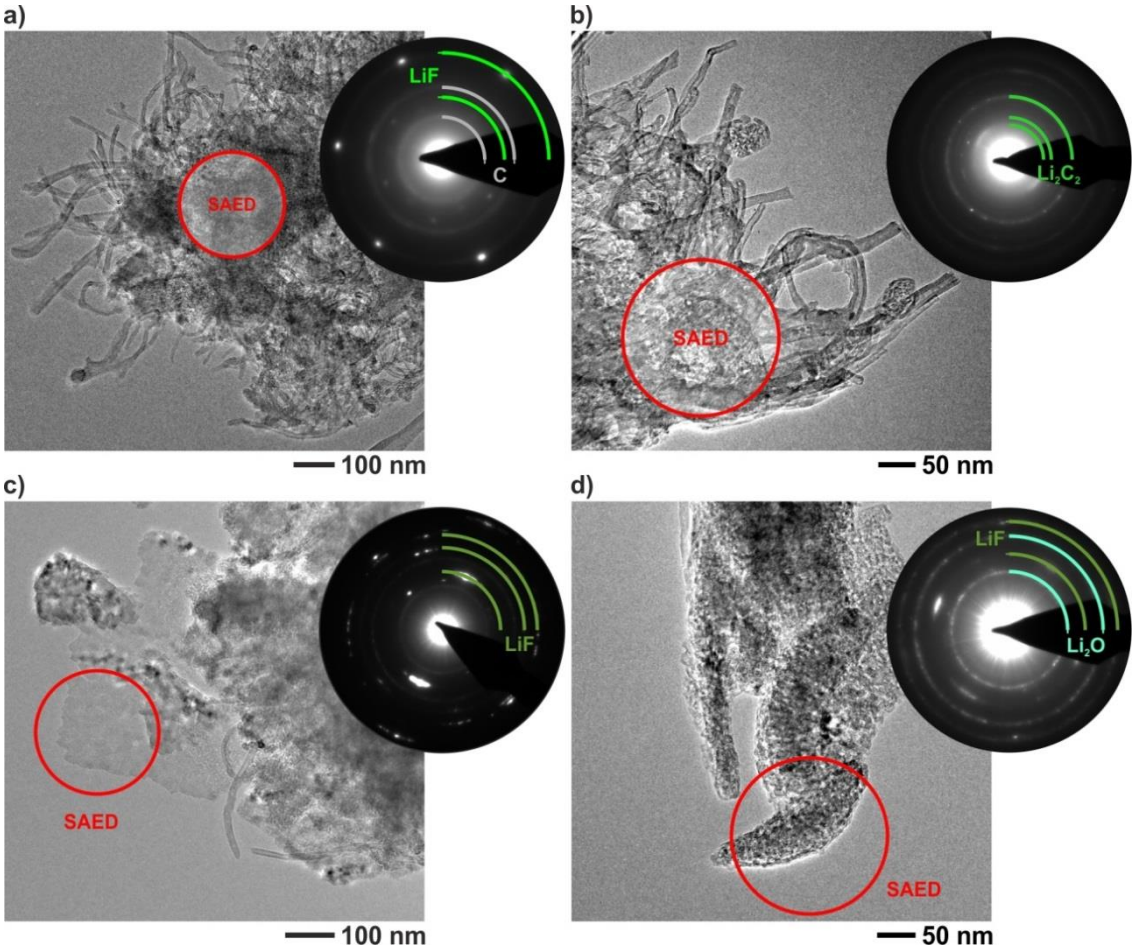


**Figure 6.7:** BF-TEM images from selected positions depicting the presence of (a) graphitic carbon and (b-d) different Li compounds. Corresponding SAED patterns from marked positions are contained in insets.

Unlike the crystalline anode, the determination of the cathode's SEI is not possible by standard imaging since its morphology does not noticeably change. By SAED and EDX data (see Table 6), the presence of LiF remaining from decomposition of the electrolyte is demonstrated forming thin probably crystalline lamellas (Figure 6.7 c).

**Table 6:** EDX results from Figure 6.7 a-d.

| Element | Concentration in at.% | | | |
|---|---|---|---|---|
| | Fig. 6.7 a | Fig. 6.7 b | Fig. 6.7 c | Fig. 6.7 d |
| **C** | 65.74 | 75.94 | 15.76 | 45.71 |
| **F** | 16.89 | 8.51 | 46.85 | 39.78 |
| **P** | 1.93 | 2.44 | 2.14 | 2.94 |
| **O** | 15.41 | 13.09 | 35.25 | 11.55 |

Other Li compounds, that were identified, comprise $Li_2C_2$ (Figure 6.7 b) and $Li_2O$ (Figure 6.7 d). In case of a reversible reaction, the formation of $Li_2C_2$ increases the capacity,

during cycling as it is already applied as battery material[169]. Concerning $Li_2O$, the concentration of oxygen was detected to be systematically higher at the outer region, which is explained by increased oxygen concentrations at the surface of the host material (CNTTs). The same holds for phosphorous that was only detected at the outer part. On the contrary, EDX analysis revealed a systematic absence of sulfur at the outer part of the cycled cathode pellet, that has yet to be explained and requires detailed analytical investigations (see Chapter 6.3).

## 6.3 Prospective development

Synthesized carbon-sulfur compounds were already demonstrated to represent a suitable cathode material applicable as counterpart to the Li-Si anode. First studies revealed promising properties (high capacity, versatile fabrication possibilities), but illustrated many problems concerning its application in a battery cathode. In the following, important scientific questions and prospective approaches to solve those are presented in order to further exploit the vast potential of sulfur-based cathodes.

### Sulfur concentration

Since first examinations of the cycled sulfur-containing carbon compound depicted a segregation of sulfur, a concentration gradient is proposed that has to be confirmed by more detailed investigations demanding for suited methods. A principally simple, but time-consuming procedure to examine an existing gradient, is the sequential analysis of multiple slices from defined positions; a basic outline is sketched in Figure 6.8.

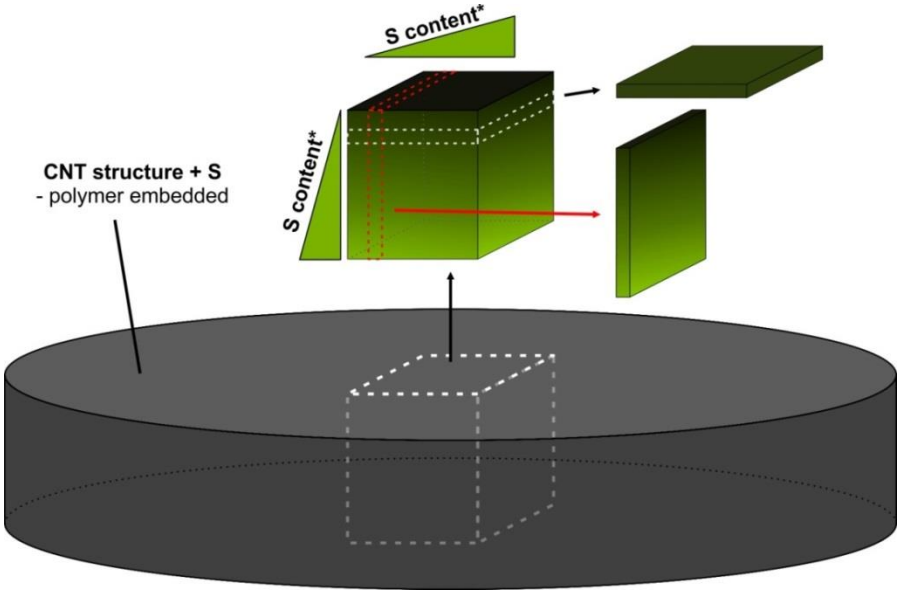


**Figure 6.8:** Schematic preparation of thin TEM-suited slices to investigate emerging sulfur gradients. First a small block is extracted from the polymer-embedded cathode pellet and further slices were cut in expedient orientations, that potentially present a concentration gradient.

Small blocks will be extracted from the polymer-embedded pellet, e.g. using a wire-saw and cut into thin electron-transparent slices by an ultramicrotome. Since the segregation of sulfur is expected to be caused by the polysulfide-shuttle effect, direction and intensity of the supposed gradient have to be examined in detail. This will be realized by the application of different cutting directions. Finally, the particular concentration and distribution of sulfur can be examined for each slice to stitch a 3-D model of the pellet. Additionally, TEM tomography can be applied for a regional determination of sulfur concentration.

Stability of the sulfur-carbon framework

The currently applied highly porous carbon structures are tailored via a template process where CNTs are used to cover tetrapodal ZnO frameworks. Suggested concepts for the proceeding project include a potential application of other suitable nanomaterials like graphene and boron nitride. Furthermore, different template structures could be applied to realize even higher porosities or heterogeneous porosities with a gradient from inner to outer region, e.g. to manipulate the shuttle-effect. Conceivable structures comprise, e.g. ZnO types providing different sizes and packing densities. Promising steps, in order to achieve higher mechanical stability of the resulting structures, are the application of a protective polymer layer and polymer additives during covering of the template.
A supplementary approach is the local fixation of sulfides during cycling of the cathode. Therefore, sulfur has to be bound effectively to carbon, and furthermore, remain fixed after charging. Already investigated concepts include the use of species, like $MoS_2$[170,171] or $MnO_2$[172], that entrap polysulfides and form surface-bound intermediates.

### 6.4 Summary

A carbon-sulfur cathode was developed by high-temperature sulfur infiltration of a CNT-framework structure. In a first test the desired stability of sulfur was successfully confirmed by EDX measurements showing identical sulfur concentrations before and after beam irradiation inside the TEM. But after only one charge/discharge cycle, the sample shows a systematic sulfur gradient detected by TEM analysis. The absence of sulfur at the outer part was probably detected due to electrochemically induced migration of sulfur towards the inner region of the cathode pellet. Sequential slicing is presented as a straight preparation procedure to provide a systematic examination of the sulfur distribution.
For an appropriate long-term performance an improved fixation of sulfur should be achieved to reduce the emerging concentration gradient and avoid partial passivation

of the cathode material. Here, a more detailed analysis of the chemical environment of sulfur and its binding mechanism in the CNT network is necessary. As for the anode, a SEI consisting of lithium and carbon compounds was observed that covers the CNT network.

# 7 Cu-In-S phases

Nanocrystalline Cu-In-S phases with distinguishable morphologies and uncommon microstructures through solvothermal synthesis were first produced at Kiel University by Dr. Enrique Quiroga-González at the Institute of Inorganic Chemistry, and subsequently reproduced at the Institute for Materials Science. Complementary to silicon and transition metal compounds discussed in Chapters 3-5, intended applications for Cu-In-S phases are energy conversion devices based on photovoltaic and photocatalytic processes. The well-known ternary compound $CuInS_2$ is a I-III-$VI_2$ chalcopyrite semiconductor already being used for photovoltaic applications termed as CI(G)S materials[173–176]. Belonging to the class of thin-film technologies, these compounds provide the fabrication of lighter (compared to conventional Si cells), flexible and partially transparent cells. Still, the market is governed by more efficient silicon-based devices and the share of thin-film CIS-based devices amounted only 1.3 % in 2016[177]. But through fundamental investigation and potential manipulation of the microstructures of Cu-In-S phases, more efficient and versatile CIS solar cells can be rendered possible.

Another prospective field of application is photocatalysis[178], where chemical reactions are supported by light incidence. Water splitting, as a particular type of photocatalysis, is a promising process to help covering the increasing demand for hydrogen, which is caused by the increasing use of fuel cell-powered vehicles. It is – among other techniques – a promising and clean energy source, where hydrogen conversion from water is obtained by exposing the respective catalyst material to sunlight without causing $CO_2$-producing combustion and radioactivity. According to the potential of the $O_2/H_2O$ couple, the minimum band gap for water splitting amounts 1.23 eV[179]. With a direct band gap of 1.55 eV at T = 300 K[180] $CuInS_2$ meets this requirement but provides a lower efficiency than already applied compounds, e.g. CdS[181] and ZnS. This can possibly be overcome by band-gap engineering or application of other Cu-In-S phases with less Cu content, e.g. CuInS, $CuIn_3S_5$ and $CuIn_5S_8$, which will not be considered in this work.

In previous works, different compounds of Cu-In-S system were investigated in terms of synthesis and structure and specified by the typical semiconductor formula $I\text{-}III_{2n}\text{-}VI_{3n+2}$[182,183]. Thus, the herein investigated products can be described best as stoichiometric mixtures of indium(III) sulfide and copper(I) sulfide(see Figure 7.1). In its stable, form $CuInS_2$ features a tetragonal chalcopyrite structure[184] trivially termed roquesite, with copper and indium forming a cubic close-packed lattice with sulfur atoms at the tetrahedral sites. For thin-film synthesis with a higher $In_2S_3$ concentration, Cu-In-S compounds were found to change from chalcopyrite to spinel structure since $In^{3+}$ ions preferentially occupy octahedral sites at higher indium concentration instead

of tetrahedral sites[183]. According to the phase diagram of $Cu_2S$ and $In_2S_3$, with $CuInS_2$ and $CuIn_5S_8$, only two equilibrium phases are known to exist. Still, many metastable phases can be synthesized, and in the following a chemical and crystallographic classification of obtained phases is presented as well as selected microstructural phenomena.

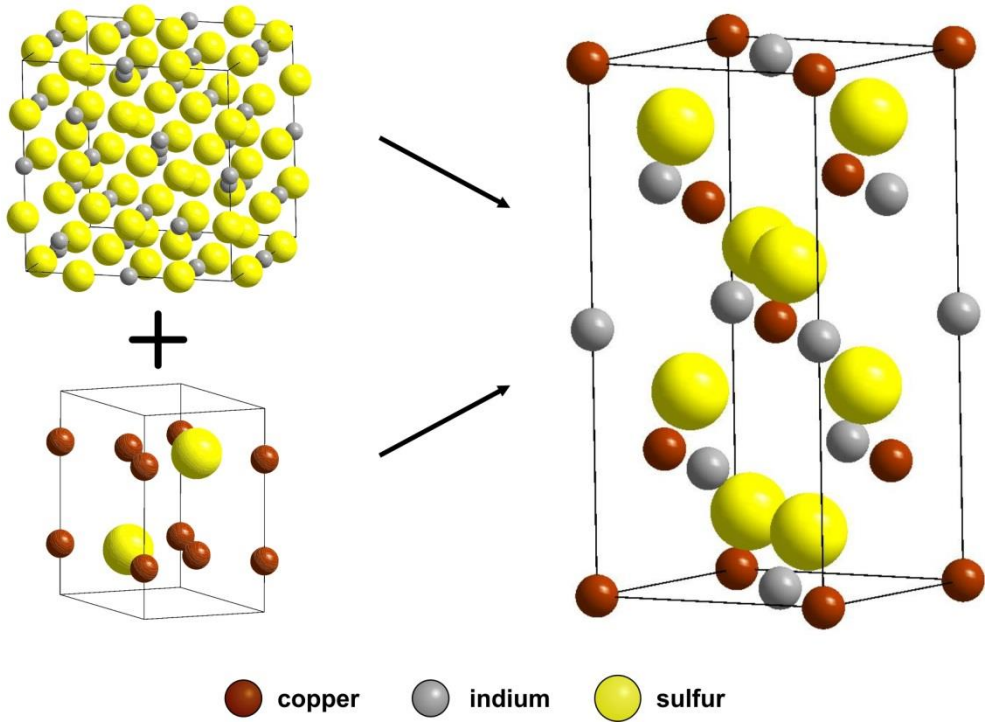


**Figure 7.1:** Indium(III) sulfide and copper(I) sulfide (left) eventually react to $CuInS_2$ (right).

### 7.1 Synthesis of Cu-In-S compounds

All compounds being investigated within this work were synthesized by a solvothermal approach (see Chapter 2.4.4), applying different temperatures and associated pressures. The three elements copper, indium and sulfur were weighted in the ratio 1.3:5:8 and put into a PTFE vessel. The particular proportions were determined by Dr. Quiroga-González in the course of his work on this topic. Sulfur was present as fine powder that easily sticks to any surface, especially to the PTFE vessel, due to electrostatic forces. Therefore, the actual amount of sulfur was a little less than weighted before. Indium and copper were present as small pellets. Additionally, ethylendiamine (EN) was added as a pressure-regulating agent. EN is a basic organic compound with the molecular formula $C_2H_4(NH_2)$. Determined through many experiments during prior synthesis by Dr. Quiroga-Gonzáles, the most suitable filling rate of approximately 15 vol% was applied. The PTFE vessels being used had a volume

of 50 ml so the amount of EN to achieve the desired pressure was calculated to be 7.5 ml.

The loaded steel vessel, with a pressure limit of 50 bar, was put in an oven at the adjusted temperature of 180 °C (/220 °C) and syntheses were preformed over 5 days. The products in the PTFE vessel were black to orange/red slurries. Cu-In-S compounds contained therein were extracted through filtering by passing a fine frit. For each sample the filtered product was rinsed with water, acetone and ethanol multiple times to remove remaining EN. Finally, a coarse powder of crystalline Cu-In-S particles was extracted to be investigated. For TEM investigation those particles were ground with an agate mortar and suspended in n-butanol. The suspension was dripped onto an aluminum TEM grid, not on a standard copper grid in order to prevent overlapping signals from sample and grid.

### 7.2 Phase characterization

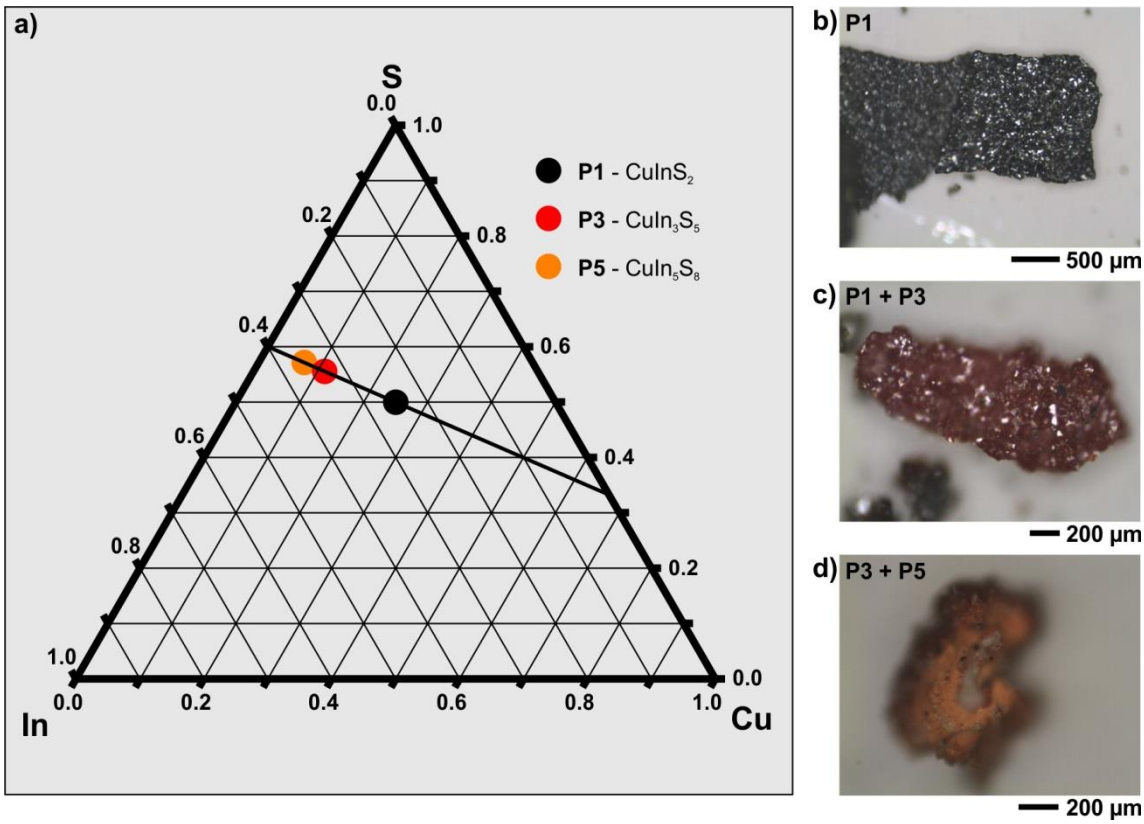


**Figure 7.2:** a) Ternary phase diagram for Cu-In-S with indicated herein discussed phases. b-d) Light microscope images depicting the typical colors of the phases black (P1), red (P3) and orange (P5). P3 and P5 were not found as macroscopic phases, but only as composites.

An initial examination of the particles was conducted with the help of a stereo light microscope of the type *Leica Polylite 88*, including a presorting according to particles' colors. Generally, three different phases were distinguished, termed P1 in black, P3 in

red and P5 in orange (Figure 7.2). A rough manual separation of the macroscopically different particles was conducted to simplify further handling and investigation. P1 particles were mainly found as single-phase particles that form a hard and brittle compound. P3 was partially identified as single phase, but also attached to P1 and P5. Similar to P1, the P3 and P1+P3 particles are brittle, but less hard. P5, the last compound, is found to exist exclusively next to P3. Respective particles are porous and very beam-sensitive.

### 7.2.1 $CuInS_2$ (P1)

#### Morphology and composition

Only a black phase, termed P1, was obtained from experiments performed at 180 °C. Its composition was determined by TEM-EDX to $Cu_{1.00}In_{1.18}S_{1.97}$, containing a slight excess of indium in form of $In_2S_3$ according to the defined mixture of $CuS_2$ and $In_2S_3$. Macroscopically, it looks similar to anthracite having a black color with many small shiny faces (see Figure 7.2 b). The morphology of the compound was analyzed in detail by SEM. As depicted in Figure 7.3 stacks of aligned round plates were determined with average diameters of 5 µm, and the thickness of the single plates was measured to be 100-200 nm. The phenomenon of stacking has not yet been reported for $CuInS_2$, but it was observed for $Cu_{1.94}S_{1.00}$ nanoplatelets produced from $CuInS_2$ nanoplatelets by cation exchange[185].

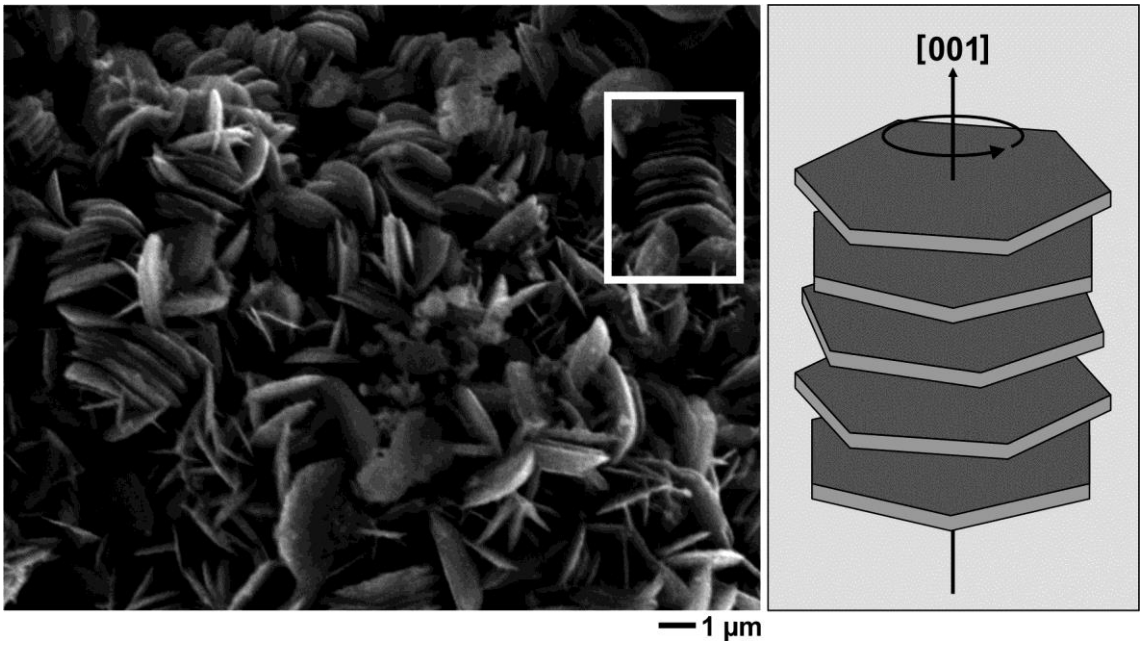


**Figure 7.3:** SEM image of P1 consisting of single and stacked plates. A schematic of a stack with indicated 6-fold symmetry demonstrates the common rotation axis towards which the plates preferentially align.

A comparable natural structure is nacre, a calcium carbonate modification. Still, iridescence[186], a typical phenomenon for many thin-layered materials ( e.g. nacre), was not observed for P1 probably due to the random arrangement of the plate stacks. Furthermore, the resulting large inner surface area effects strong light absorption letting the material appear very dark.

Reflections corresponding to the wurtzite modification of $CuInS_2$ were identified through TEM examination, presented in the following section. Furthermore, stacking and rotation of plates is assumed to occur along a preferred direction. Stacking can be described as a form of texturing, and since parallel plates share a common axis, this axis' reflex is expected to appear intensified in the SAED pattern, which is indeed observed for the (002) reflection (see Figure 7.6 c).

Microstructure

Thorough SAED and HRTEM investigations of powder samples were conducted to examine microstructural details of the phase P1. Figure 7.4 a depicts a part of a P1 plate that features a layered structure. The layers appear highly transparent and despite overlapping their edges are clearly visible. Their overall crystalline character is demonstrated by HRTEM (Figure 7.4 b) on a single layer that features a perfectly ordered wurtzite structure. The corresponding FFT pattern (Figure 7.4 c) as well as the SAED pattern (Figure 7.4 d) comply with the simulated ED pattern for the [101] zone axis (Figure 7.4 e) of hexagonal $CuInS_2$[187].

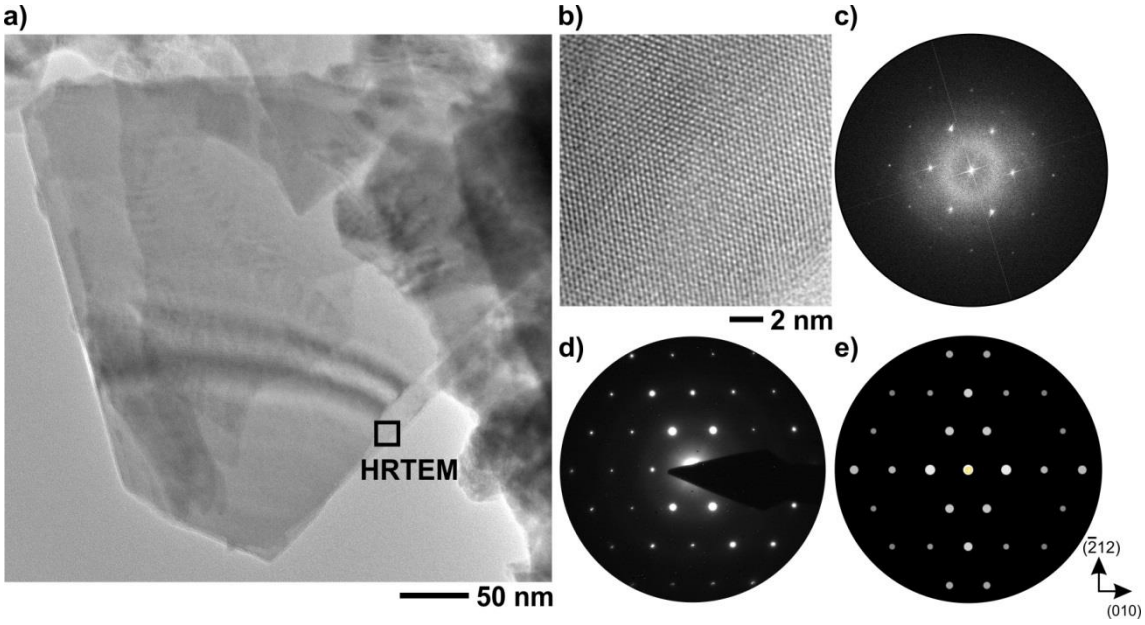


**Figure 7.4:** a) BF-TEM image of overlapping layers of P1. b) HRTEM micrograph from the region marked in (a), and (c) corresponding FFT pattern. d) SAED pattern from the particle shown in (a). e) Simulated ED pattern of the [101] direction for hexagonal $CuInS_2$.

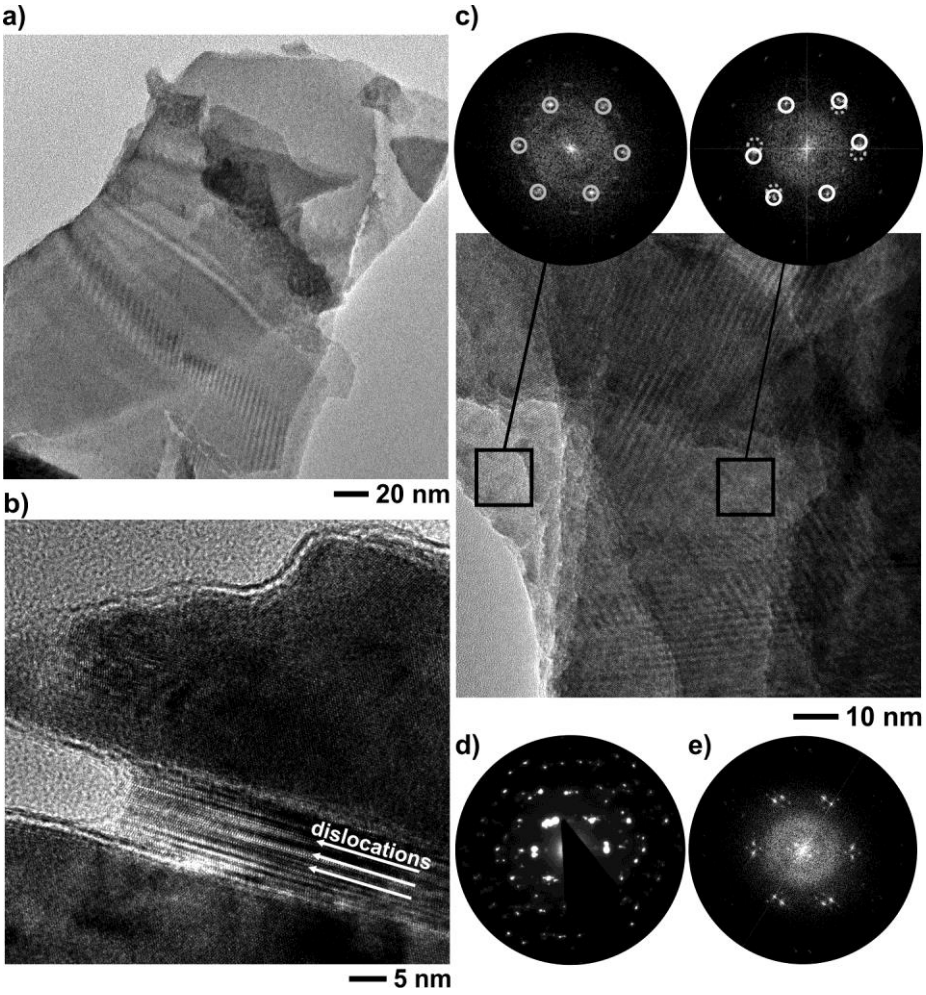


**Figure 7.5:** a) BF-TEM image of P1 showing beginning delamination at an edge. b) HRTEM micrograph of emerging dislocations marked by white arrows. c) Overlapping layers with slightly different lattice parameters (see FFT patterns in insets) noticeable by moiré patterns in the HRTEM micrograph. d) SAED pattern from the intact part of the particle containing two identical sets of reflections tilted against each other. e) FFT pattern from (c) with additional intensities from moiré effects.

The layered structure of P1 is investigated in more detail at edge-near positions that show starting delamination of individual layers (see Figure 7.5 a). Small fragments start to bend away from the surface to finally detach from the bulk structure, being ideal electron-transparent specimens. Furthermore, mismatches between thin layers of the bulk particles were determined, recognizable as moiré patterns (Figure 7.5 c). The corresponding FFT pattern (Figure 7.5 e) features multiple intensities in close proximity to the main spots, typical for moiré effects. By comparing two FFT patterns from neighboring regions (Figure 7.5 c, insets), a difference of their lattice parameters was measured. The assumed origin of the change of plane distances is a locally decreased Cu concentration and subsequent formation of defects, e.g. dislocations. As depicted in Figure 7.5 b, investigated dislocations share the crystallographic orientation [100]

towards surrounding crystalline fractions, which appears to be split by the actual dislocations. A systematic mechanism for dislocation formation is assumed representing a pre-stage for phase transformation to Cu-poorer phases accompanied by a slight lattice mismatch.
Furthermore, rotational mismatches between single or multiple layers were identified that cause multiple sets of reflections in the corresponding SAED pattern (see Figure 7.5 d). The phenomenon of rotational disorder is discussed in more detail for P3 (see Chapter 7.2.2) where its effect is more pronounced.

Superstructure reflections

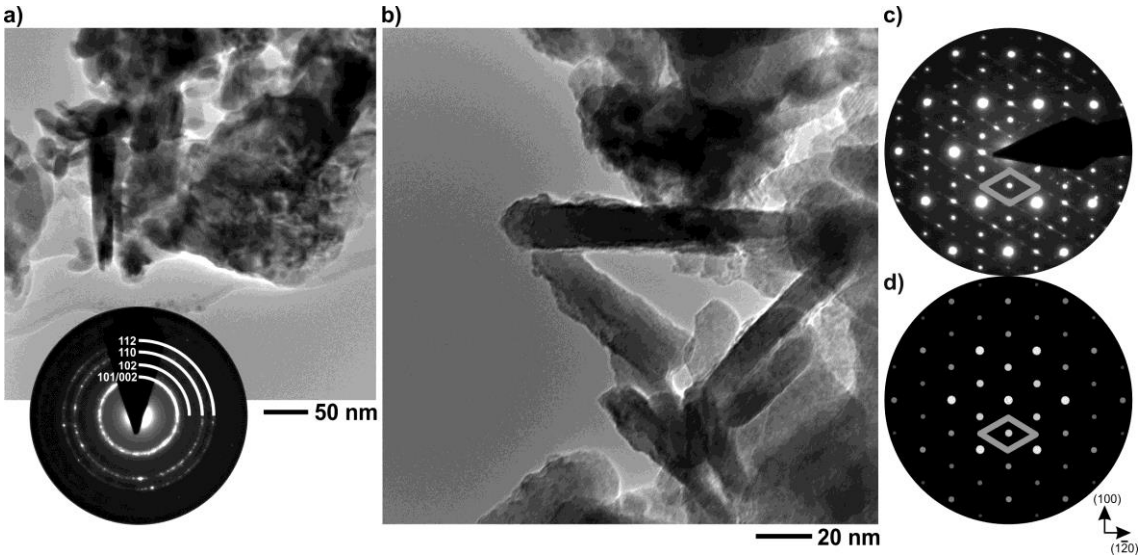


**Figure 7.6:** a) BF-TEM image of $CuInS_2$ needles with corresponding SAED pattern in the inset. b) Accumulation of needles at higher magnification. c) SAED pattern of a single needle featuring additional intensities and defined streaks marked by a grey rhombus. d) Simulated ED pattern of the [001] zone axis of $CuInS_2$.

The smallest $CuInS_2$ particles, that were yet observed are small needles with 20 nm in diameter and lengths of min. 50 nm (see Figure 7.6 b). According to EDX characterization, their composition is $Cu_{1.00}In_{1.22}S_{2.17}$. An SAED pattern from a larger region (Figure 7.6 a, inset) shows Debye-Scherrer rings due to the amount of randomly oriented crystalline nanodomains. All reflection rings can be assigned to the wurtzite structure of $CuInS_2$. When inserting a smaller diffraction aperture to focus on single needles, monocrystalline patterns are obtained. The SAED pattern in Figure 7.6 c generally corresponds to the simulated ED pattern (Figure 7.6 d) for the [001] zone axis of wurtzite-type $CuInS_2$. But next to the main reflections, additional intensities were detected. Existent on *h k/2 l* and equivalent positions, these additional spots are superimposed by fine, diffuse streaks forming rhombs that enclose the main

reflections. A symmetry reduction by doubling of the unit cell in *h* and *k* direction is considered as origin of the superstructure reflections.

### 7.2.2 $CuIn_3S_5$ (P3) and $CuIn_5S_8$ (P5)

At an elevated temperature of 220 °C red-orange products were obtained. Unlike the black P1 phase, P3 was not found in form of isolated particles, but connected to either P1 or P5. Still, a differentiation is simple due to their different morphologies and by performing EDX analyses prior to electron microscopic examination.

Morphology and composition

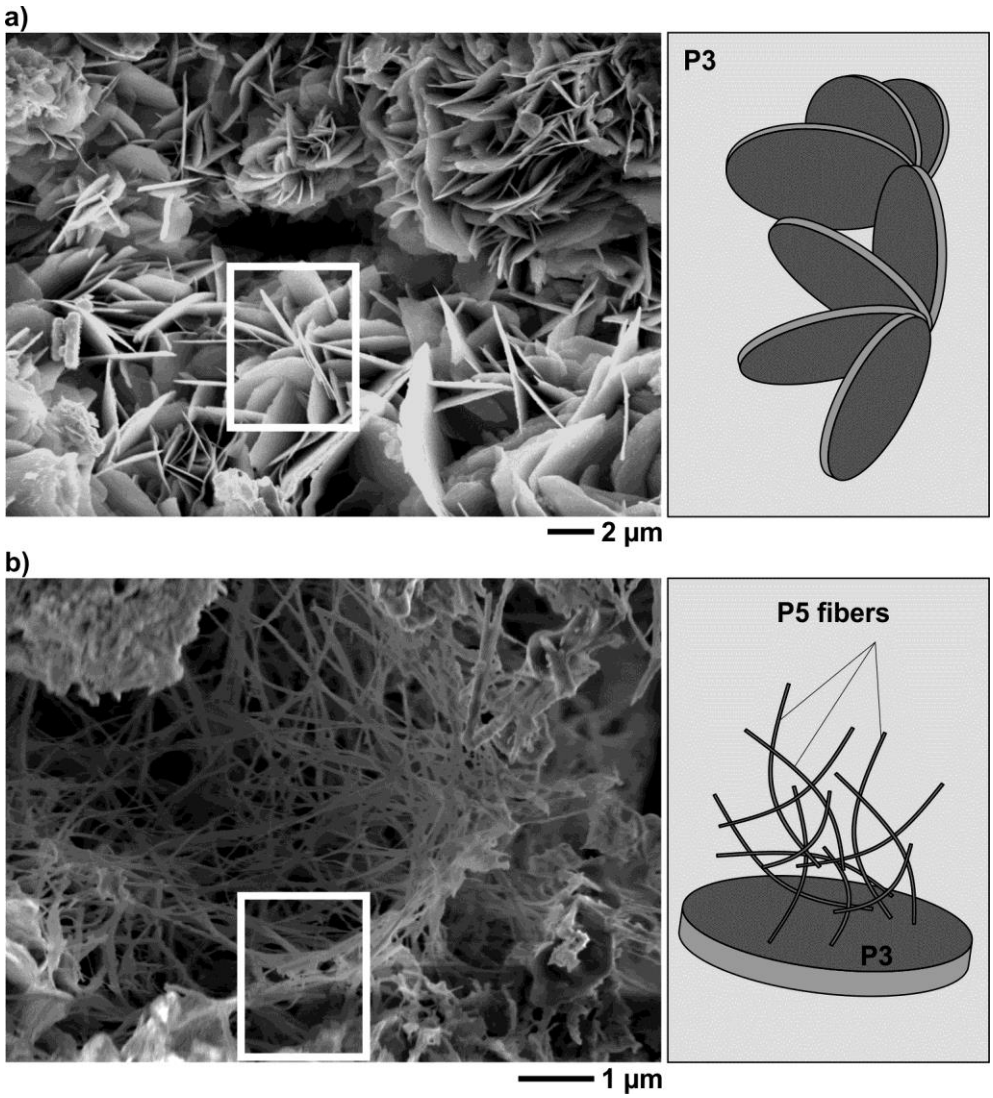


**Figure 7.7:** SEM images and schematics for the compounds P3 and P5. a) P3 consisting of petal-like organized thin plates with a common pivotal point. b) Thin P5 fibers with high aspect ratio and random orientation, exclusively found next to P3 particles.

Similar to P1, the P3-containing compound (P1+P3) features brilliant faces. For fractions identified as P3 a composition of $Cu_{1.00}In_{3.35}S_{5.38}$ was determined by TEM-EDX. The deviation from the composition of $CuIn_3S_5$, suggested by Dr. Quiroga-González, is explained by the coexistence of P3 and P5. The morphology of P3, presented in Figure 7.7 a, features a petal-like arrangement of sheets with about 5 µm in diameter, that appear noticeably thinner than the P1 plates. The respective schematic sketches the orientation of sheets that share a common pivotal point. Different from P1, no parallel stacking was observed. Close to P3 particles fine fibers with diameters of approximately 20 nm and lengths of up to more than 1 µm were found that were identified as P5. As shown in Figure 7.7 b those fibers appear to be flexible and randomly arranged. P5-containing particles feature an orange color and appear brighter due to the absence of P1. Throughout mechanical sample preparation P5 particles were determined to be were very brittle and porous. The composition for single fibers was determined to $Cu_{1.00}In_{4.99}S_{7.76}$ being very close to the composition of the stable phase $CuIn_5S_8$. Furthermore, fractions with lower copper content were found, e.g. compositions close to $CuIn_7S_{11}$, but they are not part of this work.

P3 microstructure

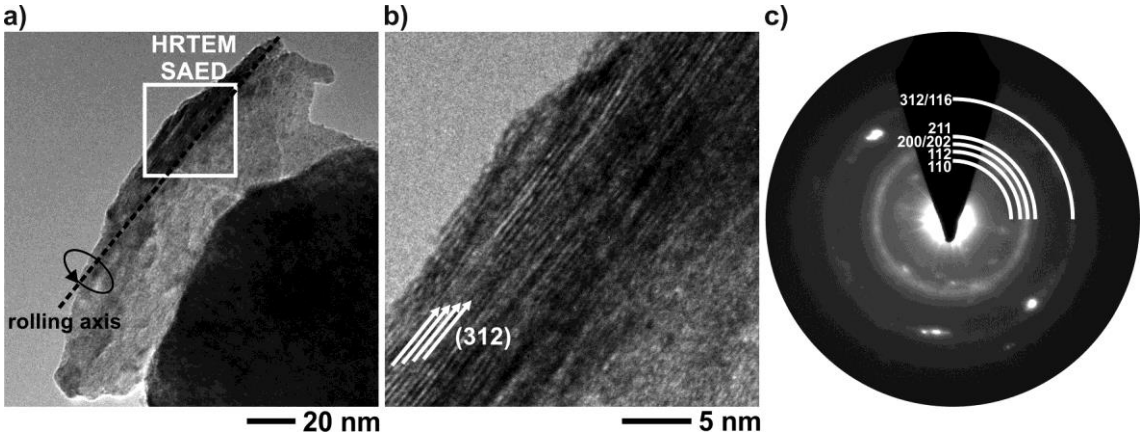


**Figure 7.8:** a) BF-TEM image of a P3 sheet with upper edge showing a tendency to roll up. b) HRTEM micrograph from region marked in (a) with apparent (312) planes and (c) corresponding SAED pattern.

A phenomenon barely recognized by SEM imaging is the tendency of P3-compound sheets to roll up. Figure 7.8 a depicts a few layers-thin particle that shows bending at its left edge appearing darker and pointing to the front. Due to tilting into an appropriate zone axis (Figure 7.8 b), (312) planes are visible at the bent region at higher magnification. Those planes are represented by two strong reflections in the corresponding SAED pattern (Figure 7.8 c). Nanocrystalline rings in the pattern can be assigned to $CuIn_3S_5$. According to the studies of Khemiri et al.[188], this copper-poor compound forms a chalcopyrite structure and originates from $CuInS_2$ through phase

transformation, starting at the surfaces accompanied by a segregation of $Cu_2S$[189]. $CuInS_2$, in its stable form (I-42d), and $CuIn_3S_5$ (P-42c) share related chalcopyrite structures with slightly differing lattice parameters. The composition at the particular area was determined to $Cu_{1.00}In_{1.95}S_{2.58}$, which indicates a coexistence of $CuInS_2$ and P3 due to the absence of other phases.

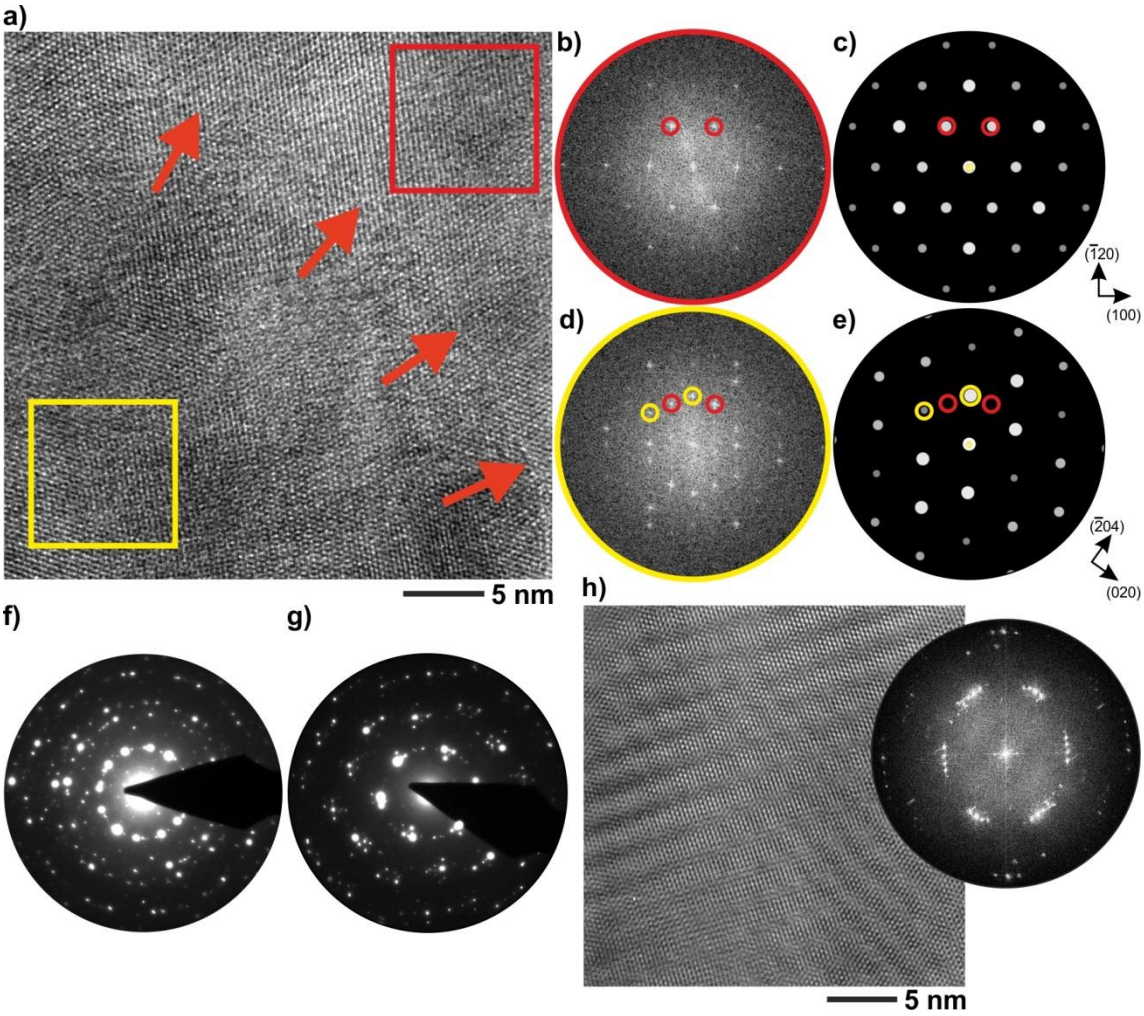


**Figure 7.9:** a) HRTEM micrograph of P1 featuring overlapping layers of different phases demonstrated by (b, d) corresponding calculated FFT patterns from marked regions that are compared to simulated ED patterns for (c) wurtzite-type $CuInS_2$ ([001] zone axis) respectively (e) chalcopyrite-type $CuInS_2$ ([201] zone axis). Recorded SAED patterns for a P1-P3 compound show (f) multiple sets of reflections typical for turbostratic disordering and further (g) oval-shaped patterns. h) HRTEM micrograph from a P1-P3 compound exhibiting a moiré pattern from superposition of different layers as well apparent as multiple oval-aligned reflections in the corresponding FFT pattern in the inset.

Throughout the applied synthesis, a transformation of metastable wurtzite- to chalcopyrite-type $CuInS_2$ is assumed prior to the formation of P3. For the herein investigated specimen the coexistence of those phases is demonstrated in Figure 7.9 a, that features structurally different overlapping layers. FFT patterns from those areas

(Figure 7.9 b, d) are compared to simulated patterns for hexagonal, respectively tetragonal $CuInS_2$ (Figure 7.9 c, e). Frequently, overlapping domains were recognized. The corresponding SAED pattern (Figure 7.9 f) and FFT pattern (Figure 7.9 h) predominantly contain four sets of reflections that exhibit systematic mismatch angles. This phenomenon, typical for turbostratic disordering, arises from coincidental correlated and uncorrelated stacking and was already reported, e.g. in earlier findings on montmorillonite[190]. In-plane defects and layer misalignments emerge in the progress of phase transformation, that are visualized by complex superposition phenomena in this case an oval-shaped SAED pattern (see Figure 7.9 g).

P5 microstructure

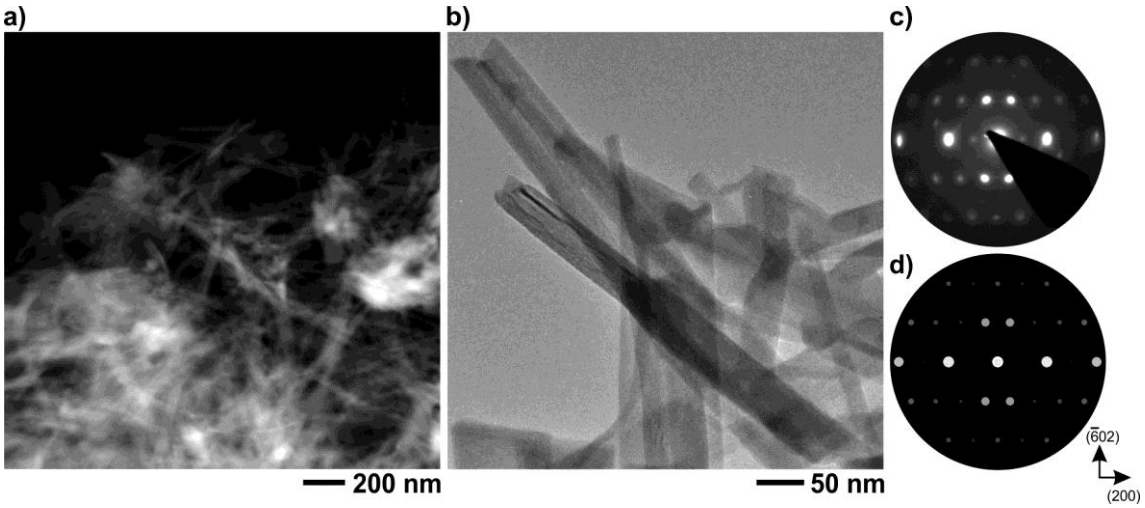


**Figure 7.10:** a) DF-STEM image and (b) higher magnified BF-TEM image of randomly oriented P5 fibers. c) SAED (d) simulated ED pattern from P5 along the [103] zone axis.

Thin unordered fibers (Figure 7.10 a, b) were identified, that are very beam-sensitive. Knock-on damage by the incident electron beam leads to proceeding decomposition of the specimen, inhibiting the recording of images of acceptable quality at higher magnifications. The SAED pattern depicted in Figure 7.10 c corresponds to the [103] zone axis of cubic $CuIn_5S_8$ (Figure 7.10 d) in agreement with the presented EDX data. But next to the main reflections, additional reflections as well as diffuse scattering were observed being typical for (locally) disordered structures[191]. In the case of P3, a predominant $CuIn_5S_8$ phase was found, that appears to be locally disordered, according to EDX data, this is caused by Cu-poorer fractions.

### 7.3 Photocatalytic activity

Four samples were tested for their photocatalytic production of $H_2$ from water. Two of them consist mainly of P1, the other two are mainly P3 or P5, respectively. Catalytic

experiments were performed with $Na_2S{\cdot}8\ H_2O$ and $Na_2SO_3$ as sacrificial reagents and Pt as co-catalyst. A 250 W metal-halide lamp was used as an energy source, providing light in the range of 250-600 nm at an intensity of 190000 Lux. During irradiation, the vessel was cooled below 40 °C to avoid evaporation of water. For quantification of produced $H_2$ the gas chromatograph *Shimadzu GC-14A* was used, with Ar as carrier gas.

Figure 7.11 shows a graph with data recorded by Dr. Quiroga-González that compares the time-dependent amount of produced $H_2$ for different samples, which mainly contained the compounds in captions. Generally, Cu-poor compounds reveal increased $H_2$ evolution. For P5 a rate of about 2000 $\mu molh^{-1}g^{-1}$ was measured, which is comparable to $rGO\text{-}Zn_{0.8}Cd_{0.2}S$[192] with 1.824 $\mu molh^{-1}g^{-1}$. For P3 it was about 400 $\mu molh^{-1}g^{-1}$ being comparable to $(AgIn)_xZn_{2(1-x)}S_2$[193] with 283 $\mu molh^{-1}g^{-1}$. But according to the fitted plot for P3, a decreasing slope indicates a reduction of the evolution rate to nearly zero after 60 min. For P1, two disparate curves with values lower than those for P3 and P5 are presented; one with steady $H_2$ evolution and the other with initially increasing evolution rate until, after 40 min, it decreases to become negative. Since both samples were basically P1 but still contained fractions of P3 and P5, it was concluded that the actual composition strongly influences the catalytic properties and has to be investigated in more detail.

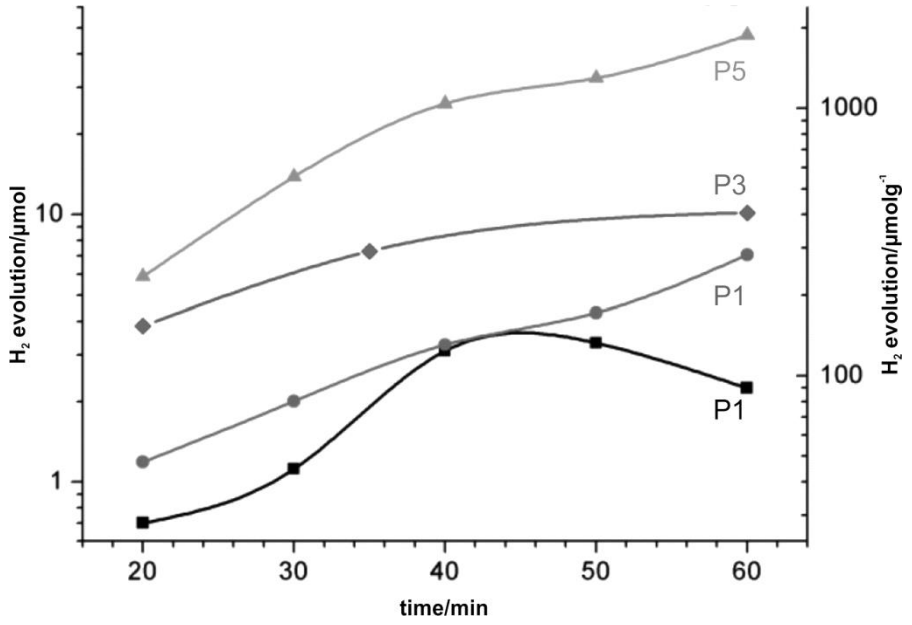


**Figure 7.11:** Comparison of $H_2$ evolution rates for different Cu-In-S phases.

## 7.4 Summary

New uncommon phases in the system Cu-In-S especially wurtzite-type $CuInS_2$ and $CuIn_3S_5$ are presented. The occurrence of respective phases is shown to depend on the

synthesis temperature, and their transitions are mostly inchoate. Obtained reaction products were separated macroscopically due to different colors ranging from orange to black. Still, many particles consist of different compositions coexisting next to each other.

Comparing the morphologies of obtained phases, a decreased ordering was observed with decreasing Cu content. The metastable wurtzite-type $CuInS_2$ phase, termed P1, was found to aggregate self-organized stacks of µm-sized plates. For P3 crystalline sheets were also observed but less symmetrically arranged. Furthermore, bending and detachment of layers was noted as well as a gradual transition to Cu-poorer phases. P5 phase fibers were detected, exclusively accompanied by P3 and determined to be very beam-sensitive due to their thin diameter and partially disordered structure.

Different from the two stable compounds in the Cu-In-S system (chalcopyrite-type $CuInS_2$ and $CuIn_5S_8$), all metastable compounds feature peculiar structural defects with different grades of ordering that are potentially viable, e.g. for band-gap engineering. Those have to be investigated in more detail. Especially the microstructure of the volatile P5 phase is rarely understood, and further more sensitive analytical techniques are necessary to avoid sample degradation. Experiments on photocatalytic activity revealed comparably good $H_2$ evolution, especially for the Cu-poor phase P5. Still, a stable production was not achieved, which is explained by the yet unstable phases demonstrated by TEM experiments.

# 8 Conclusion and Outlook

Within this dissertation, different potential materials for battery application and photocatalysis were analyzed and evaluated. Individual preparation procedures were developed and applied in order to elucidate highly sensitive compounds by TEM and SEM.

An alternative for storing electrical energy in batteries is the generation of $H_2$ for fuel-cells. Cu-In-S compounds were synthesized and shown to be usable as photocatalytic material. Especially Cu-poor phases demonstrated to provide high photocatalytic activity. Different composition-dependent microstructural characteristics were presented that are potentially beneficial for band-gap engineering. An interesting point for continuative works is the determination of respective correlations in order to develop a good photocatalyst.

The development of innovative high-performance batteries was focused on in the field of reversible energy storage. For an economic application not only higher capacities, but also improved durability and sustainability are required.
Carbon-enhanced transition metal compounds were developed as conversion-type cathodes, that include widely available metals to substitute, e.g. cobalt. Their microstructural evolution through cycling from spinel structure nanoparticles to agglomerated microcrystalline or amorphous mixed-oxide particles was demonstrated by HRTEM and SAED analysis. An increased long-time performance of the batteries by integration of carbon was shown. With up to 900 $mAhg^{-1}$ ($NiFe_2O_4$, after 40 cycles) adequate capacities were achieved, compared to currently available batteries that supply about 350 $mAhg^{-1}$. Capacity losses mainly occur in the first cycles through degradation of the spinel structure and become smaller during further cycling. For a reasonable application in commercial batteries the performance after a larger number of cycles as well as the impact of elevated temperatures has to be examined. Further investigations of the emerging microstructure are necessary to predict the advantage of mixed metal oxides. Especially the cycling characteristics of manganese offer many problems, e.g. irreversible losses and segregation.

Developed from the field of semiconductor technologies, the novel concept of ordered Si microwires as anode material exhibits large capacities of 3000 $mAhg^{-1}$. Due to the special morphology of the Si structure, a reversible transformation from crystalline silicon to amorphous Li-Si through lithiation was achieved. Still, the structural dimensions were disadvantageous for a direct TEM analysis, but it was rendered possible to obtain isolated wires by developing suited preparation methods. In case of cycled samples, due to their air- and moisture-sensitive SEI, a procedure for handling at inert gas atmosphere was elaborated. Failure mechanisms including stress-induced

fracturing and altering of the SEI were illustrated to occur especially during the first cycles and at higher charging rates. By applying a lower charging rate for the first cycles, the formation of a stable SEI was achieved that reduces degradation during further cycling. Different trials on tuning the electrolyte were performed with best results after adding PC whose transition leads to an increased elasticity of the formed SEI. Thus, charging rates could be increased to 2 C, meaning complete charging in 30 min. In the course of the herein presented cycling experiments a model for reversible cycling of Si microwires was set up that describes the interaction of SEI, electrolyte and amorphous as well as crystalline Si. Important for intended practical applications of any electrode is the impact of elevated temperatures. Coating with BN was demonstrated for this particular anode type to improve its stability at temperatures up to 80 °C. Through continuous improvements, it is assumed to finally obtain a temperature-stable and fast-rechargeable anode type for high performance batteries being applicable in, e.g. vehicles or stand-alone devices.

As recent development, a carbon-sulfur compound was presented as potential material for complementary cathodes, which is currently being developed in Kiel. Although the handling of sulfur in a TEM is potentially harmful to its components, it was managed without adverse effects. First experiments were successfully performed and revealed a successful integration of sulfur into a porous carbon framework with the aim to exploit the large potential of sulfur as electrode material, but also indicated emerging concentration gradients for sulfur during cycling. At the present stage it is intended to develop a procedure to synthesize a consistent compound that does not suffer from decomposition and partial segregation during cycling. Following steps schedule to match the carbon-sulfur cathode with the Si-microwire anode and tailor its cycling performance in order to develop a viable and competitive battery.

## Abbreviations

| | | |
|---|---|---|
| BCC | - | Body-centered cubic |
| BF | - | Bright-field |
| C | - | Charging rate |
| DF | - | Dark-field |
| ED | - | Electron diffraction |
| EDX | - | Energy-dispersive X-ray spectroscopy |
| EELS | - | Electron energy loss spectroscopy |
| EFTEM | - | Energy-filtered TEM |
| FFT | - | Fast Fourier transform |
| FIB | - | Focused ion beam |
| HAADF | - | High-angle annular DF |
| HRTEM | - | High-resolution TEM |
| LIB | - | Lithium-ion battery |
| PED | | Precession ED |
| SAED | - | Selected area ED |
| SEI | - | Solid electrolyte interface |
| SEM | - | Scanning electron microscopy |
| STEM | - | Scanning TEM |
| TEM | - | Transmission electron microscopy |
| XRD | - | X-ray diffraction |

## Bibliography


1. The Columbia Dry Cell Battery. (2005).
2. Whittingham, M. S. Lithium Batteries and Cathode Materials. *Chem. Rev.* **104**, 4271–4302 (2004).
3. *Lithium Batteries*. (Springer US, 2003). doi:10.1007/978-0-387-92675-9
4. Mizushima, K., Jones, P. C., Wiseman, P. J. & Goodenough, J. B. LixCoO2 (0<x<-1): A new cathode material for batteries of high energy density. *Mater. Res. Bull.* **15**, 783–789 (1980).
5. Sony History. Available at: https://www.sony.net/SonyInfo/CorporateInfo/History/SonyHistory/2-13.html.
6. Goodenough, J. B. & Kim, Y. Challenges for Rechargeable Li Batteries. *Chem. Mater.* **22**, 587–603 (2010).
7. Dahn, J. R., Zheng, T., Liu, Y. & Xue, J. S. Mechanisms for Lithium Insertion in Carbonaceous Materials. *Science* **270**, 590–593 (1995).
8. Stevens, D. A. & Dahn, J. R. High Capacity Anode Materials for Rechargeable Sodium-Ion Batteries. *J. Electrochem. Soc.* **147**, 1271 (2000).
9. *E-mobility Roadmap for the EU battery industry*. (The European Association for Advanced Rechargeable Batteries, 2013).
10. *Vehicle Battery Safety Roadmap Guidance*. (National Renewable Energy Laboratory, 2012).
11. *Technology Roadmap Energy Storage for Electric Mobility 2030*. (Fraunhofer Institute for Systems and Innovation, 2012).
12. Motorola Milestones. Available at: https://www.motorola.com/us/about/motorola-history-milestones.
13. *Ericsson Mobility Report November 2017*. (Ericsson AB, 2017).
14. Tesla Model S 90D EPA Rating Tops 300 Miles Highway. Available at: https://www.teslarati.com/new-tesla-model-s-90d-gets-300-mile-epa-rating/.
15. Battery and charging. Available at: https://www.renault.co.uk/vehicles/new-vehicles/zoe-250/battery-and-charging.html.
16. Model S/Range. Available at: https://www.tesla.com/models.
17. Tesla Model S Weight Distribution. Available at: https://www.teslarati.com/tesla-model-s-weight.
18. Samsung confirms battery faults as cause of Note 7 fires. Available at: http://www.bbc.com/news/business-38714461.

19. Ohnsman, A. & Greiling Keane, A. Tesla's Third Model S Fire Brings Call for U.S. Inquiry. Available at: https://www.bloomberg.com/news/articles/2013-11-07/tesla-s-third-model-s-fire-brings-call-for-u-s-inquiry.

20. Holmes, F. *The World's Cobalt Supply Is In Jeopardy*. (Forbes, 2018).

21. Kobayakawa, K., Teranishi, A., Tsurumaki, T., Sato, Y. & Fujishima, A. Photocatalytic activity of CuInS2 and CuIn5S8. *Electrochimica Acta* **37**, 465–467 (1992).

22. Williams, D. B. & Carter, C. B. *Transmission electron microscopy: a textbook for materials science*. (Springer, 2008).

23. Fultz, B. & Howe, J. M. *Transmission electron microscopy and diffractometry of materials*. (Springer, 2013).

24. Reimer, L. & Kohl, H. *Transmission electron microscopy: physics of image formation*. (Springer, 2008).

25. *Transmission electron energy loss spectrometry in materials science and the EELS atlas*. (Wiley, 2004).

26. Schürmann, U., Duppel, V., Buller, S., Bensch, W. & Kienle, L. Precession Electron Diffraction - a versatile tool for the characterization of Phase Change Materials. *Cryst. Res. Technol.* **46**, 561–568 (2011).

27. Balakrishnan, P. G., Ramesh, R. & Prem Kumar, T. Safety mechanisms in lithium-ion batteries. *J. Power Sources* **155**, 401–414 (2006).

28. Wang, Q. *et al.* Thermal runaway caused fire and explosion of lithium ion battery. *J. Power Sources* **208**, 210–224 (2012).

29. Askeland, D. R., Fulay, P. P. & Wright, W. J. *The science and engineering of materials*. (Cengage Learning, 2011).

30. Engler, O. & Randle, V. *Introduction to texture analysis: macrotexture, microtexture, and orientation mapping*. (CRC Press, 2010).

31. Mayer, J., Giannuzzi, L. A., Kamino, T. & Michael, J. TEM Sample Preparation and FIB-Induced Damage. *MRS Bull.* **32**, 400–407 (2007).

32. Furneaux, R. C., Thompson, G. E. & Wood, G. C. The application of ultramicrotomy to the electronoptical examination of surface films on aluminium. *Corros. Sci.* **18**, 853–881 (1978).

33. Kvien, I., Tanem, B. S. & Oksman, K. Characterization of Cellulose Whiskers and Their Nanocomposites by Atomic Force and Electron Microscopy. *Biomacromolecules* **6**, 3160–3165 (2005).

34. Hölken, I. *et al.* Complex shaped ZnO nano- and microstructure based polymer composites: mechanically stable and environmentally friendly coatings for potential antifouling applications. *Phys Chem Chem Phys* **18**, 7114–7123 (2016).

35. Li, C. *et al.* Thiol–isocyanate click reaction in a Pickering emulsion: a rapid and efficient route to encapsulation of healing agents. *Polym. Chem.* **6**, 7100–7111 (2015).

36. Li, Y. *et al.* $MoS_2$ Nanoparticles Grown on Graphene: An Advanced Catalyst for the Hydrogen Evolution Reaction. *J. Am. Chem. Soc.* **133**, 7296–7299 (2011).

37. Patzke, G. R., Krumeich, F. & Nesper, R. Oxidic Nanotubes and Nanorods—Anisotropic Modules for a Future Nanotechnology. *Angew. Chem. Int. Ed.* **41**, 2446–2461 (2002).

38. Quiroga-González, E., Ossei-Wusu, E., Carstensen, J. & Föll, H. How to Make Optimized Arrays of Si Wires Suitable as Superior Anode for Li-Ion Batteries. *J. Electrochem. Soc.* **158**, E119 (2011).

39. Quiroga-González, E., Carstensen, J. & Föll, H. Good cycling performance of high-density arrays of Si microwires as anodes for Li ion batteries. *Electrochimica Acta* **101**, 93–98 (2013).

40. Nöhren, S., Quiroga-González, E., Carstensen, J. & Föll, H. Electrochemical Fabrication and Characterization of Silicon Microwire Anodes for Li Ion Batteries. *J. Electrochem. Soc.* **163**, A373–A379 (2016).

41. Mukhopadhyay, A. & Sheldon, B. W. Deformation and stress in electrode materials for Li-ion batteries. *Prog. Mater. Sci.* **63**, 58–116 (2014).

42. eneloop lite batteries. Available at: http://www.panasonic-eneloop.eu/en/products-lite.

43. Energizer Recharge® Rechargeable Batteries. Available at: http://www.energizer.com/batteries/energizer-rechargeable-batteries.

44. Manhart, A., Riewe, T. & Brommer, E. *PROSA Smartphones*. (Öko-Institut e.V.).

45. Xu, B., Oudalov, A., Ulbig, A., Andersson, G. & Kirschen, D. S. Modeling of Lithium-Ion Battery Degradation for Cell Life Assessment. *IEEE Trans. Smart Grid* **9**, 1131–1140 (2018).

46. Broussely, M. *et al.* Main aging mechanisms in Li ion batteries. *J. Power Sources* **146**, 90–96 (2005).

47. *Handbook of batteries*. (McGraw-Hill, 2002).

48. Nadler, M. R. & Kempier, C. P. Crystallographic Data 186. Lithium. *Anal. Chem.* **31**, 2109–2109 (1959).

49. Krebs, R. E. The history and use of our earth's chemical elements: a reference guide. (2006).

50. Martin, R. *Quest to Mine Seawater for Lithium Advances*. (MIT, 2015).

51. *Lithium*. (U.S. Geological Survey, 2018).

52. Cipriani, A., Hawton, K., Stockton, S. & Geddes, J. R. Lithium in the prevention of suicide in mood disorders: updated systematic review and meta-analysis. *BMJ* **346**, f3646–f3646 (2013).

53. Bowden, C. L. A Randomized, Placebo-Controlled 12-Month Trial of Divalproex and Lithium in Treatment of Outpatients With Bipolar I Disorder. *Arch. Gen. Psychiatry* **57**, 481 (2000).

54. US to decide how to make its tritium. *New Sci.* **121**, 36 (1989).

55. Brooker, M. H. & Bates, J. B. Raman and Infrared Spectral Studies of Anhydrous Li $_2$ CO $_3$ and Na $_2$ CO $_3$. *J. Chem. Phys.* **54**, 4788–4796 (1971).

56. Besenhard, J. O. & Eichinger, G. High energy density lithium cells. *J. Electroanal. Chem. Interfacial Electrochem.* **68**, 1–18 (1976).

57. Basu, S. *et al.* Synthesis and properties of lithium-graphite intercalation compounds. *Mater. Sci. Eng.* **38**, 275–283 (1979).

58. Brown, G. C. & Mussett, A. E. *The inaccessible earth*. (Allen & Unwin, 1981).

59. Straumanis, M. E. & Aka, E. Z. Lattice Parameters, Coefficients of Thermal Expansion, and Atomic Weights of Purest Silicon and Germanium. *J. Appl. Phys.* **23**, 330–334 (1952).

60. Müller, G. *Crystal growth from the melt*. (Springer, 1988).

61. Robles-Hernandez, F., Herrera Ramírez, J. M., Mackay, R. & Springer International Publishing AG. *Al-Si Alloys Automotive, Aeronautical, and Aerospace Applications*. (2017).

62. *Handbuch Maschinenbau: Grundlagen und Anwendungen der Maschinenbau-Technik ; mit 405 Tabellen*. (Springer Vieweg, 2013).

63. Zeilinger, M., Kurylyshyn, I. M., Häussermann, U. & Fässler, T. F. Revision of the Li–Si Phase Diagram: Discovery and Single-Crystal X-ray Structure Determination of the High-Temperature Phase Li $_{4.11}$ Si. *Chem. Mater.* **25**, 4623–4632 (2013).

64. Li, J. & Dahn, J. R. An In Situ X-Ray Diffraction Study of the Reaction of Li with Crystalline Si. *J. Electrochem. Soc.* **154**, A156 (2007).

65. Frank, U., Müller, W. & Schäfer, H. Zur Kenntnis der Phase Li13Si4. *Z. Fuer Naturforschung B J. Chem. Sci.* **30 b**, 10–13 (1975).

66. Obrovac, M. N. & Christensen, L. Structural Changes in Silicon Anodes during Lithium Insertion/Extraction. *Electrochem. Solid-State Lett.* **7**, A93 (2004).

67. Hatchard, T. D. & Dahn, J. R. In Situ XRD and Electrochemical Study of the Reaction of Lithium with Amorphous Silicon. *J. Electrochem. Soc.* **151**, A838 (2004).

68. Zeilinger, M. *et al.* Alkali Metals Extraction Reactions with the Silicides $Li_{15}Si_4$ and $Li_3NaSi_6$ : Amorphous Si *versus allo* -Si. *Chem. Mater.* **26**, 6603–6612 (2014).

69. Thomas, D. *et al.* The heat capacity and entropy of the lithium silicides Li17Si4 and Li16.42Si4 in the temperature range from (2 to 873)K. *J. Chem. Thermodyn.* **85**, 178–190 (2015).

70. Axel, H., Schäfer, H. & Weiss, A. Zur Kenntnis der Phase Li22Si5. *Z. Fuer Naturforschung Teil B Anorg. Chem. Org. Chem. Biochem. Biophys. Biol.* **21 b**, 115–117 (1966).

71. Kubota, Y., Escaño, M. C. S., Nakanishi, H. & Kasai, H. Crystal and electronic structure of Li15Si4. *J. Appl. Phys.* **102**, 053704 (2007).

72. Lee, S. W., McDowell, M. T., Choi, J. W. & Cui, Y. Anomalous Shape Changes of Silicon Nanopillars by Electrochemical Lithiation. *Nano Lett.* **11**, 3034–3039 (2011).

73. Xianhua, H., Shejun, H., Qiang, R. & Zhiwen, Z. The Roles of Intermediate Phases of Li-Si Alloy as Anode Materials for Lithium-Ion Batteries. *Rare Met. Mater. Eng.* **39**, 2079–2083 (2010).

74. Misra, S. *et al.* In Situ X-ray Diffraction Studies of (De)lithiation Mechanism in Silicon Nanowire Anodes. *ACS Nano* **6**, 5465–5473 (2012).

75. Smetana, V., Kienle, L., Duppel, V. & Simon, A. Synthesis, Crystal Structure, and TEM Analysis of $Sr_{19}Li_{44}$ and $Sr_3Li_2$ : A Reinvestigation of the Sr–Li Phase Diagram. *Inorg. Chem.* **54**, 733–739 (2015).

76. Farley, T. W. D., Hayes, W., Hull, S., Hutchings, M. T. & Vrtis, M. Investigation of thermally induced $Li^+$ ion disorder in $Li_2O$ using neutron diffraction. *J. Phys. Condens. Matter* **3**, 4761–4781 (1991).

77. Park, J. M. *et al.* Reversible crystalline-amorphous phase transformation in Si nanosheets with lithi-/delithiation. *Nanotechnology* **28**, 255401 (2017).

78. Etacheri, V., Marom, R., Elazari, R., Salitra, G. & Aurbach, D. Challenges in the development of advanced Li-ion batteries: a review. *Energy Environ. Sci.* **4**, 3243 (2011).

79. Aurbach, D. A Comparative Study of Synthetic Graphite and Li Electrodes in Electrolyte Solutions Based on Ethylene Carbonate-Dimethyl Carbonate Mixtures. *J. Electrochem. Soc.* **143**, 3809 (1996).

80. Thackeray, M. M. Spinel Electrodes for Lithium Batteries. *J. Am. Ceram. Soc.* **82**, 3347–3354 (2004).

81. Winter, M., Besenhard, J. O., Spahr, M. E. & Novák, P. Insertion Electrode Materials for Rechargeable Lithium Batteries. *Adv. Mater.* **10**, 725–763 (1998).

82. Pinson, M. B. & Bazant, M. Z. Theory of SEI Formation in Rechargeable Batteries: Capacity Fade, Accelerated Aging and Lifetime Prediction. *J. Electrochem. Soc.* **160**, A243–A250 (2012).

83. Nie, M., Abraham, D. P., Chen, Y., Bose, A. & Lucht, B. L. Silicon Solid Electrolyte Interphase (SEI) of Lithium Ion Battery Characterized by Microscopy and Spectroscopy. *J. Phys. Chem. C* **117**, 13403–13412 (2013).

84. Lehmann, V. Formation Mechanism and Properties of Electrochemically Etched Trenches in n-Type Silicon. *J. Electrochem. Soc.* **137**, 653 (1990).

85. McDowell, M. T., Lee, S. W., Nix, W. D. & Cui, Y. 25th Anniversary Article: Understanding the Lithiation of Silicon and Other Alloying Anodes for Lithium-Ion Batteries. *Adv. Mater.* **25**, 4966–4985 (2013).

86. Neubüser, G., Hansen, S., Duppel, V., Adelung, R. & Kienle, L. (Re-)crystallization mechanism of highly oriented Si-microwire arrays by TEM analysis. *J. Solid State Electrochem.* **21**, 3421–3427 (2017).

87. Langford, R. M. Focused ion beams techniques for nanomaterials characterization. *Microsc. Res. Tech.* **69**, 538–549 (2006).

88. Reid, N. & Beesley, J. E. *Sectioning and cryosectioning for electron microscopy*. (Elsevier ; Sole distributors for the U.S.A., Elsevier Science Pub. Co, 1991).

89. Hansen, S. On the Stabilization Mechanisms of Silicon Microwire Array Anodes for Li-Ion Batteries. (2017).

90. Archer, R. J. Optical Measurement of Film Growth on Silicon and Germanium Surfaces in Room Air. *J. Electrochem. Soc.* **104**, 619 (1957).

91. Lukeš, F. Oxidation of Si and GaAs in air at room temperature. *Surf. Sci.* **30**, 91–100 (1972).

92. Morita, M., Ohmi, T., Hasegawa, E., Kawakami, M. & Ohwada, M. Growth of native oxide on a silicon surface. *J. Appl. Phys.* **68**, 1272–1281 (1990).

93. Zhang, S. S. A review on electrolyte additives for lithium-ion batteries. *J. Power Sources* **162**, 1379–1394 (2006).

94. Schroder, K. W., Celio, H., Webb, L. J. & Stevenson, K. J. Examining Solid Electrolyte Interphase Formation on Crystalline Silicon Electrodes: Influence of Electrochemical Preparation and Ambient Exposure Conditions. *J. Phys. Chem. C* **116**, 19737–19747 (2012).

95. *Electrolytes for Lithium and Lithium-Ion Batteries*. **58**, (Springer New York, 2014).

96. Liu, X. H. *et al.* Anisotropic Swelling and Fracture of Silicon Nanowires during Lithiation. *Nano Lett.* **11**, 3312–3318 (2011).

97. Chan, M. K. Y., Wolverton, C. & Greeley, J. P. First Principles Simulations of the Electrochemical Lithiation and Delithiation of Faceted Crystalline Silicon. *J. Am. Chem. Soc.* **134**, 14362–14374 (2012).

98. Kasavajjula, U., Wang, C. & Appleby, A. J. Nano- and bulk-silicon-based insertion anodes for lithium-ion secondary cells. *J. Power Sources* **163**, 1003–1039 (2007).

99. Wang, C.-M. *et al.* In Situ TEM Investigation of Congruent Phase Transition and Structural Evolution of Nanostructured Silicon/Carbon Anode for Lithium Ion Batteries. *Nano Lett.* **12**, 1624–1632 (2012).

100. Wang, H., Ji, X., Chen, C., Xu, K. & Miao, L. Lithium diffusion in silicon and induced structure disorder: A molecular dynamics study. *AIP Adv.* **3**, 112102 (2013).

101. Lee, S. W., McDowell, M. T., Berla, L. A., Nix, W. D. & Cui, Y. Fracture of crystalline silicon nanopillars during electrochemical lithium insertion. *Proc. Natl. Acad. Sci.* **109**, 4080–4085 (2012).

102. Ryu, I., Choi, J. W., Cui, Y. & Nix, W. D. Size-dependent fracture of Si nanowire battery anodes. *J. Mech. Phys. Solids* **59**, 1717–1730 (2011).

103. Iaboni, D. S. M. & Obrovac, M. N. $Li_{15}Si_4$ Formation in Silicon Thin Film Negative Electrodes. *J. Electrochem. Soc.* **163**, A255–A261 (2016).

104. Gibbons, J. F. Ion implantation in semiconductors—Part II: Damage production and annealing. *Proc. IEEE* **60**, 1062–1096 (1972).

105. Baek, S.-H. *et al.* Influence of the crystallographic orientation of silicon nanowires in a carbon matrix on electrochemical performance as negative electrode materials for lithium-ion batteries. *J. Power Sources* **244**, 515–520 (2013).

106. Liu, N. *et al.* A Yolk-Shell Design for Stabilized and Scalable Li-Ion Battery Alloy Anodes. *Nano Lett.* **12**, 3315–3321 (2012).

107. Sandu, G. *et al.* Surface Coating Mediated Swelling and Fracture of Silicon Nanowires during Lithiation. *ACS Nano* **8**, 9427–9436 (2014).

108. Schmitz, R. W. *et al.* Investigations on novel electrolytes, solvents and SEI additives for use in lithium-ion batteries: Systematic electrochemical characterization and detailed analysis by spectroscopic methods. *Prog. Solid State Chem.* **42**, 65–84 (2014).

109. Barchasz, C., Lepretre, J.-C., Patoux, S. & Alloin, F. Revisiting TEGDME/DIOX Binary Electrolytes for Lithium/Sulfur Batteries: Importance of Solvation Ability and Additives. *J. Electrochem. Soc.* **160**, A430–A436 (2013).

110. Andersson, A. M. *et al.* Surface Characterization of Electrodes from High Power Lithium-Ion Batteries. *J. Electrochem. Soc.* **149**, A1358 (2002).

111. Verma, P., Maire, P. & Novák, P. A review of the features and analyses of the solid electrolyte interphase in Li-ion batteries. *Electrochimica Acta* **55**, 6332–6341 (2010).

112. Lee, H. H., Wan, C. C. & Wang, Y. Y. Thermal Stability of the Solid Electrolyte Interface on Carbon Electrodes of Lithium Batteries. *J. Electrochem. Soc.* **151**, A542 (2004).

113. Shim, J. *et al.* 2D boron nitride nanoflakes as a multifunctional additive in gel polymer electrolytes for safe, long cycle life and high rate lithium metal batteries. *Energy Environ. Sci.* **10**, 1911–1916 (2017).

114. Rodrigues, M.-T. F. *et al.* Hexagonal Boron Nitride-Based Electrolyte Composite for Li-Ion Battery Operation from Room Temperature to 150 °C. *Adv. Energy Mater.* **6**, 1600218 (2016).

115. Jung, H. Amorphous silicon anode for lithium-ion rechargeable batteries. *J. Power Sources* **115**, 346–351 (2003).

116. Uehara, M., Suzuki, J., Tamura, K., Sekine, K. & Takamura, T. Thick vacuum deposited silicon films suitable for the anode of Li-ion battery. *J. Power Sources* **146**, 441–444 (2005).

117. Cui, L.-F., Ruffo, R., Chan, C. K., Peng, H. & Cui, Y. Crystalline-Amorphous Core−Shell Silicon Nanowires for High Capacity and High Current Battery Electrodes. *Nano Lett.* **9**, 491–495 (2009).

118. Magasinski, A. *et al.* High-performance lithium-ion anodes using a hierarchical bottom-up approach. *Nat. Mater.* **9**, 353–358 (2010).

119. Lin, N. *et al.* A Si/Ge nanocomposite prepared by a one-step solid-state metathesis reaction and its enhanced electrochemical performance. *J. Mater. Chem. A* **3**, 11199–11202 (2015).

120. Wentorf, R. H. & Kasper, J. S. Two New Forms of Silicon. *Science* **139**, 338–339 (1963).

121. Li, H. The crystal structural evolution of nano-Si anode caused by lithium insertion and extraction at room temperature. *Solid State Ion.* **135**, 181–191 (2000).

122. Kaxiras, E. Effect of surface reconstruction on stability and reactivity of Si clusters. *Phys. Rev. Lett.* **64**, 551–554 (1990).

123. Röthlisberger, U., Andreoni, W. & Parrinello, M. Structure of nanoscale silicon clusters. *Phys. Rev. Lett.* **72**, 665–668 (1994).

124. Von Schnering, H.-G., Schwarz, M. & Nesper, R. The lithium sodium silicide Li3NaSi6 and the formation of allo-silicon. *J. Common Met.* **137**, 297–310 (1988).

125. Grüttner, A., Nesper, R. & von Schnering, H. G. Novel Metastable Germanium Modifications *allo* -Ge and 4H-Ge from Li $_{7}$ Ge $_{12}$. *Angew. Chem. Int. Ed. Engl.* **21**, 912–913 (1982).

126. Zaikina, J. V. *et al.* Thermochemistry, Morphology, and Optical Characterization of Germanium Allotropes. *Chem. Mater.* **26**, 3263–3271 (2014).

127. Sepulveda-Guzman, S. *et al. In situ* formation of bismuth nanoparticles through electron-beam irradiation in a transmission electron microscope. *Nanotechnology* **18**, 335604 (2007).

128. Pelaz, L., Marqués, L. A. & Barbolla, J. Ion-beam-induced amorphization and recrystallization in silicon. *J. Appl. Phys.* **96**, 5947–5976 (2004).

129. Dismukes, J. P., Ekstrom, L. & Paff, R. J. Lattice Parameter and Density in Germanium-Silicon Alloys $^{1}$. *J. Phys. Chem.* **68**, 3021–3027 (1964).

130. Hölken, I. *et al.* Sacrificial Template Synthesis and Properties of 3D Hollow-Silicon Nano- and Microstructures. *ACS Appl. Mater. Interfaces* **8**, 20491–20498 (2016).

131. Fuller, M. L. Twinning in Zinc Oxide. *J. Appl. Phys.* **15**, 164–170 (1944).

132. Mishra, Y. K. *et al.* Fabrication of Macroscopically Flexible and Highly Porous 3D Semiconductor Networks from Interpenetrating Nanostructures by a Simple Flame Transport Approach. *Part. Part. Syst. Charact.* **30**, 775–783 (2013).

133. Houben, L. *et al.* Structural properties of microcrystalline silicon in the transition from highly crystalline to amorphous growth. *Philos. Mag. A* **77**, 1447–1460 (1998).

134. Batson, P. E. Current trends for EELS studies in physics. *Microsc. Microanal. Microstruct.* **2**, 395–402 (1991).

135. Schamm, S. *et al.* Imaging Si nanoparticles embedded in SiO2 layers by (S)TEM-EELS. *Ultramicroscopy* **108**, 346–357 (2008).

136. Zacharias, M. *et al.* Thermal crystallization of amorphous Si/SiO2 superlattices. *Appl. Phys. Lett.* **74**, 2614–2616 (1999).

137. Nitta, N., Wu, F., Lee, J. T. & Yushin, G. Li-ion battery materials: present and future. *Mater. Today* **18**, 252–264 (2015).

138. Ohzuku, T. & Makimura, Y. Layered Lithium Insertion Material of LiCo $_{1/3}$ Ni $_{1/3}$ Mn $_{1/3}$ O $_{2}$ for Lithium-Ion Batteries. *Chem. Lett.* **30**, 642–643 (2001).

139. Liu, W. *et al.* Nickel-Rich Layered Lithium Transition-Metal Oxide for High-Energy Lithium-Ion Batteries. *Angew. Chem. Int. Ed.* **54**, 4440–4457 (2015).

140. Poizot, P., Laruelle, S., Grugeon, S., Dupont, L. & Tarascon, J. M. Nano-sized transition-metal oxides as negative-electrode materials for lithium-ion batteries. *Nature* **407**, 496–499 (2000).

141. Alcántara, R., Jaraba, M., Lavela, P. & Tirado, J. L. $NiCo_2O_4$ Spinel: First Report on a Transition Metal Oxide for the Negative Electrode of Sodium-Ion Batteries. *Chem. Mater.* **14**, 2847–2848 (2002).

142. Yuan, C., Wu, H. B., Xie, Y. & Lou, X. W. D. Mixed Transition-Metal Oxides: Design, Synthesis, and Energy-Related Applications. *Angew. Chem. Int. Ed.* **53**, 1488–1504 (2014).

143. Biagioni, C. & Pasero, M. The systematics of the spinel-type minerals: An overview. *Am. Mineral.* **99**, 1254–1264 (2014).

144. Permien, S. Investigation of the reaction mechanisms during Li uptake and release of spinel oxide nanoparticles M II-M III-FeO4 (MII = Mn, Mg, Co, Ni; M III = Mn, Fe) for application as anode materials in Lithium ion batteries. (2016).

145. Permien, S. *et al.* Transition metal cations on the move: simultaneous *operando* X-ray absorption spectroscopy and X-ray diffraction investigations during Li uptake and release of a $NiFe_2O_4$ /CNT composite. *Phys. Chem. Chem. Phys.* (2018). doi:10.1039/C8CP02919A

146. Permien, S. *et al.* Elucidation of the Conversion Reaction of $CoMnFeO_4$ Nanoparticles in Lithium Ion Battery Anode via Operando Studies. *ACS Appl. Mater. Interfaces* **8**, 15320–15332 (2016).

147. Chu, Y.-Q., Fu, Z.-W. & Qin, Q.-Z. Cobalt ferrite thin films as anode material for lithium ion batteries. *Electrochimica Acta* **49**, 4915–4921 (2004).

148. Lavela, P. & Tirado, J. L. CoFe2O4 and NiFe2O4 synthesized by sol–gel procedures for their use as anode materials for Li ion batteries. *J. Power Sources* **172**, 379–387 (2007).

149. Cabana, J., Monconduit, L., Larcher, D. & Palacín, M. R. Beyond Intercalation-Based Li-Ion Batteries: The State of the Art and Challenges of Electrode Materials Reacting Through Conversion Reactions. *Adv. Mater.* **22**, E170–E192 (2010).

150. Zeng, G. *et al.* A General Method of Fabricating Flexible Spinel-Type Oxide/Reduced Graphene Oxide Nanocomposite Aerogels as Advanced Anodes for Lithium-Ion Batteries. *ACS Nano* **9**, 4227–4235 (2015).

151. Permien, S. *et al.* The Role of Reduced Graphite Oxide in Transition Metal Oxide Nanocomposites Used as Li Anode Material: An Operando Study on $CoFe_2O_4$ /rGO. *Chem. - Eur. J.* **22**, 16929–16938 (2016).

152. Rieck, G. D. & Thijssen, J. J. M. The cation distribution in $CoFe_2O_4$. *Acta Crystallogr. B* **24**, 982–983 (1968).

153. Goyal, A., Bansal, S., Kumar, V., Singh, J. & Singhal, S. Mn substituted cobalt ferrites (CoMnxFe2−xO4 (x=0.0, 0.2, 0.4, 0.6, 0.8, 1.0)): As magnetically separable

heterogeneous nanocatalyst for the reduction of nitrophenols. *Appl. Surf. Sci.* **324**, 877–889 (2015).

154. Caltun, O. *et al.* The influence of Mn doping level on magnetostriction coefficient of cobalt ferrite. *J. Magn. Magn. Mater.* **316**, e618–e620 (2007).

155. Lavela, P., Kyerematenga, N. A. & Tirado, J. L. NiMn2−xFexO4 prepared by a reverse micelles method as conversion anode materials for Li-ion batteries. *Mater. Chem. Phys.* **124**, 102–108 (2010).

156. Cherian, C. T. *et al.* Morphologically Robust NiFe $_2$ O $_4$ Nanofibers as High Capacity Li-Ion Battery Anode Material. *ACS Appl. Mater. Interfaces* **5**, 9957–9963 (2013).

157. Hastings, J. M. & Corliss, L. M. Neutron Diffraction Studies of Zinc Ferrite and Nickel Ferrite. *Rev. Mod. Phys.* **25**, 114–119 (1953).

158. Shirane, G., Pickart, S. J., Nathans, R. & Ishikawa, Y. Neutron-diffraction study of antiferromagnetic FeTi03 and its solid solutions with α-Fe2O3. *J. Phys. Chem. Solids* **10**, 35–43 (1959).

159. Barrett, C. A. & Evans, E. B. Solid Solubility and Lattice Parameter of NiO-MnO. *J. Am. Ceram. Soc.* **47**, 533–533 (1964).

160. Trucano, P. & Chen, R. Structure of graphite by neutron diffraction. *Nature* **258**, 136–137 (1975).

161. Bruce, P. G., Hardwick, L. J. & Abraham, K. M. Lithium-air and lithium-sulfur batteries. *MRS Bull.* **36**, 506–512 (2011).

162. Schütt, F. *et al.* Hierarchical self-entangled carbon nanotube tube networks. *Nat. Commun.* **8**, (2017).

163. Wild, M. *et al.* Lithium sulfur batteries, a mechanistic review. *Energy Environ. Sci.* **8**, 3477–3494 (2015).

164. Mikhaylik, Y. V. & Akridge, J. R. Polysulfide Shuttle Study in the Li/S Battery System. *J. Electrochem. Soc.* **151**, A1969 (2004).

165. Ji, X., Lee, K. T. & Nazar, L. F. A highly ordered nanostructured carbon–sulphur cathode for lithium–sulphur batteries. *Nat. Mater.* **8**, 500–506 (2009).

166. Levin, B. D. A. *et al.* Characterization of Sulfur and Nanostructured Sulfur Battery Cathodes in Electron Microscopy Without Sublimation Artifacts. *Microsc. Microanal.* **23**, 155–162 (2017).

167. Johnson, A. S. *et al.* Measurement of sulfur L2,3 and carbon K edge XANES in a polythiophene film using a high harmonic supercontinuum. *Struct. Dyn.* **3**, 062603 (2016).

168. Senninger, D. Analysis of electron diffraction patterns from carbon nanotubes with image processing to determine structural parameters. (2011).

169. Avdeev, V. V., Savchenkova, A. P., Monyakina, L. A., Nikol'skaya, I. V. & Khvostov, A. V. Intercalation reactions and carbide formation in graphite-lithium system. *J. Phys. Chem. Solids* **57**, 947–949 (1996).

170. Stephenson, T., Li, Z., Olsen, B. & Mitlin, D. Lithium ion battery applications of molybdenum disulfide ($MoS_2$) nanocomposites. *Energy Env. Sci* **7**, 209–231 (2014).

171. Xiao, J. *et al.* Electrochemically Induced High Capacity Displacement Reaction of PEO/MoS2/Graphene Nanocomposites with Lithium. *Adv. Funct. Mater.* **21**, 2840–2846 (2011).

172. Liang, X. *et al.* A highly efficient polysulfide mediator for lithium–sulfur batteries. *Nat. Commun.* **6**, (2015).

173. Goetzberger, A., Hebling, C. & Schock, H.-W. Photovoltaic materials, history, status and outlook. *Mater. Sci. Eng. R Rep.* **40**, 1–46 (2003).

174. Klenk, R. *et al.* Solar cells based on CuInS2—an overview. *Thin Solid Films* **480–481**, 509–514 (2005).

175. Pan, Z. *et al.* High-Efficiency "Green" Quantum Dot Solar Cells. *J. Am. Chem. Soc.* **136**, 9203–9210 (2014).

176. *Solar cells: materials, manufacture and operation*. (Elsevier Advanced Technology, 2005).

177. Philipps, S. *PHOTOVOLTAICS REPORT*. (Fraunhofer ISE, 2018).

178. Mills, A. & Le Hunte, S. An overview of semiconductor photocatalysis. *J. Photochem. Photobiol. Chem.* **108**, 1–35 (1997).

179. *Photocatalysis*. (Springer, 2011).

180. Kazmerski, L. L. & Shieh, C. C. Photoconductivity effects in CuInS2, CuInSe2 and CuInTe2 thin films. *Thin Solid Films* **41**, 35–41 (1977).

181. Luo, J. *et al.* Solution Transformation of $Cu_2O$ into $CuInS_2$ for Solar Water Splitting. *Nano Lett.* **15**, 1395–1402 (2015).

182. Binsma, J. J. M., Giling, L. J. & Bloem, J. Phase relations in the system Cu2S-In2S3. *J. Cryst. Growth* **50**, 429–436 (1980).

183. Khemiri, N., Abdelkader, D., Khalfallah, B. & Kanzari, M. Synthesis and Characterization of CuIn<sub>2n+1</sub> S<sub>3n+2</sub> (with n = 0, 1, 2, 3 and 5) Powders. *Open J. Synth. Theory Appl.* **02**, 33–37 (2013).

184. Tell, B., Shay, J. L. & Kasper, H. M. Electrical Properties, Optical Properties, and Band Structure of CuGa S 2 and CuIn S 2. *Phys. Rev. B* **4**, 2463–2471 (1971).

185. Liu, Y., Liu, M. & Swihart, M. T. Shape Evolution of Biconcave Djurleite Cu $_{1.94}$ S Nanoplatelets Produced from CuInS $_2$ Nanoplatelets by Cation Exchange. *J. Am. Chem. Soc.* **139**, 18598–18606 (2017).

186. Vukusic, P. & Sambles, J. R. Erratum: Photonic structures in biology. *Nature* **424**, 852–855 (2003).

187. Qi, Y. *et al.* Synthesis and Characterization of Nanostructured Wurtzite CuInS $_2$ : A New Cation Disordered Polymorph of CuInS $_2$. *J. Phys. Chem. C* **113**, 3939–3944 (2009).

188. Khemiri, N. & Kanzari, M. Comparative study of structural and morphological properties of CuIn3S5 and CuIn7S11 materials. *Nucl. Instrum. Methods Phys. Res. Sect. B Beam Interact. Mater. At.* **268**, 268–272 (2010).

189. Scheer, R. & Lewerenz, H. -J. Formation of secondary phases in evaporated CuInS $_2$ thin films: A surface analytical study. *J. Vac. Sci. Technol. Vac. Surf. Films* **13**, 1924–1929 (1995).

190. Drummy, L. F. *et al.* High-Resolution Electron Microscopy of Montmorillonite and Montmorillonite/Epoxy Nanocomposites. *J. Phys. Chem. B* **109**, 17868–17878 (2005).

191. Welberry, T. R. & Goossens, D. J. Diffuse scattering and partial disorder in complex structures. *IUCrJ* **1**, 550–562 (2014).

192. Zhang, J., Yu, J., Jaroniec, M. & Gong, J. R. Noble Metal-Free Reduced Graphene Oxide-Zn $_x$ Cd $_{1-x}$ S Nanocomposite with Enhanced Solar Photocatalytic H $_2$ -Production Performance. *Nano Lett.* **12**, 4584–4589 (2012).

193. Tsuji, I., Kato, H., Kobayashi, H. & Kudo, A. Photocatalytic H $_2$ Evolution Reaction from Aqueous Solutions over Band Structure-Controlled (AgIn) $_x$ Zn $_{2(1-x)}$ S $_2$ Solid Solution Photocatalysts with Visible-Light Response and Their Surface Nanostructures. *J. Am. Chem. Soc.* **126**, 13406–13413 (2004).

## Danksagung

Alle Ergebnisse und Erkenntnisse dieser Dissertation wurden während der Arbeit am Lehrstuhl *Synthesis and Real Structure* erarbeitet, und für die Aufnahme in diese Gruppe und die Möglichkeit, dieses tolle Arbeitsumfeld zu nutzen, möchte ich mich herzlich bei Prof. Dr. Lorenz Kienle bedanken.
Für seine fachliche und persönliche Betreuung und Unterstützung in allen Lagen, geht ein besonderer Dank an Dr. Ulrich Schürmann, ebenso an Katrin Brandenburg für die Organisation und Verwaltung des Forschungsalltags.
Unverzichtbar für meine Forschung war die Unterstützung durch Christin Szillus und Viola Duppel und deren – mir stets unerreichbaren – Fertigkeiten in den Bereichen Synthese und Spezialuntersuchung. Ein besonderer Dank geht hier an Sandra Hansen, ohne deren revolutionäre Forschung an der Kieler Batterie meine Arbeit nicht möglich gewesen wäre.
Unverzichtbar während der letzten Jahre war das angenehme Arbeitsumfeld mit maßgeblicher Beteiligung der geliebten Kolleginnen und Kollegen Torben Dankwort, Nico Gaida, Hendrik Groß, Marius Kamp, Julian Strobel, Niklas Wolff, Ole Gronenberg, Martin Hicke, Khurram Saleem, Ullrich Schürmann, Christin Szillus, Ahmad Takriti, Marie Ullrich und Lennart Voß.
Ebenso möchte ich mich herzlich bei ehemaligen Mitgliedern der Gruppe bedanken: Mao Deng, Burak Erkartal, Dietrich Häussler, Viktor Hrkac, Venkata Sai Kiran Chakravadhanula, Igor Barg, Grit Köppel, Cai Müller, Lena Nolte und Moritz Schultes.
Aus der benachbahrten Arbeitgruppe von Prof. Dr. Adelung möchte ich mich bei Iris Hölken, Mathias Hoppe, E. A. Victor P. Kaidas, Fabian Schütt und Daria Smazna bedanken.
Im Verlauf meiner Promotion entstanden viele Kooperationen mit tollen Menschen, denen ich an dieser Stelle danken möchte: Henning Lühmann, Stefan Permien, Enrique Quiroga-González, Lavinia Scherf und Miachel Zeilinger.
Darüberhinaus danke ich allen Personen, die mich in den letzten Jahren an der Technischen Fakultät begleitet haben, für eine tolle Zeit, die mit dem ersten Studientag begann und mir immer gut in Erinnnerung bleiben wird.
Für ihre Unterstützung und Inspiration, die mich bis zur Promotion führte, danke ich allen voran meiner Familie und meinen Freunden, ohne die ich es nicht bis hierher geschafft hätte.
Zuletzt danke ich Judith, dafür dass du mich so liebst wie ich dich und mich stets unterstützt bei all unseren Vorhaben.